Influence of acquisition time and smoothing parameters on Ga–68 wholebody PET/CT image quality

by

Boitshoko Phenyo Diale

Thesis presented in partial fulfilment of the requirements for the degree of Master of Science in Nuclear Medicine in the Faculty of Medicine and Health Science at Stellenbosch University

Supervisor: Mr. Tumelo Moalosi

Co–supervisors: Dr. Michael Mix

Prof. Annare Ellmann

December 2020

Declaration

By submitting this thesis electronically, I declare that the entirety of the work contained therein is my own, original work, that I am the sole author thereof (save to the extent explicitly otherwise stated), that reproduction and publication thereof by Stellenbosch University will not infringe any third party rights and that I have not previously in its entirety or in part submitted it for obtaining any qualification.

Abstract

PET/CT image optimization has been extensively investigated for ^{18}F–FDG PET imaging. Although ^{68}Ga–tracers are already widely used in PET, optimized imaging and reconstruction are still missing. The aim of this research was to optimize image quality for ^{68}Ga scans under the constraint that the administered dose to a patient and acquisition time are limited.

Materials and Methods

A Gemini TF Big Bore PET/CT system manufactured by Philips was used to acquire the images. The experimental data was formulated by retrospectively collecting data from patient scans, who had undergone wholebody (WB) PET/CT using ^{68}Ga–DOTANOC for oncological imaging. The patient data sets were analyzed for this study to plan phantom measurements which simulated a typical activity distribution like in the patient scans. The NEMA (IEC) body phantom filled with low contrast and high contrast activity ratios was scanned on the Gemini TF Big Bore PET/CT scanner using the patient acquisition protocol.

The data was reconstructed using a default WB reconstruction protocol with different smoothing parameters and varying scan acquisition times for low and high contrast data. Additionally a HN protocol with smaller voxel sizes was also used on high contrast data. The set images were analyzed using R Studio. Image quality parameters such as coefficient of variation (COV%), contrast to noise ratio (CNR), signal to noise ratio (SNR), recovery coefficient (RC%) and uniformity in terms of standardized uptake value (SUV) were acquired.

Results

For low contrast COV%, CNR, SNR values varied as follows: 0.89 – 0.99%, 0.96 – 1.08, 0.99 – 1.05, respectively. Values for high contrast varied as follows: 1.03 – 1.16%, 0.84 – 0.91, 0.80 – 0.97. When comparing COV%, CNR and SNR, low contrast images appeared to be superior to high contrast images. The RC% was found to be consistent in both low contrast and high contrast irrespective of the smoothing parameter.

Conclusion

The results obtained from the phantom study demonstrated the Philips Gemini TF Big Bore PET scanner's stability of good uniformity when assessing maximum activity concentration among the different acquisitions, and ability of the scanner to detect or recover radioactivity in low and high contrast images for all reconstruction parameters. From the phantom study results, incorporating the smoothing reconstruction parameter "smooth" on low contrast images, allowed the reduction of acquisition time to 180 seconds while maintaining acceptable image quality.

Opsomming

Optimale beeldkwaliteit van PET/RT beelding is vir ^{18}F–FDG PET beelding reeds in diepte ondersoek. Alhoewel ^{68}Ga–spoorders reeds algemeen in PET gebruik word, is daar steeds 'n leemte in die daarstelling van optimale beelding en rekonstruksie parameters. Die doel van hierdie navorsing was om beeldkwaltiteit van ^{68}Ga skandering te optimaliseer met die inagneming van beperkings in die toegediende dosis en beeldingstyd

Materiaal en Metodes

'n Philips Gemini TF *Big Bore* PET/RT kamera is vir beelding gebruik. Die eksperimentele data is beplan deur retrospektief data van onkologiese heeliggaam (HL) ^{68}Ga–DOTANOC PET/RT studies te versamel. Hierdie data is geanaliseer om fantoommetings te beplan wat tipiese verspreiding van aktiwiteit in pasiëntstudies sou simuleer. 'n NEMA (IEC) liggaamsfantoom is met lae en hoë kontras aktiwiteitverhoudings gevul en vervolgens, volgens die bestaande pasiëntbeeldingsprotokol, met die Gemini TF *Big Bore* PET/RT kamera skandeer.

Die data is met 'n verstek HL rekonstruksieprotokol met verskillende vergladdingsparameters en variërende beeldingstye vir lae en hoë kontrasdata verwerk. Bykomend is 'n kop–en nek–protokol met kleiner vokselgrootte op hoë kontrasdata ook gebruik. Die beelde is met R studio geanaliseer. Beeldkwaliteitparameters soos variasiekkoëffisiënt (COV%), kontras tot geraas verhouding (CNR), sein tot geraas verhouding (SNR), herstelkoëffisiënt (RC%) en uniformiteit in terme van gestandardiseerde opname waarde (SUV), is verkry.

Resultate

Vir lae kontras het COV%, CNR, en SNR waardes respektiewelik soos volg gevarieer: 0.89–0.99%, 0.96–1.08, en 0.99–1.05. Waardes vir hoë kontras het soos volg gevarieer: 1.03 – 1.16%, 0.84–0.91, en 0.80–0.97. As COV%, CNR en SNR vergelyk is, was lae kontras beelde beter as hoë kontras beelde. Die RC% was konstant in beide lae kontras en hoë kontras, ongeag die vergladdingsparameter.

Gevolgtrekking

Die resultate van die fantoomstudie het die Philips Gemini TF *Big Bore* PET skandeerder se stabiele uniformiteit, in die evaluering van maksimum aktiwiteit konsentrasie tydens verskillende beeldverkrygings, bevestig. Dit het getoon dat die skandeerder in staat is om radioaktiwiteit in lae en hoë kontrasbeelde, vir alle rekonstruksieparameters, waar te neem. Volgens die resultate van die fantoomstudies kan die beeldingstyd tot 180 sekondes verkort word, as die verwerkingsparameter ”glad” (smooth) in die lae kontras beelding gebruik is.

Acknowledgements

The start and completion of this work seemed impossible but with the support and encouragement from many, the final product is here.

I would like to thank my mentors, co–investigators and supervisors:

Dr. Michael Mix (University Medical Center Freiburg, Germany), who is the initiator of this project, for the experience he imparted to me and the knowledge he shared, as well as the time he gave.

Mr. Tumelo Moalosi (Medical Physicist, Tygerberg Hospital) for the long hours spent while brainstorming this research idea as well as time he gave in imparting his knowledge of operating the PET/CT scanner. His scientific expertise and knowledge proved invaluable and led to the realisation of this work. Thank you for believing in me, your encouraging words and prayers kept me focused to completion of this project. You are a great teacher.

The head of Division of Nuclear Medicine and my co–supervisor, Prof. A Ellmann, to whom I will forever be indebted for proof reading my thesis and sharing her research experiences with me in order to realise the completion of this project and for my development.

Special thanks to:
My supervisor at Radiation Control Ms. Emma Snyman for encouraging me to pursue this M.Sc. degree and immense support. You enthusiastically followed my progress and your encouraging words kept me focused to completion of this project.

Mr. Andrew Esau for exposing me to LaTex and R programming language and sharing your knowledge.

The staff at Radiation Control for words of encouragement and support.

Dedications

This work is dedicated to the almighty God with whom all things are possible (1 Cor 2:9), my ever supporting and loving wife (Regomoditswe) and daughter (Rorisang). I thank you for being there for me during my absence and sleepless nights.

I also would like to thank my supporting parents (Nchimane and Mmaesasa Diale) for this name Boitshoko ke Phenyo (Perseverance lead to victory – Rom 5:3–4, Hebr10:35–36) and instilling the importance of education; my brothers Letlhogonolo and Keamogetswe and my sister Lorato for encouraging me to focus on what I want to achieve at the end. I thank you all for your encouragement and prayers. Ke fitlhisitswe nakong e ke Rara wa lorato.

Contents

List of Figures

List of Tables

Abbreviations

1D	one dimensional
2D	two dimensional
3D	three dimensional
ART	algebraic reconstruction technique
BGO	bismuth germanate
CT	computed tomography
CNR	contrast to noise ratio
COV	coefficient of variation
EM	expectation maximization
FWHM	full width at half maximum
HN	head and neck
IEC	International Electrotechnical Commission
^{68}Ga	Gallium–68
^{68}Ge	Germanium–68
LOR	line of response
MLEM	maximum likelihood expectation maximization
NEMA	National Electrical Manufactures Association
OSEM	ordered subset expectation maximization
PET	positron emission tomography
PMT	photomultiplier tube
RAMLA	row action maximum likelihood algorithm
ROI	region of interest
SNR	signal to noise ratio
SPECT	single photon emission computed tomography
SUV	standardized uptake value

TOF	time of flight
WB	whole body
WCAPC	Western Cape Academic PET/CT Centre

Chapter 1

Introduction

1.1 Background of Nuclear Medicine Imaging

Nuclear Medicine utilizes unsealed radionuclides for diagnostic and therapeutic purposes. Distinct amounts of compounds labelled with radionuclides are applied either intravenously, or are swallowed or inhaled to provide diagnostic information or treatment of a wide range of diseases (Cherry, Sorenson and Phelps, 2012). Commonly used radionuclides for diagnostic purposes include ^{99m}Tc, ^{123}I and ^{111}In, that give off energy by emitting a gamma–ray to be detected by a single or dual scintillation detector gamma camera, and proton enriched radionuclides such as ^{15}O, ^{13}N and ^{18}F, which give off two photons of 511 keV at almost 180° following interaction of an emitted positron and electron to be detected simultaneously by two opposing detectors (Cherry, Sorenson and Phelps, 2012).

Nuclear Medicine images represent the spatial and temporal distribution of so–called tracers, representing physiological parameters like glucose metabolism, and receptor concentration and thus provide information about the function of organs in the body.

Nuclear Medicine includes three dimensional (3D) techniques such as positron emission tomography (PET) and single–photon emission computed tomography (SPECT), where filtered back projection or iterative algorithms are used to reconstruct images from emission projections (Cherry, Sorenson and Phelps, 2012).

In general, tomography is a principle of collecting data about an object from multiple views and using these projection data to reconstruct an image of an object.

In computed tomography (CT) imaging, a narrow X–ray beam is transmitted through an object in sync with a radiation detector on the opposite side of the object (Hendee and Ritenour, 2002). CT is a principle whereby the internal structure (in terms of density) of an object is reconstructed from multiple projections of the object. Contrary to nuclear medicine emission imaging, in CT multiple attenuated transmission views of the object are built in the detector, and a computer uses the same algorithm to reconstruct an image of the patient (Hendee and Ritenour, 2002). X–ray computed tomography has a very high spatial resolution and it illustrates the body's architectural structure (Fogelman, Gnanasegaran and van der Wall, 2012).

SPECT is a diagnostic imaging technique in which the gamma camera acquires multiple planar views of the radioactivity generated from a gamma–emitting radionuclide, and the radioactivity is detected at numerous positions about the distribution. The gamma camera acquires these multiple planar two dimensional (2D) projection views at 360° of which the data create an image (Cherry, Sorenson and Phelps, 2012).

Contrary to PET, this imaging technique relies on physical collimation to obtain directional information for incident photons. The collimator allows access of incident photons only in the direction parallel to the holes, and photons deflected away from the original direction are absorbed by the material of the collimator (Cherry, Sorenson and Phelps, 2012).

PET has higher sensitivity and better spatial resolution than SPECT due to the detection without an additional collimator, and the use of a complete ring of detectors and reduced attenuation of 511 keV photons (Smith and Webb, 2011).

1.2 PET Tracers

PET radionuclides are bound to molecules that are involved in the normal or pathological metabolism in the human body. The distribution and uptake of these molecules can be detected. This allows for evaluation, and quantification of metabolic processes (Garcea, Ong and Maddern, 2009).

Positron emitters are produced in a cyclotron, radionuclide generator or nuclear reactor. Radionuclide generators can be used for longer, thereby preventing a need for a cyclotron on site (Banerjee and Pomper, 2013).

^{68}Ga is a radioisotope characterized by a short half–life of 68 minutes and high energy positron decay. It is a daughter nuclide created from the decay of germanium–68 (^{68}Ge) (Martiniova et al., 2016). ^{68}Ge has a half–life of 271 days and decays by electron capture to ^{68}Ga (Saha, 2010). The ^{68}Ga radionuclide is eluted from the Germanium-68/Gallium-68 (^{68}Ge/^{68}Ga) generator using hydrochloric acid (HCl) and it is ready for use in preparation of radiotracers (Shanchez-Crespo, 2013).

^{68}Ga decays with 89% yield through positron emission (maximum energy of 2.92 MeV and a mean energy of 0.89 MeV) (Banerjee and Pomper, 2013). A ^{68}Ge/^{68}Ga generator can be used for 6–9 months providing cost–effectiveness and convenience (Banerjee and Pomper, 2013). The properties of ^{68}Ga have enhanced interest in PET imaging research due to its long–lived parent isotope that allows for it to be produced and obtained from a generator, eliminating the need for a cyclotron, making it most cost–effective (Martiniova et al., 2016).

1.3 Data Acquisition

PET is based on the use of unstable isotopes that release their energy by beta decay emitting a positron. The emitted positron travels a short distance, annihilates with an electron and the masses of the two particles are converted into two photons of 511 keV photons. The two photons are then emitted in coincidence and opposite directions forming a line of response (LOR) as shown in figure 1.1.

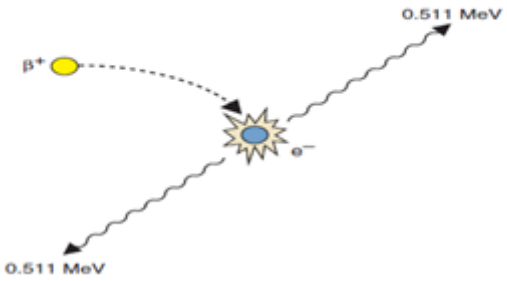

Figure 1.1: Representation of the annihilation reaction between a positron and an electron (Cherry, Sorenson and Phelps, 2012)

The LORs are arranged into parallel projections as defined by coincidence channels, and are used to reconstruct the 3D distribution of the positron emitter tracer within the patient (Zaidi, 2006). The detected events of a LOR are sorted into true coincidences and are detected simultaneously by the detectors.

A very common type of detector design is a multi–crystal two dimensional bismuth germanate (BGO) block detector, presented by Casey and Nutt (1986). Most modern detector systems still use the full ring arrangement of block detectors. The block detector design uses a positioning technique to achieve good spatial resolution and reduce dead time. When photons strike the crystals, they are absorbed and visible light is being emitted.

The block detector is coupled to a light guide and photocathode. The light guide distributes the light from the crystals into the photocathode (Casey and Nutt, 1986). It also enhances identification of the crystal by distributing the light to the photocathode in a controllable manner. This light is then detected and converted to photoelectrons by a photocathode.

The photoelectrons in turn are greatly amplified by a cascade of photocathodes in a photomultiplier tube (PMT). The electronic signal is generated by the PMT, then preamplified to get a homogenous signal output. This signal is amplified before being passed onto the computer for further analysis (Mittra and Quon, 2009).

The ideal principal characteristics of PET scintillator crystal–based detectors include: (a) high density to interact with the high energy 511 keV photons, as this results in effective detection of gamma–rays, (b) high light output per 511 keV photon, this allows to couple small crystals elements to a single photodetector, (c) short scintillation decay time to improve coincident detection (timing and count rate capability), (d) good energy resolution, (e) optimal length of the scintillation crystal, which provides a greater chance of interaction, and increased sensitivity, (f) the transmission of the scintillation light pulses into the photodetector, as it is best

when the refractive index of the scintillator material is similar to that of the entrance window and coupling material near 1.5 (Melcher, 2000; Mittra and Quon, 2009).

Acquired photons being detected are classified as true, scattered and random coincidence events as shown in figure 1.2.

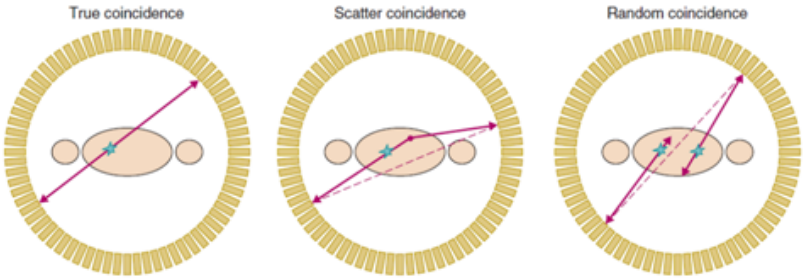

Figure 1.2: True coincidence event (left), scatter coincidence event (center) and random coincidence event (right) (Cherry, Sorenson and Phelps, 2012)

True coincidence: A true coincidence event occurs when two photons from a single annihilation event are registered by detectors in coincidence (Zaidi, 2006). In a true coincidence, neither photon encounters any form of interaction before detection, and no additional event is detected within the defined coincidence time window (Zaidi, 2006). True coincidence defines the LOR that includes the actual point of annihilation and contributes to accurately reflect the actual underlying radionuclide activity distribution (Karakatsanis, Fokou and Tsoumpass, 2015). The true coincidence events are desired, as they contribute to good PET image quality.

Scatter coincidence: Scatter events occur when one of the two gamma photons are subjected to Compton scattering when they interact with the patient's body or a neighbouring detector crystal before they are detected. The emitted photons lose kinetic energy as they interact with the surrounding material, change direction and are diverted from true coincidence at the detection point (Karakatsanis, Fokou and Tsoumpass, 2015).

Scattering results mainly in a loss of true counts, leading to increased noise and incorrect quantification of radioactivity distributions (Turkington, 2001). Scattered photons may be detected as accidental true coincidences if they are within the energy window accounted for by the PET system (Karakatsanis, Fokou and Tsoumpass, 2015).

Random coincidence: Random coincidences occur when two photons produced by different annihilations closer to each other in time are detected in opposing detectors (Karakatsanis, Fokou and Tsoumpass, 2015). The PET detection system registers the two photons and falsely assigns them to a LOR. The random coincidence rate increases with the amount of activity in the patient or object, significantly contributing to background noise in the image (Karakatsanis, Fokou and Tsoumpass, 2015).

Scatter and random coincidences comprise no spatial information about the tracer distribution and therefore they decrease image quality by reducing contrast (Karakatsanis, Fokou and Tsoumpass, 2015).

Attenuation is caused by scattered photons which lose more energy and are not detected causing PET image quality degradation, which can be corrected using a transmission attenuation scan to restore accurate representation of activity concentrations and to avoid artifacts (Cherry, Sorenson and Phelps, 2012). The transmission scan provides a detailed anatomic map (Mittra and Quon, 2009).

Workman and Coleman (2006), showed two methods by which attenuation correction can be performed. An older way is using photons from an external

transmission radionuclide line source (e.g. ^{68}Ge/^{68}Ga rods). The current way is the use of the CT detector which is situated on the PET gantry coaxially. The CT scan serves as a transmission map used for attenuation correction of the PET image and also provides a detailed anatomic image that is used for precise disease localization (Cherry, Sorenson and Phelps, 2012). When a CT is combined with a PET in the described manner, it is widely called a hybrid imaging system. Both data sets, PET and CT are acquired in the same imaging session sequentially so the patient does not need a second investigation. This translates into better patient tolerance, improved throughput and also reduces motion–induced artifacts (Workman and Coleman, 2006).

1.3.1 Time of flight

The accuracy in determining the time difference between arrival of coincidence photons at two detectors is a key parameter for the time of flight (ToF) PET scanner (Conti, 2011). In a conventional PET system, positron annihilation is assumed to be localized somewhere along the LOR between the two detectors without information regarding the exact interaction point (Ullah et al., 2016), as in figure 1.2.

For reconstruction, the annihilation events along this LOR are considered to be evenly distributed along this line, adding noise to the image (Ullah et al., 2016). Using ToF PET, the detected time difference between the annihilation pair is used, and the PET camera could restrict the position of the gamma positron annihilation to a small region along the LOR, improving the signal to noise ratio (SNR) of the final image (Ullah et al., 2016), as in figure 1.3. PET images reconstructed from projection data with ToF information have higher SNR and superior resolution (Karakatsanis, Fokou and Tsoumpass, 2015).

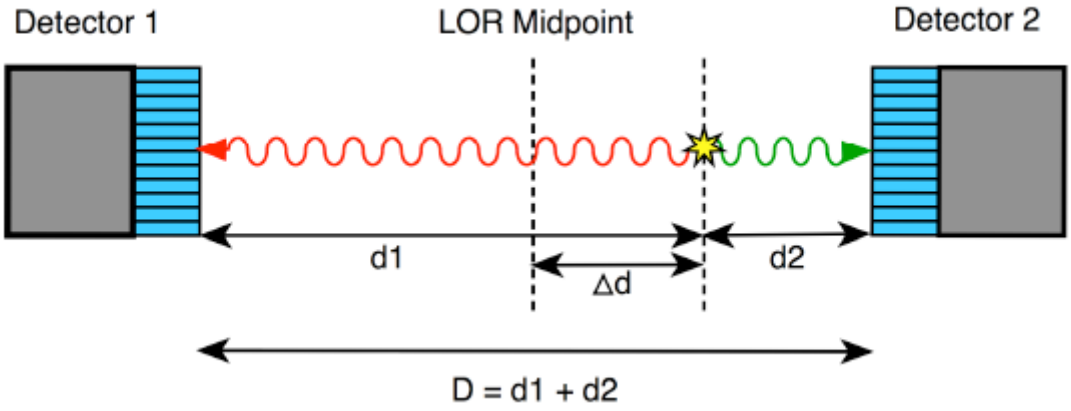

Figure 1.3: ToF PET system (McKeown, 2019)

The main motivation for ToF PET is to improve image quality or to reduce the image acquisition time (Vandenberghe et al., 2016). Better PET images mean better lesion detection or reducing either scan times or radiopharmaceutical doses with equal image quality (Lee, 2010). The key characteristics for ToF PET is to improve image quality due to a higher SNR and higher contrast recovery (Conti, 2011).

1.4 Image Reconstruction

The raw data once acquired are reconstructed to form a diagnostic image using 1) filtered back projection, or 2) iterative reconstruction (Mittra and Quon, 2009).

Filtered back–projection

Filtered back–projection is used for 2–D projections. It involves filtering and a back projection reconstruction method. In PET, the acquired data are collected along a LOR through a 2–D object f(x,y) as a line integral, as illustrated in figure 1.4.

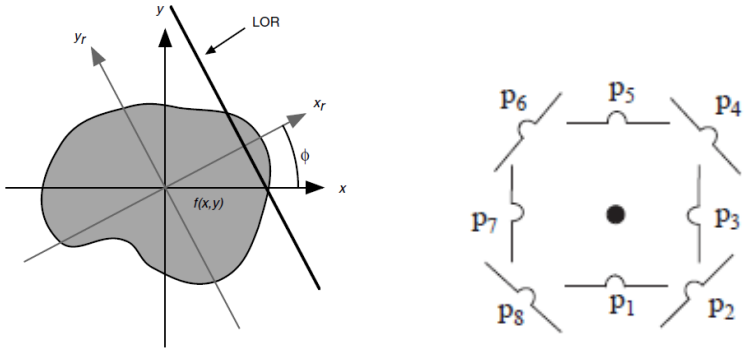

Figure 1.4: Two–dimensional LOR, image slice f(x,y) estimated from a set of projections to obtain a 2D sinogram (Wernick and Aarsvold, 2004)

The LOR's are projected on detectors, and a set of measurements are integrated along a line assuming the positron–electron annihilation occurred along straight lines through the object. In general, the detector is at an angle of θ degrees to the x–axis measurement, with θ having values between 0 and 360°. The intention is then to represent this 2–D object into polar co–ordinates of Fourier domain, a 2–D Fourier transform is then applied to the 2–D object (Smith and Webb, 2011). The Fourier slice theorem states that, a one–dimensional (1–D) Fourier transformation of the detector function at an angle θ is the same as a line through a two dimensional to the Fourier transform representation of the entire object (Al Hussani and Ali Al Hayani, 2014).

The raw data acquired by the detectors are taken from multiple forward projection angles summed up creating multiple slices or sinograms.

Using image reconstruction with back projection only, each projection is smeared back into the object region along the direction it was measured (Wernick and Aarsvold, 2004). After back projection, the image is blurred having a star artefact (Powsner, Palmer and Powsner, 2013), as in figure 1.5.

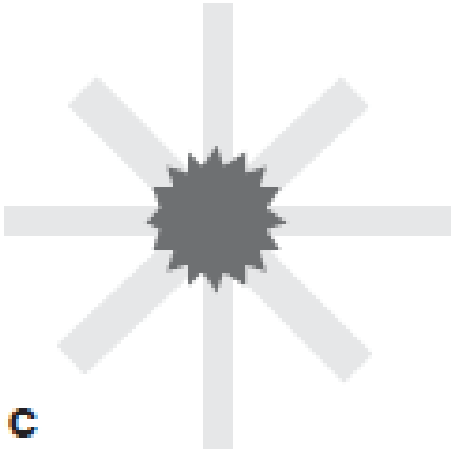

Figure 1.5: The process of back–projection involving summation (Smith and Webb, 2011)

Filtering is a mathematical technique applied during reconstruction to reduce noise and improve the appearance of the image (Powsner, Palmer and Powsner, 2013). Filtering is performed in the back projection also to eliminate the star artefact.

Iterative reconstruction

Iterative reconstruction assumes an initial image that is uniformly distributed as in figure 1.6. It then forward projects the estimated image into raw data space creating a sinogram (Smith and Webb, 2011). The sinogram is then compared with the actual initial raw data acquired to compute a correction term.

The correction term is back projected onto the image space (volumetric object) and multiplied with the previously forward projected image as the next image estimate. The better the prior images match the final images, the faster the process converges towards a stable solution. The iterative process is complete when either a fixed number of iterations are reached, or the update for the current image is considered small enough (Beister, Kolditz and Kalender, 2012).

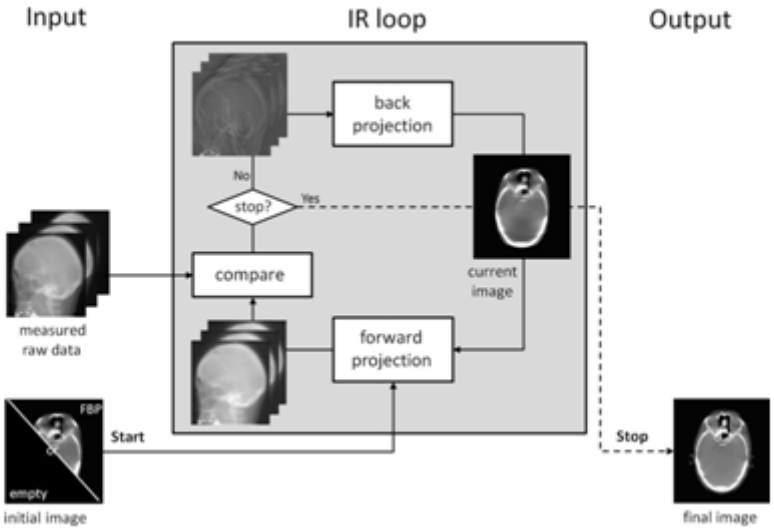

Figure 1.6: Iterative reconstruction process (Beister, Kolditz and Kalender, 2012)

The iterative reconstruction algorithm requires extensive computer power, as the computation time is long and it takes time when all of the projection views are used in each iteration to reach a solution (Powsner, Palmer and Powsner, 2013). Iterative reconstruction is slow compared to filtered back projection, however, filtered back projection amplifies statistical noise, affecting image quality (Powsner, Palmer and Powsner, 2013).

In most of the modern PET/CT systems a technique based on the maximum likelihood expectation maximization (MLEM) algorithm is implemented to speed up the iterative reconstruction process. This algorithm is called ordered subset expectation maximization (OSEM) (Powsner, Palmer and Powsner, 2013). The OSEM algorithm is an adaptation of the conventional MLEM (Guerra, 2004). To shorten the processing time, projection sinograms from the estimated and original datasets are grouped into small subsets or groups of projection views to perform expectation maximization on each subset (Cherry, Sorenson and Phelps, 2012; Chuang et al., 2005).

One iteration of OSEM is defined as a single pass through all specified subsets. In contrast to one MLEM iteration, the image update in OSEM is performed after each subset, that means n times if n is the number of ordered subsets. Computation time for the multiple image updates through all of the ordered subsets is nearly identical to one MLEM iteration. On the other hand, the reconstructed image after one OSEM iteration through n subsets is comparable to an image after n MLEM iterations.

Advantages of MLEM over the FBP are that it (1) does not require equally spaced projection data, (2) can use an incomplete set of projection data, and (3) yields fewer artefacts. The main limitations of the MLEM reconstruction algorithms are its slow convergence rate and the high computational cost of its practical implementation (Chuang et al., 2005).

Another accelerated iterative algorithm is the row action maximum likelihood algorithm (RAMLA). RAMLA was developed similar to OSEM as a faster alternative to the MLEM algorithm, maximizing the Poisson likelihood in the emission computed tomography (Herman and Meyer, 1993). This algorithm is based on an algebraic reconstruction technique (ART), and as investigated by Herman and Meyer (1993), offers extensively better image quality than many iterations of expectation maximization (EM).

Recently there has been an implementation of the LOR RAMLA algorithm on the Gemini (Philips Medical System, Cleveland, Ohio, USA) with an integrated geometric correction. It provides improved spatial resolution and reduced noise levels in reconstructed images (Groheux et al., 2009).

1.5 Image Quality

The quality of PET/CT images acquired with a given statistics is determined by the process used to reconstruct the images and interpreted by different parameters such as contrast, spatial resolution, scanner sensitivity, and tomographic uniformity (Francis et al., 2016).

These statistics of the acquired counts depend on the detector system, injected activity, scan duration, and the data acquisition protocol (Fukukita et al., 2010).

Most PET scanners have high sensitivity which allows the detection of a small amount of radiotracer, nonetheless in comparison to CT, the spatial resolution is weak (Bettinardi et al., 2014). Spatial resolution is the distance by which two small point sources of radioactivity must be separated to be differentiated as separate in the reconstructed image (Bushberg et al., 2012).

The spatial resolution of a PET imaging system is characterised by its point spread function (PSF), i.e. the response of the imaging system to a radioactive point source (Bettinardi et al., 2014). PSF characterizes an imaging system by constructing the response of the system on the input as in figure 1.7.

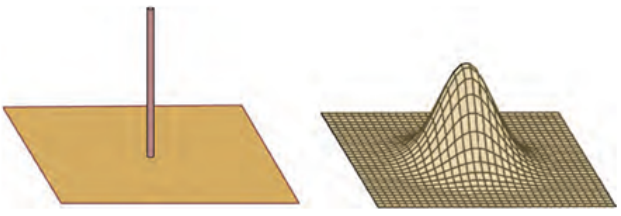

Figure 1.7: A point source as viewed in two dimensions (left); the response of the imaging system as characterized by the point spread function (right) (Bushberg et al., 2012)

The characterization of spatial resolution involves measuring the width of the point spread function, defined as the full width at half maximum (FWHM) (Bettinardi et al., 2014). Spatial resolution in PET is limited mainly by the detector size as it plays a role in determining the resolution due to the solid angle as the position of interaction within the crystal is not determined, however, the smaller the cross–sectional size the better the resolution (Moses, 2011).

Constraints due to the limited spatial resolution described above results in partial loss of intensity, and the activity around the structure appears to be smeared over a larger area than it occupies in the reconstructed image (Saha, 2010). These smearings occur on hot spots nearer cold background that are smaller than twice the resolution of the scanner (Saha, 2010).

The reconstructed image in PET should depict the radiotracer distribution accurately throughout the field of view (FOV), however, the constraints introduce hot spots near cold background (Saha, 2010), resulting in blurring (Bettinardi et al., 2014). The blurring due to limited spatial resolution reduces the image contrast thereby limiting the detectability of small lesions and preventing precise anatomical localisation of focal radiotracer uptake (Bettinardi et al., 2014). This reduction in image contrast between high and low uptake regions, would result in an underestimation and overestimation of activities around smaller structures in the reconstructed images. This is known as partial volume effect (PVE) (Saha, 2010).

Correction needs to be applied for overestimation or underestimation of activities to smaller structures in the reconstructed images. Many PVE corrections have been proposed in the literature, to improve PET image quality and quantitative accuracy

(Bettinardi et al., 2014), however, these methods are suitable for visual analysis but currently not for the absolute quantification of lesion uptake (Soret, Bacharach and Buvat, 2007).

1.6 Problem Statement

The proposed research is significant in Nuclear Medicine as most scans take a long time to acquire, thus contributing to the discomfort of the patient, increasing the likelihood of motion artefacts and further degrading the image quality.

In PET, high image quality is essential for precise diagnosis, however, PET image quality is limited in obese patients due to increase in photon attenuation and high scatter fractions (Taniguchi et al., 2015). Kangai and Onishi (2016) suggested the quality of clinical ^{18}F–FDG PET images from the overweight patient can be enhanced only by increasing the administered amount of radioactivity or by extending the acquisition time.

Increasing the administered activity is limited because it results in a higher rate of positron annihilations and gamma emissions thereby increasing random coincidences and possible counting losses caused by dead time and pile–up effects on detectors (Karakatsanis, Fokou and Tsoumpass, 2015). Pulse pileup takes place at high count rates when two equal light pulses occur close together in time so that the system perceives this as one event with twice the energy present (Mettler and Guiberteau, 2012).

Pulse pileup changes energy information contributing to counting losses (dead time) of the detection system as two pulses are counted as one (Cherry, Sorenson and

Phelps, 2012). Dead time refers to the failure of the detector to process more than one coincidence event at a time, whereby additional coincidence events are not captured as the detector is saturated and ineffective in processing those events (Cherry, Sorenson and Phelps, 2012).

To characterize the count rate performance of the PET scanner at high activity, the correlation between the administered dose, random events, dead time loss and the noise equivalent count rate (NECR) needs to be determined (Ahasan et al., 2011).

As the rate of photons hitting a detector increases, the probability of missing a photon due to detector dead time increases (Turkington, 2001).

To interpret PET/CT clinical images, both visual and quantitative images are needed. The image can be analysed visually by identifying structures that have anatomical and metabolic changes, which may indicate an active tumor. The standardized uptake value (SUV) is used to analyse the image by evaluating the metabolism of the lesion (Krempser et al., 2013). The SUV is a significant calculable measure of normalized radioactivity concentration in PET images.

The SUV is a widely used measure of tracer accumulation in PET studies, and normalizes the measured activity concentration to the injected activity per gram body mass (Von Schulthess, 2007), by the expression,

$$SUV = \frac{A[kBq]/cc}{D[kBq]} mass[g] \tag{1.1}$$

where A is the tissue activity and D is the injected dose, both decay corrected to the same time point.

The SUV can, amongst others be reported in two way namely,

- $\mathrm{SUV}_{\mathrm{mean}}$ defined as the mean SUV of all voxels within a specified ROI.
- $\mathrm{SUV}_{\mathrm{max}}$ defined as the voxel with the highest SUV within the defined region.

The quantification of PET/CT images using the SUV is affected by the image reconstruction, filtering techniques, and partial volume effect. Scattered and random coincidences add image background counts that contribute to SUV uptake (Mettler and Guiberteau, 2012).

The objective of PET image improvement is to limit the negative effect of noise by increasing the number of detected true coincidences relative to scatter and random coincidences (Cherry, Sorenson and Phelps, 2012). Both true coincidence and scatter rates are increased in three dimensional (3D) acquisition mode (Shreve and Townsend, 2011). 3D acquisition mode provides a higher sensitivity of the detector system and, thus, a higher temporal resolution could be feasible using shorter frame durations in dynamic 3D acquisition mode. Improving image quality with 3D acquisition mode needs an accurate elimination of scatter and random events (Mettler and Guiberteau, 2012), which is still a challenge for PET image reconstruction.

In PET imaging, the NECR describes the true coincidence rate that would give the observed signal to noise ratio (SNR) if there were no random and scatter coincidences (Antić and Haglund, 2016). Administering high activity establishes high count rates causing pulse pileup thereby affecting the spatial resolution in common PET scanners, and also impacts the timing resolution of the time of flight (ToF) (Surti et al., 2007).

Masuda et al. (2009) suggested that the quality of the PET images acquired from heavier patients be maintained by scanning for longer periods, as administering high activity increases the dose to the patient and did not improve the quality of PET/CT images with LSO detectors. Karakatsanis, Loudos and Nikita (2009) argued that increasing the acquisition time can limit the number of PET studies performed in a facility per day and also increases the probability of patient stress and motion artifacts.

Due to arguments presented by Antić and Haglund (2016), too much radioactivity increases random coincidences and dead time thereby adding image noise. Karakatsanis, Fokou and Tsoumpass (2015) concluded that the image quality of obese patients is primarily controllable by optimizing the acquisition time.

1.7 Study Aim and Objectives

The aim of this research study was to optimize image quality for Gallium–68 (^{68}Ga) scans under the constraint that the administered dose to a patient and acquisition duration time is limited. In this study, research was focused on the impact of image reconstruction and acquisition time on image quality, $\mathrm{SUV}_{\mathrm{max}}$, and lesion volume delineation for whole body PET/CT.

The objective to pursue this research arised from the requirement to shorten the scan acquisition time and to be able to do more scans with the same amount of ^{68}Ga activity at the WCAPC of Tygerberg Hospital.

Chapter 2

Literature Review

The literature review was performed using Pubmed as a search engine, focusing on specific journals and relevant books in the Stellenbosch University library. The specific journals were Journal Frontiers Biomedical Technologies, Journal of Nuclear Medicine, European Journal of Nuclear Medicine and Molecular Imaging, and Journal of Nuclear Medicine Technology. The literature cited was from 1993 onwards.

2.1 Optimizing Acquisition Time in PET/CT

Akamatsu et al. (2014) evaluated the PET image quality of a 39 ring and 52 ring time of flight (TOF) PET/CT scanner and also assessed the possibility of reducing the whole body scanning time using a 52 ring TOF PET/CT scanner. Two types of Biograph mCT scanners (Siemens Healthcare), one having a 39 ring detector and the other with a 52 ring detector, were used for this study. Both scanners have four rings of 48 LSO detector blocks.

The measured peak NECR for LSO block detectors was measured to be 180 ± 0.6 kBq/ml (Jakoby et al., 2011). A NEMA body phantom filled with a ^{18}F solution containing background activity of 5.31 and 2.65 kBq/ml incorporating a sphere to background ratio of 4:1 was used for this study. The PET data were acquired for 10 min in 3D–list mode. Data were extracted from 1 to 10 minutes and reconstructed using the ordered subsets reconstruction maximization plus the point spread function plus time of flight algorithms. PET images were physically assessed using the sensitivity, noise equivalent count rate coefficient of variation of background, and relative recovery coefficient. The group found the total sensitivity of the 39 and 52 ring scanners as 5.6 and 9.3 kcps/MBq. The noise equivalent counting rate of the 52 ring scanner compared to the 39 ring scanner, was 60% higher for both low and high contrast. The RC% and the COV% were consistent for both ring scanners. The image quality of the 52 ring scanner was better than that of the 39 ring system. The group further concluded that the acquisition time per bed position of the ring system can be reduced by 25% without compromising image quality.

Oliveira et al. (2018) investigated the shortest acquisition time without compromising the image quality in both a NEMA body phantom and patients, using a ToF PET/CT scanner and ^{68}Ga radionuclide. The group used the Gemini TF 16 PET/CT system (Philips Medical Systems), which is a high–performance 3D PET scanner with a peak NECR of 125 kcps at 17.4 kBq/ml (0.47) and a CT scanner (Brilliance model) of 16 slices (Soret, Bacharach and Buvat, 2007). Oliveira (2016, p. 30) regards the equipment to have a LYSO scintillator with a timing resolution of 575 ps and a spatial resolution near the centre of about 4.8 mm. The scanner was adjusted to operate as would be typical for patient studies, including the radionuclide. Oliveira (2016, p. 34) reconstructed the images using a 3D RAMLA algorithm, and used default parameters in routine clinical whole body image

reconstructions. The four smallest spheres of the NEMA phantom were filled with ^{68}Ga to simulate hot lesions. The background had an activity typical of the nature of what is seen in patient studies (5.3 kBq/ml) and the hot spheres were filled with activity concentration 8 times that of the background. Clinical images of a patient after administration of ^{68}Ga labeled PSMA were acquired for 30, 45 and 80 seconds per bed position in the upper abdomen, including the liver, spleen, heart, kidneys, bowel and the vertebras. Images of the NEMA phantom were acquired at 30, 45, 60, 80, and 120 s per bed position. The images were acquired with a hybrid system ToF PET/CT (Gemini TF 16, Philips). The clinical and NEMA phantom images were reconstructed using RAMLA. The group analyzed parameters such as noise, signal to noise ratio, contrast, contrast to noise ratio, and volume recovery coefficients. The quantification in terms of SUV was also analyzed. The group concluded that it is possible to decrease the acquisition time below 2 minutes per bed position without compromising the detection of the spheres of the NEMA phantom. A time between 45 and 60 seconds per bed position was proposed for future clinical practices, allowing more scans per day. Ahangari et al. (2015) investigated the impact of PSF reconstruction on PET acquisition time using a GE Discovery–60 PET/CT scanner with 64–slice CT. The group evaluated whether a reduction in acquisition time would be in agreement with the accuracy of quantitative measures using a PSF algorithm. Experiments were performed using an image quality NEMA phantom containing six inserts with 4:1 lesion to background ratio. A whole body FDG PET/CT scan of 17 patients with different primary cancers were also used in this study. NEMA phantoms were reconstructed in 3 iterations, 24 subsets with acquisition times varying from 180, 150, 120, 90 to 60 s. Both phantom and clinical images were analyzed by calculating coefficient of variation, a contrast to noise ratio and recovery coefficients. PET/CT image quality showed improvement in lesion detection and quantitative accuracy with PSF

algorithm. In addition better edge detection was achieved for smaller focal points, and acquisition time was reduced with no loss of image quality and quantitative accuracy when PSF was incorporated.

Hausmann et al. (2012) investigated the impact of acquisition time on image quality, lesion detection rate, SUV, and lesion volume for ^{18}F–FDG PET in cancer patients. The study was conducted over 7 months and 33 cancer patients were included in this study. In these 33 cancer patients, 63 lesions were independently identified. Two consecutive whole body ^{18}F–FDG PET/CT scans were performed, using a 3 min and 1.5 min acquisition time per bed position. Lesions were visually identified by the 2 nuclear medicine specialists and compared using a 5 point Likert–type scale to assess the image quality. The lesion volumes and SUV of the primary tumour, lymph nodes, and metastases were determined and also compared. Results indicated that all relevant lesions could be identified at both acquisition times, however, image quality was affected by an acquisition time of 1.5 min and was good in only 85% of these scans. The results also showed the quality of lesion visualization was excellent regardless of the acquisition time. The group used the Pearson correlation coefficient to look at the correlation between lesion volume and $\mathrm{SUV}_{\mathrm{max}}$ value on the PET images, and it showed an excellent correlation of 0.99 and 0.97 between the two acquisition times. Hausmann et al. (2012) concluded that even though the image quality was slightly poorer, the acquisition time could be reduced to 1.5 minutes, still being clinically useful without decreasing the lesion detection rate.

Umeda et al. (2017) explored the optimization of a shorter variable–acquisition time for legs to establish a code at achieving true whole–body PET/CT images. Their aim was to look at PET images as a function of acquisition time for legs of different

sizes and shorten the acquisition time to achieve better qualitative and quantitative accuracy of true whole–body PET/CT images. The Discovery PET/CT 600 Motion Vision scanner combined with a 16–multislice CT scanner (GE Healthcare, Milwaukee, WI, USA) was used for this study. The PET scanner has no time of flight capability and comprises of 12 288 bismuth–germanate (BGO) crystal elements with a volume of 4.7x6.3x30 mm^3 each and a total of 256 BGO detector blocks covering axial and transaxial FOV of 15.3 and 70 cm. The study analyzed PET images of a NEMA phantom and three plastic bottle phantoms (axial length 5.69, 8.54, and 10.7 cm) that simulated the human body and legs. The diameters of legs to be modeled as phantoms were defined based on data derived from 53 patients. The phantoms comprised two spheres (diameters, 10 and 17 mm) containing ^{18}F–FDG solution with the sphere to background ratios of 4 at a radioactivity level of 2.65 kBq/ml. All PET data were reconstructed with acquisition times ranging from 10 to 180, and 1200 seconds. The group evaluated the images and determined the coefficient of variance of the background, contrast and quantitative percentage error of the hot spheres, and then determined two shorter variable–acquisition protocols for legs. Lesion detectability was evaluated and quantitative accuracy determined based on SUV_{max} in PET images of a patient using the proposed protocols. A larger phantom and a shorter acquisition time resulted in increased background noise on images and decreased the contrast in hot spheres. The quantitative % errors of the 10 and 17 mm spheres in the leg phantoms were $\pm 15\%$ and $\pm 10\%$ respectively in PET images with a high coefficient of variation (scan $<$30s). The SUV_{mean} of three lesions using the current fixed acquisition and two proposed shorter variable acquisition time protocols in the clinical study were 3.1, and 3.2, which did not differ significantly. Leg acquisition time per bed position of even 30–90 s allowed axial equalization, uniform image noise and a maximum $\pm 15\%$ quantitative accuracy for the smallest lesion. The

general acquisition time was reduced by 23–42% using proposed shorter variable acquisition time than the current fixed acquisition time for imaging legs, indicating that this is a useful and practical protocol for routine qualitative and quantitative PET/CT assessment in the clinical setting. All these publications indicate that an acquisition time reduction seems to be possible for clinical routine.

Only one study evaluated ^{68}Ga–PET/CT with default reconstruction and a contrast and background preparation of the NEMA whole body image quality phantom like NEMA recommends it for ^{18}F–PET/CT (Oliveira et al., 2018).

Chapter 3

Materials and Methods

The study was performed at the Western Cape Academic PET/CT centre (WCAPC) in the Division of Nuclear Medicine (Tygerberg Hospital).

3.1 PET/CT Scanner

A Gemini TF Big Bore hybrid PET/CT system scanner manufactured by Philips was used to acquire the images of the NEMA phantom. The system comprises a Brilliance CT and PET system, the latter containing a ring detector system with 420 blocks of 4x4 mm^3 LYSO scintillator crystals of a dimension of 4x4x22 mm^3. The axial FOV of the PET detector ring is 18 cm. The CT is a 16 slice Brilliance system having a slice width of 0.75 mm with the fastest rotation of 0.5 seconds. The patient port of the hybrid system has a diameter of 85 cm and a transverse field of view of 60 cm (Surti et al., 2007).

This scanner is a fully 3D scanner with an energy resolution of 11.5% (FWHM) at 511 keV and an energy window setting of 440 and 665 keV (Surti et al., 2007).

Its temporal resolution measured with a low activity point source in air is 585 ps (FWHM). It has the capability of implementing the TOF technique. The PET crystal detectors are arranged in a pixelated Anger–logic design (Surti et al., 2007).

3.2 Ethics

The study was approved by the Health Research Ethics committee 2 of the Faculty of Medicine and Health Sciences of Stellenbosch University (Reference S/19/05/089). No patient consent was needed as only patients' imaging records were used. All patients records were handled confidentially and identifying details such as the name and the hospital number of the patients were not recorded. A waiver of informed consent was obtained due to the low risk nature of the study.

3.3 Materials

3.3.1 Patient selection

This study included the imaging records of 80 patients who had undergone whole body (WB) PET/CT using ^{68}Ga DOTANOC for oncological imaging on the Philips system at the WCAPC between March 2017 and May 2019. Patients were selected to get a homogeneous distribution over the time period but without any inclusion or exclusion criteria, independent from any patient information. The patient data sets were analyzed for this study to plan phantom measurements which simulate a typical activity distribution like in the patient scans.

The WB PET/CT imaging was done 60 min after the injection of ^{68}Ga–DOTANOC with a scan duration that usually took about 2 to 5 min per bed position. ROIs were drawn on the normal liver, thigh muscle and heart areas. ROIs were also drawn on multiple lesions in the liver of 21 patients with SUV_{max} measured. To get an equivalent number of ROIs values for lesions, only twenty one patients were necessary to define the appropriate ROIs and to quantify an average of SUV_{max}.

Results of the patient data analysis were used to prepare the phantom for measurements with activity and concentration, similar to clinical situations.

3.3.2 Phantom

Data were acquired using the NEMA phantom with a volume of 9.18 litres and comprised of six spheres with internal diameters of 10, 13, 17, 22, 28 and 37 mm imitating tumors of differing sizes. The phantom is designed following the International Electrotechnical Commission (IEC) recommendations and the modification done by NEMA. The NEMA describes a series of standards for characterizing the performance of radionuclide imaging (DeWerd and Kissick, 2014). This phantom is recommended for the evaluation of reconstructed image quality in WB PET imaging.

3.4 Image Reconstruction

The PET part of the Gemini TF big bore hybrid PET/CT has an impressive computing platform that can carry out fully 3D PET iterative reconstruction algorithms (LOR based list mode reconstruction). This computing platform utilizes a 5–node quad–core CPU cluster, thereby making it possible to integrate image

processing to continue in parallel with data acquisition.

Image processing using the NEMA phantom took about 5 minutes after the end of the acquisition. The phantom images were attenuation corrected using a CT operating as for a typical patient scan to improve accuracy and uniformity. For PET/CT phantom reconstruction, the same reconstruction protocol used for clinical studies at the WCAPC was used as the reference. This protocol reconstructs a WB image with a voxel size of 4x4x4 mm^3 using a 3D LOR spherically symmetric basis function ordered algorithm (BLOB–OS–TF) with ToF information representing the emissions. The default reconstruction uses 3 iterations and 33 subsets with a relaxation parameter lambda (λ = 1.0) which is labeled as smoothing filter ”normal” in the vendor software.

Image filtering or smoothing is applied to reduce the effects of noise on image analysis. In addition to the default parameter λ = 1.0, a selection of smoothing filters with relaxation parameters λ = 0.7 (smooth), λ = 0.5 (smooth A) and λ = 0.3 (smooth B) were used to reconstruct the list mode raw data.

PET raw data were also reconstructed using a small voxel of 2x2x2 mm^3 (head and neck (HN) imaging protocol) with smooth B smoothing applied.

Table 3.1 illustrates these reconstructions with different reconstruction parameters applied for high contrast (HC) and low contrast (LC). In total, 63 images with different frame duration (30, 60, 90, 120, 150, 180 and 300 s), different smoothing filtering and voxel–size were generated.

Table 3.1: Different frame duration, with smoothing filters and voxel–size

Scan Type Duration	LC (4 mm): 6 spheres Background 1	HC (4 mm): 6 spheres Background 2	HC (2 mm): 6 spheres Background 2
300 s	normal, smooth smooth A, smooth B	normal, smooth smooth A, smooth B	smooth B
180 s	normal, smooth smooth A, smooth B	normal, smooth smooth A, smooth B	smooth B
150 s	normal, smooth smooth A, smooth B	normal, smooth smooth A, smooth B	smooth B
120 s	normal, smooth smooth A, smooth B	normal, smooth smooth A, smooth B	smooth B
90 s	normal, smooth smooth A, smooth B	normal, smooth smooth A, smooth B	smooth B
60 s	normal, smooth smooth A, smooth B	normal, smooth smooth A, smooth B	smooth B
30 s	normal, smooth smooth A, smooth B	normal, smooth smooth A, smooth B	smooth B

3.5 Methodology

To develop this experimental investigation, two phases were performed, (a) Patient data of 80 patients who underwent ^{68}Ga DOTANOC PET/CT WB scans were collected, to measure image quality parameters in different organs (thigh muscle, liver, heart) and lesions in the liver, (b) NEMA phantom prepared according to what would have been measured in the 80 patients.

3.5.1 Patient data

Images were analyzed from patient records available at the WCAPC using Hermes Medical Systems Hybrid Viewer Software. The use of ROIs in Hermes Hybrid Viewer software allowed the extraction of the following voxel values in the ROI: (a) mean, (b) maximum, (c) median. It also provided the standard deviation and the $\mathrm{SUV_{max}}$ of all voxels in the ROI.

ROIs in the liver, thigh muscle and heart were drawn and SUV values measured as in figure 3.1. The $\mathrm{SUV_{mean}}$ values were obtained from homogenous tracer accumulation in PET studies of patients with normal/healthy tissues as in figure 3.1 (a), and $\mathrm{SUV_{max}}$ on liver with lesions as in figure 3.1 (b). These values assisted in ascertaining what background activity concentration must be prepared in the phantom to produce images simulating patients with lesions of different sizes in and outside the liver.

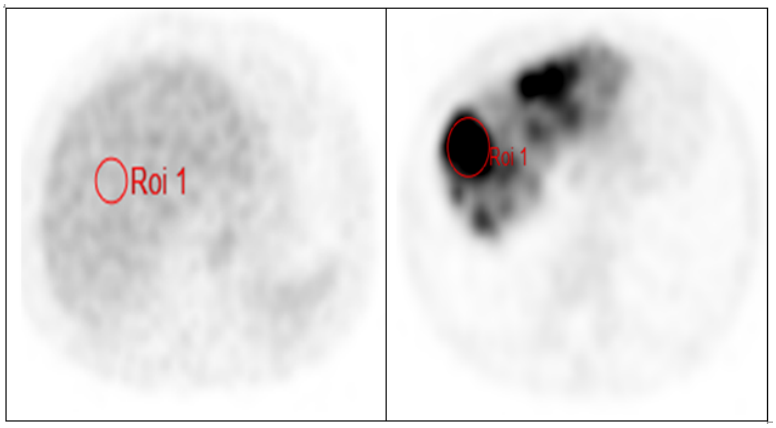

Figure 3.1: ROIs drawn on (a) homogenous normal liver, and (b) lesions in the liver.

The ROIs were manually placed within an area of normal uptake of ^{68}Ga DOTANOC in the liver, thigh muscle and heart with SUV_{mean} measured on fifty nine patients. Fifty nine ROIs on lesions of twenty one randomly selected patient records were identified with SUV_{max} values averaged and quantified.

3.5.2 Phantom preparation and data collection

The NEMA phantom measurement was prepared under two contrast conditions,
(i) High concentration representing areas outside the liver averaged between the heart, thigh muscle and lesions in the liver; (ii) Low concentration representing lesion in the liver and normal uptake in the liver.

Three activities of ^{68}Ga were prepared for this phantom measurement. An amount of 7.7 MBq ^{68}Ga was measured with a tuberculin syringe, calibrated in a PTW Curiementor 3 dose calibrator 24 minutes before the start of the first acquisition. This activity was injected in a 200 ml stock solution, 1 ml of water was firstly removed from the stock solution using a B-D Plastipak syringe and replaced with injected activity to make it 200 ml once more.

The solution was stirred for a while, and using a syringe an activity was withdrawn from the solution and injected into each of the small spheres. At time of imaging (24 minutes after preparation of the stock solution), activity concentration in the sphere was 30 kBq/cc. The second syringe with an activity of 8.4 MBq was flushed in a 9.18 litre volume of the NEMA phantom 18 minutes before the first scan. This volume would have an activity concentration of 0.7 kBq/cc, making a contrast of 1 to 42.3 at the time of scan, representing high contrast ratio.

To ensure uniform mixture between activity and water the phantom was tilted, rotated on a swivel chair so no air inside as bubbles could interfere with the measurement of the recovery coefficient. The phantom was placed horizontally on the imaging table for hot spheres to be localized at the centre of the field of view in the Z-axis. Attenuation correction was performed using a CT scanner.

After the first scan, the third activity was flushed into the NEMA phantom volume background and shaken using a swivel. Attenuation correction was also performed and data acquisition performed for 5 minutes in 3D list mode. The third activity of 44.6 MBq was prepared using a tuberculin LYSA syringe and calibrated on a PTW Curiementor 3 dose calibrator. This activity was injected in the phantom volume just after the first scan making the activity concentration to be 4.3 kBq/cc and of the spheres to be 25.5 kBq/cc at the time of the scan. The phantom was positioned and aligned on the imaging table, centered on the transverse and axial FOV of the Gemini TF big bore PET/CT system. The contrast for the second scan was 1 to 5.9 making it a low contrast simulating lesions in the liver. Attenuation correction was also performed and data acquisition performed for 5 minutes in 3D list mode.

3.6 Data Processing

All images were reconstructed and corrections and smoothing levels applied. NEMA NU2-2007 protocol recommendations were used for assessing image quality (NEMA NU 2 2007, 2007). This protocol illustrates and instructs that twelve concentric circular ROIs with diameters equal to the physical internal diameter of the spheres should be drawn to measure the activity concentrations of the background regions and the spheres as in figure 3.2.

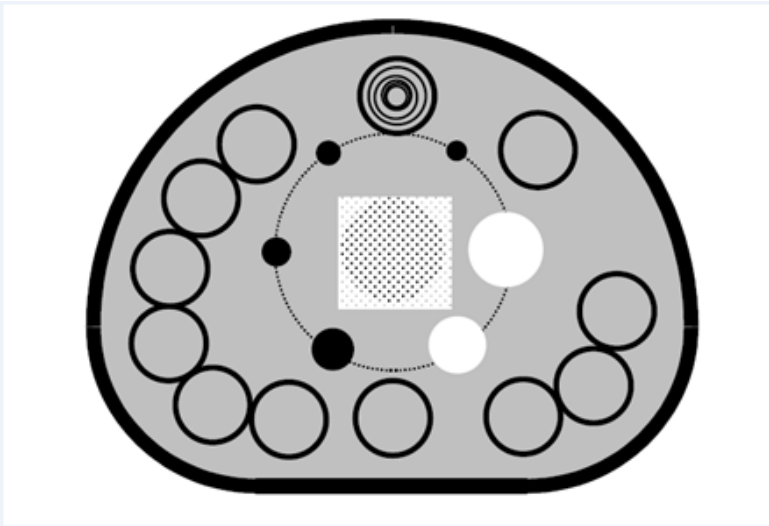

Figure 3.2: Example of ROIs drawn in PET image for activity concentration measuring in the spheres and background

The protocol further states that ROIs be drawn on each hot and cold sphere, and also 12 circular ROIs of the same sizes as on the hot and cold spheres be drawn in the background of the phantom on the central slice. Four other slices, two each on both sides of the central slice, approximately 1 cm and 2 cm from the central slice, were also drawn (NEMA NU 2 2007, 2007).

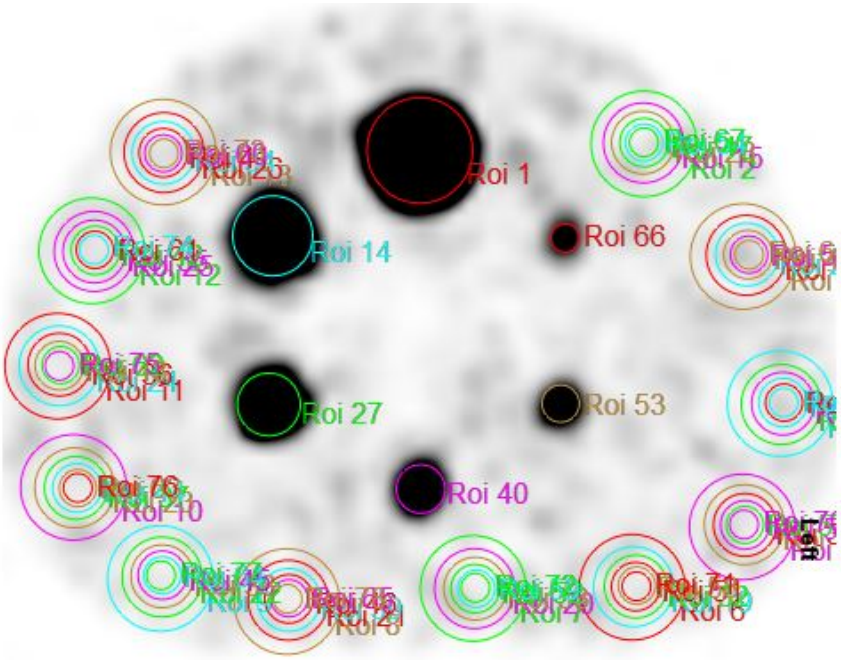

Figure 3.3: ROIs on hot spheres and background on a PET image

ROIs of 37, 28, 22, 17, 13 and 10 mm were drawn on each hot sphere and throughout as in the resulting image in figure 3.3, on central slice. The same procedure for the drawing of spheres were performed as explained above following the NEMA 2007 protocol, including on the other four slices. The activity concentrations in each image slice ROIs were recorded and used to evaluate the PET image quality by calculating the following;

- Signal to noise ratio (SNR) as

$$SNR = \frac{SUV_{\text{mnbkgrd}}}{SD} \tag{3.1}$$

where, $\text{SUV}_{\text{mnbkgrd}}$ refers to the average activity and SD to the standard deviation in the background ROIs.

- Contrast to noise (CNR) is an alternative for lesion detectability and is defined as,

$$CNR = \frac{SUV_{\text{maxsphere}} - SUV_{\text{mnbkgrd}}}{SD} \tag{3.2}$$

where, $\text{SUV}_{\text{maxsphere}}$ refers to the maximum activity concentration within a sphere.

- The recovery coefficient (RC%) obtained by dividing the measured activity concentration ($\text{SUV}_{\text{measured}}$) by the known activity concentration (A_{known}) in a region from images acquired with phantoms (Krempser et al., 2013) was also assessed using,

$$RC\% = \frac{SUV_{\text{measured}}}{A_{\text{known}}} \cdot 100\% \tag{3.3}$$

- The coefficient of variation (COV%) representing the existence in deviation of detected pulses from the expected pulse in a medical image is defined as,

$$COV\% = \frac{SD_{BG}}{C_{BG}} \cdot 100\% \tag{3.4}$$

C_{BG} the average activity in the background ROIs.

Chapter 4

Results

4.1 Data Analysis

Image quantitative analysis was performed using the Hermes Hybrid Viewer Software on PET reconstructed images using the different acquisition times. All graphical and statistical analysis in this thesis were performed using RStudio (version 1.8.2), and pgfplots (visualization tool by LaTex).

Patients results were divided into four groups, namely uptake in lesions in the liver, and uptake in thigh muscle, heart and liver. Figure 4.1 illustrates the measured activity concentration to be prepared for the NEMA phantom according to what would have been measured from the collected patient data. The extracted average SUV_{mean} values from 59 ROIs of patients with normal uptake of ^{68}Ga were determined to be 5.5 $\pm$ 1.4 kBq/cc, and SUV_{max} on 59 multiple lesions identified in 21 patients were quantified to be 26.9 $\pm$ 17.0 kBq/cc.

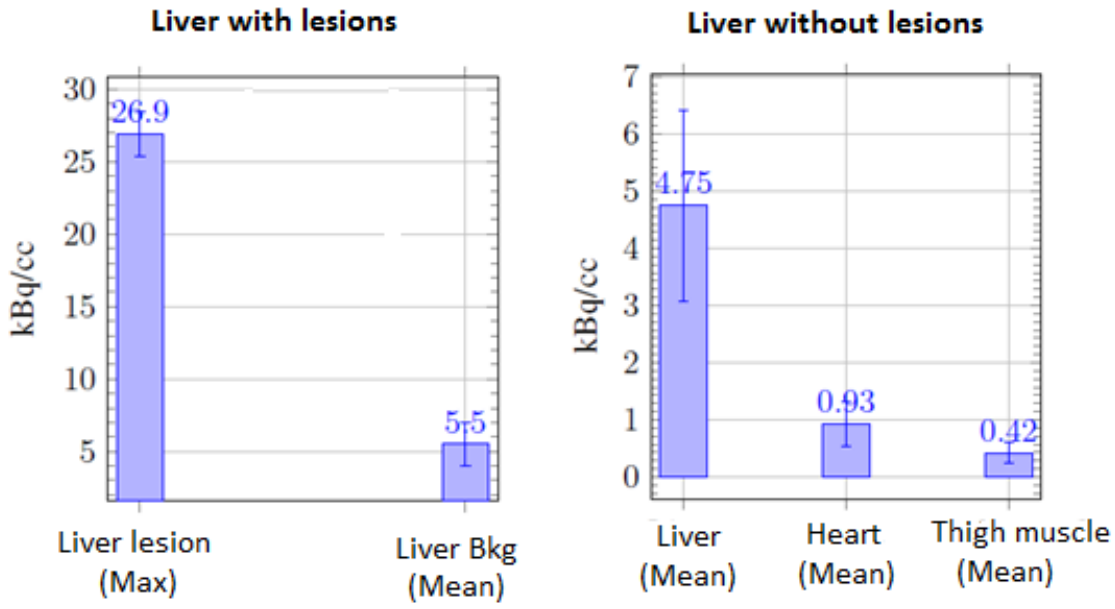

Figure 4.1: Activity concentration prepared in the NEMA phantom as derived from the patient data. Left: Max and mean uptake of the liver lesions, right: SUV_{mean} of normal tissue accumulation

The extracted SUV_{mean} and SUV_{max} from the patient data assisted in determining the mean, and maximum activity concentrations needed to prepare the phantom to simulate patients with varying lesion uptake as explained in Chapter 3. Table 4.1 lists the activity concentration and contrast for two phantom measurements derived from patient data analysis. The average value of normal liver tissue activity concentration over all patient data sets was 4.8 $\pm$ 1.7 kBq/cc, the average value of background muscle to be 0.4 $\pm$ 0.1 kBq/cc and for the heart 0.9 $\pm$ 0.4 kBq/cc averaged (muscle and heart) to be 0.7 $\pm$ 0.3 kBq/cc.

Table 4.1: Phantom preparation based on the results of patient data analysis

	Contrast 1	Contrast 2	Spheres (kBq/cc)	Background 1 (kBq/cc)	Background 2 (kBq/cc)
1st scan (t = 0)		41.5	28.1	0.7	
2nd scan (t = 30 min)	4.9		23.2		4.8

The activity concentration that needed to be prepared was determined to be 23.2 kBq/cc in the spheres and 4.8 kBq/cc in the background, for the contrast to be 4.9 rounded off to 5, with contrast being 5:1. This low contrast ratio represented lesions in the liver. The high contrast ratio needed for phantom preparation representing normal uptake of ROIs outside the liver (averaged between the heart and thigh muscle) and lesions in the liver was determined to be 41.5:1 ratio. NEMA phantom preparation representing high contrast needed the spheres to have 8.5 times the activity of the 5 background. Therefore the background activity was choosen to be 0.7 kBq/cc.

Figure 4.2 illustrates the phantom transaxial slices of PET images reconstructed using normal, smooth, smooth A and smooth B smoothing reconstruction parameters. These phantom images are representative of low contrast (5:1) lesion to background ratio. The acquisition times varied from 30 to 300 s (30, 60, 90, 120, 150, 180, and 300 s) to characterize, and optimize the effect of reducing clinical scanning times utilizing the PET component of the Gemini TF big bore hybrid PET/CT scanner. PET images with shorter acquisition time had increased

background noise, the 10 mm hot spheres in the reconstructed NEMA phantom images in figure 4.2 were unclear when the acquisition time was less than 150 s.

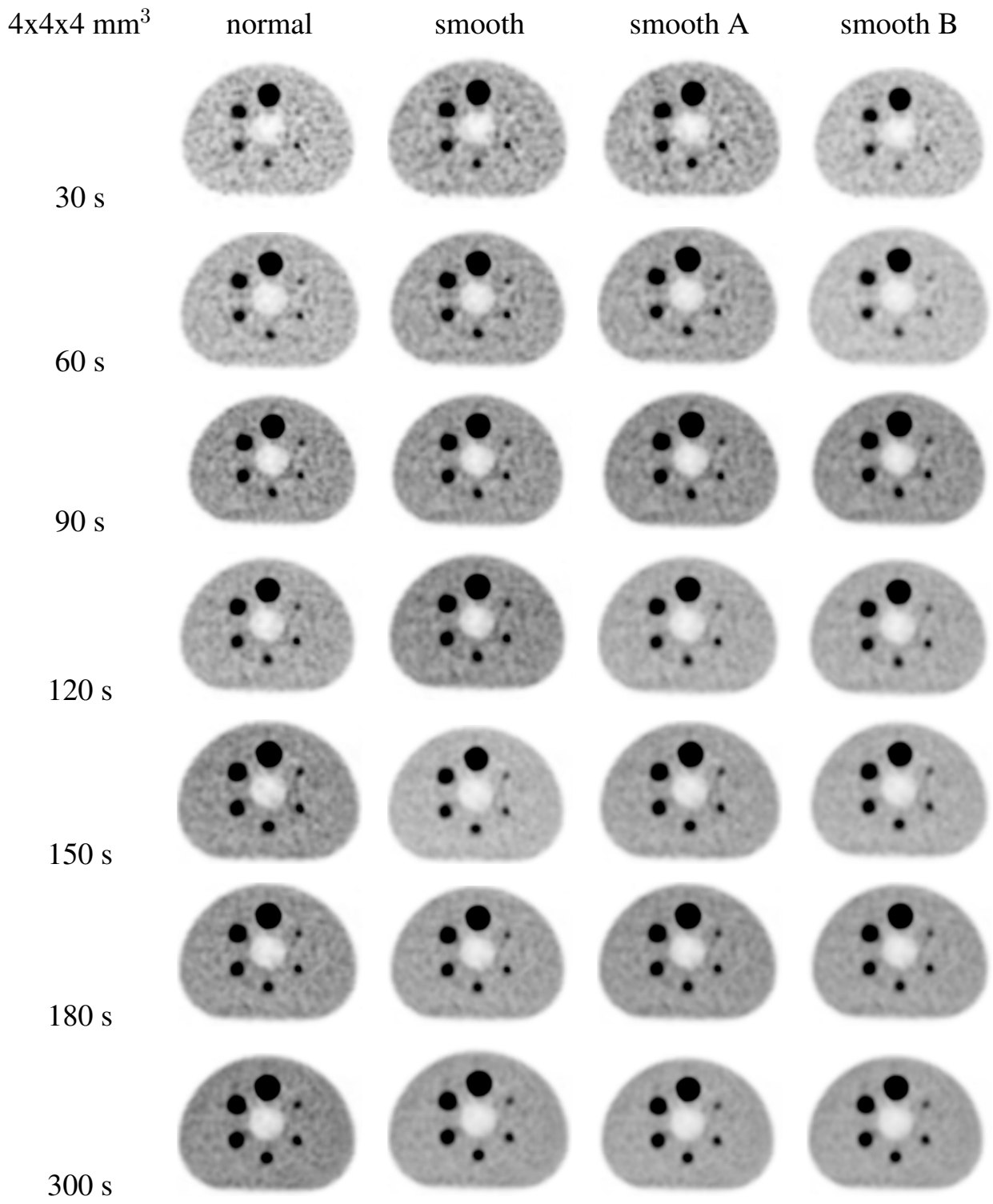

Figure 4.2: Central transaxial slice of the NEMA phantom with low contrast. PET images were reconstructed with the WB protocol (4x4x4 mm^3 voxel size).

The same smoothing parameters for low contrast were applied on high contrast

demonstrated by figure 4.3. A small voxel of 2x2x2 mm^3 reconstruction algorithm of head and neck (HN) imaging was also used with smoothing B applied.

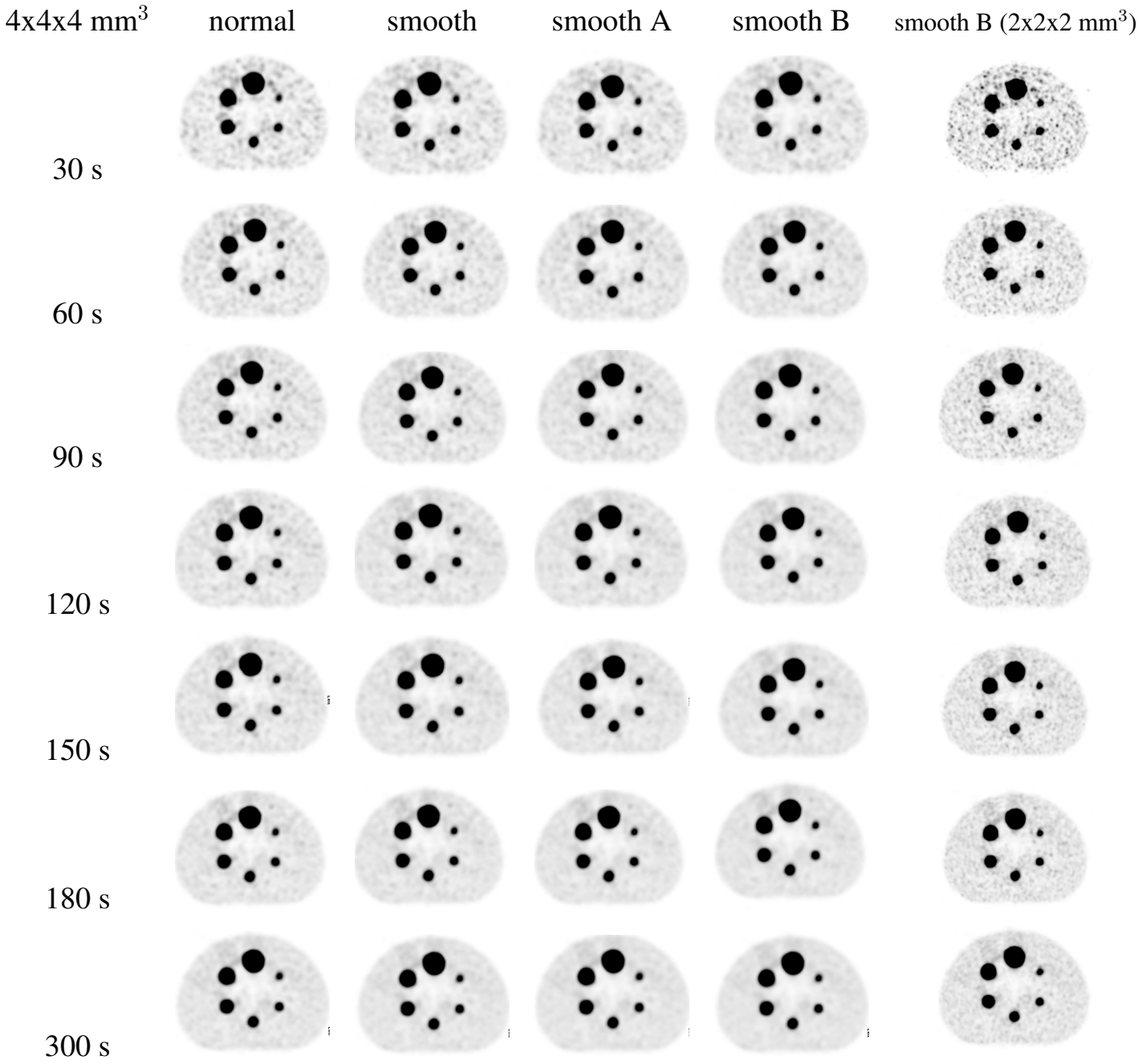

Figure 4.3: Central transaxial slice of the NEMA phantom with high contrast. PET images were reconstructed with the WB protocol (4x4x4 mm^3 voxel size) and using the HN protocol (2x2x2 mm^3).

On the reconstructed WB phantom the hot spheres were localized at the center of the field of view on slice 30 for low contrast. Twelve circular ROIs each of size 10, 13, 17, 22, 27, and 37 mm were drawn on the background on this center slice and

on slices 26, 28, 32 and 34.

The extracted mean activity concentration values of the ROIs from Hermes Hybrid Viewer Software were used to determine the average activity (C_{BG}), standard deviation (SD_{BG}), and COV%. Tables 4.2 to 4.8 detail the determined COV% phantom measurements with low contrast using different reconstruction parameters.

Table 4.2: COV% for 30 s of phantom measurement with low contrast

Sphere Diameter	**COV% 30 s scan**			
	normal	**smooth**	**smooth A**	**smooth B**
	WB	**WB**	**WB**	**WB**
37 mm	12.6 ± 0.2	10.8 ± 0.2	10.3 ± 0.2	9.9 ± 0.2
28 mm	12.8 ± 0.2	11.2 ± 0.2	10.5 ± 0.2	9.7 ± 0.2
22 mm	12.5 ± 0.2	11.0 ± 0.2	10.3 ± 0.2	9.6 ± 0.2
17 mm	12.5 ± 0.2	11.9 ± 0.2	10.6 ± 0.2	10.4 ± 0.2
13 mm	13.8 ± 0.2	13.9 ± 0.2	11.1 ± 0.2	10.9 ± 0.2
10 mm	15.7 ± 0.3	14.5 ± 0.2	13.3 ± 0.2	12.6 ± 0.2

Table 4.3: COV% for 60 s of phantom measurement with low contrast

Sphere Diameter	COV% 60 s scan			
	normal	**smooth**	**smooth A**	**smooth B**
	WB	**WB**	**WB**	**WB**
37 mm	8.3 ± 0.1	7.2 ± 0.1	6.7 ± 0.1	6.0 ± 0.1
28 mm	8.3 ± 0.1	7.2 ± 0.1	7.1 ± 0.1	6.3 ± 0.1
22 mm	9.1 ± 0.1	7.9 ± 0.1	7.1 ± 0.1	6.8 ± 0.1
17 mm	10.7 ± 0.2	9.4 ± 0.2	8.8 ± 0.1	8.0 ± 0.1
13 mm	11.9 ± 0.2	10.4 ± 0.2	9.6 ± 0.2	8.9 ± 0.2
10 mm	13.1 ± 0.2	11.4 ± 0.2	10.9 ± 0.2	10.4 ± 0.2

Table 4.4: COV% for 90 s of phantom measurement with low contrast.

Sphere Diameter	COV% 90 s scan			
	normal	**smooth**	**smooth A**	**smooth B**
	WB	**WB**	**WB**	**WB**
37 mm	7.1 ± 0.1	6.3 ± 0.1	5.9 ± 0.1	5.5 ± 0.1
28 mm	8.3 ± 0.1	7.4 ± 0.1	6.9 ± 0.1	.4 ± 0.1
22 mm	8.7 ± 0.2	7.8 ± 0.1	7.6 ± 0.1	6.9 ± 0.1
17 mm	9.4 ± 0.2	8.3 ± 0.1	8.1 ± 0.1	8.1 ± 0.1
13 mm	10.8 ± 0.2	9.7 ± 0.1	9.2 ± 0.1	8.6 ± 0.1
10 mm	12.1 ± 0.2	10.7 ± 0.2	10.2 ± 0.2	9.4 ± 0.2

Table 4.5: COV% for 120 s of phantom measurement with low contrast

Sphere Diameter	COV% 120 s scan			
	normal	**smooth**	**smooth A**	**smooth B**
	WB	**WB**	**WB**	**WB**
37 mm	6.5 ± 0.1	5.9 ± 0.10	5.7 ± 0.1	5.3 ± 0.1
28 mm	7.0 ± 0.1	6.0 ± 0.1	5.6 ± 0.1	5.4 ± 0.1
22 mm	7.4 ± 0.1	6.4 ± 0.1	6.3 ± 0.1	5.7 ± 0.1
17 mm	7.9 ± 0.1	6.6 ± 0.1	6.2 ± 0.1	5.9 ± 0.1
13 mm	9.4 ± 0.2	8.0 ± 0.1	7.6 ± 0.1	6.8 ± 0.1
10 mm	10.7 ± 0.2	9.3 ± 0.2	8.7 ± 0.1	7.9 ± 0.1

Table 4.6: COV% for 150 s of phantom measurement with low contrast

Sphere Diameter	COV% 150 s scan			
	normal	**smooth**	**smooth A**	**smooth B**
	WB	**WB**	**WB**	**WB**
37 mm	6.5 ± 0.1	5.9 ± 0.1	5.4 ± 0.1	5.2 ± 0.1
28 mm	6.1 ± 0.1	5.6 ± 0.1	5.4 ± 0.1	5.1 ± 0.1
22 mm	6.8 ± 0.1	6.3 ± 0.1	6.1 ± 0.1	5.8 ± 0.1
17 mm	6.9 ± 0.1	6.6 ± 0.1	6.3 ± 0.1	6.2 ± 0.1
13 mm	8.1 ± 0.1	7.5 ± 0.1	7.2 ± 0.1	6.8 ± 0.1
10 mm	8.6 ± 0.1	7.9 ± 0.1	7.6 ± 0.13	7.0 ± 0.1

Table 4.7: COV% for 180 s of phantom measurement with low contrast

Sphere Diameter	COV% 180 s scan			
	normal	**smooth**	**smooth A**	**smooth B**
	WB	**WB**	**WB**	**WB**
37 mm	4.6 ± 0.1	4.6 ± 0.1	4.3 ± 0.1	4.0 ± 0.1
28 mm	4.8 ± 0.1	4.8 ± 0.1	4.5 ± 0.1	4.2 ± 0.1
22 mm	5.2 ± 0.1	5.2 ± 0.1	4.9 ± 0.1	4.6 ± 0.1
17 mm	5.8 ± 0.1	5.8 ± 0.1	5.5 ± 0.1	5.2 ± 0.1
13 mm	6.4 ± 0.1	6.4 ± 0.1	6.0 ± 0.1	5.6 ± 0.1
10 mm	7.6 ± 0.1	7.6 ± 0.1	7.1 ± 0.1	6.6 ± 0.1

Table 4.8: COV% for 300 s of phantom measurement with low contrast

Sphere Diameter	COV% 300 s scan			
	normal	**smooth**	**smooth A**	**smooth B**
	WB	**WB**	**WB**	**WB**
37 mm	4.8 ± 0.1	5.3 ± 0.1	4.0 ± 0.1	4.9 ± 0.1
28 mm	5.7 ± 0.1	5.1 ± 0.1	4.7 ± 0.1	5.2 ± 0.1
22 mm	6.2 ± 0.1	5.6 ± 0.1	5.1 ± 0.1	4.9 ± 0.1
17 mm	6.5 ± 0.1	5.8 ± 0.1	5.4 ± 0.1	5.1 ± 0.1
13 mm	7.2 ± 0.1	6.4 ± 0.1	6.0 ± 0.1	5.7 ± 0.1
10 mm	7.0 ± 0.1	6.4 ± 0.1	5.9 ± 0.1	5.7 ± 0.1

The COV% data analyses for low contrast with different smoothing parameters on tables 4.2 to 4.8 indicate noise decreased as acquisition time increased, and noise further decreased with an increase in sphere diameter.

The behavior of COV% of all spheres at different acquisition times per field of view using selected reconstruction parameters is presented in figure 4.4. The measurements between different acquisition times were normalized in comparison to the 300 seconds reference scan. The 300 seconds scan is the acquisition time per bed position currently used at the WCAPC.

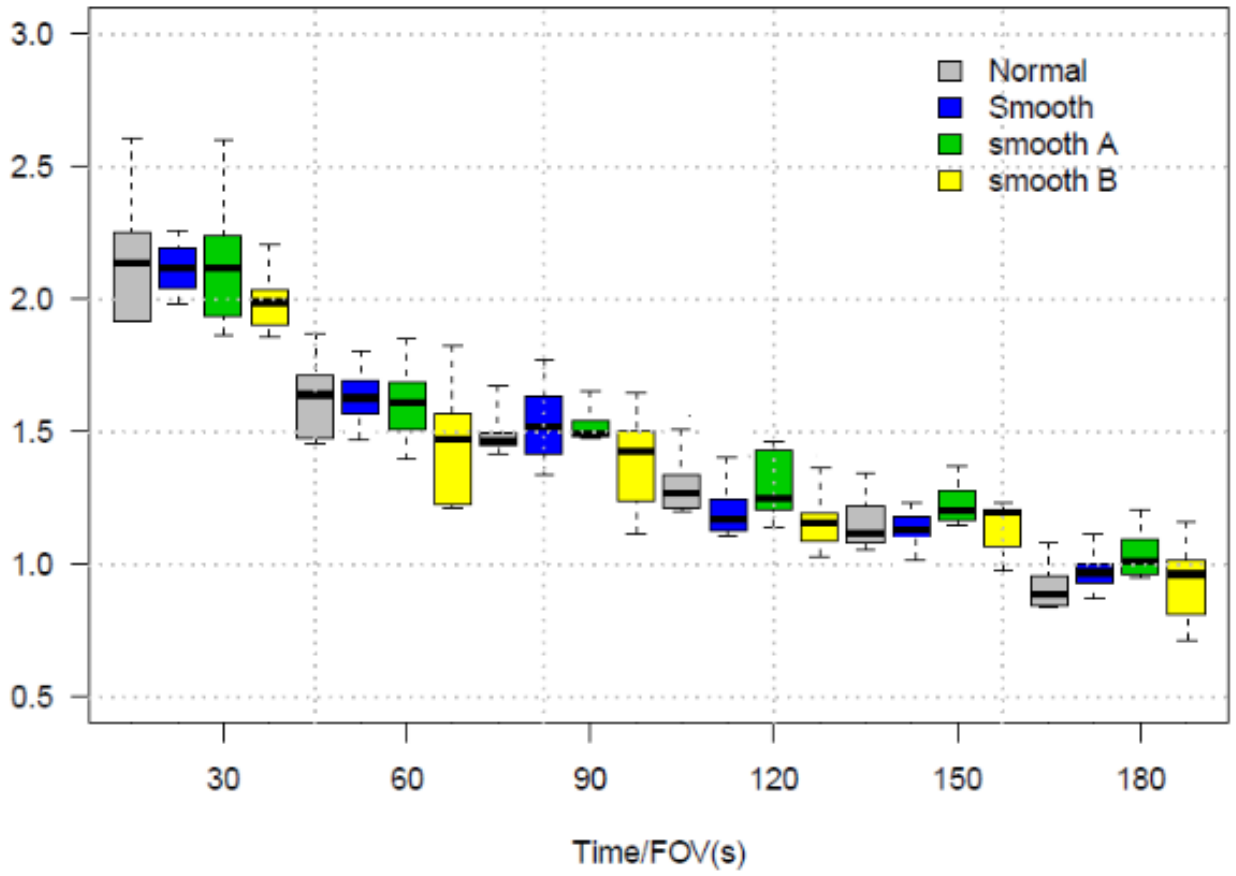

Figure 4.4: Bar plot of the COV% (low contrast) of all spheres for different frame duration times and smoothing filters compared to the 300 second reference scan for the WB reconstruction with voxel size of 4x4x4 mm^3

The results for COV% in figure 4.4 show that smooth and smooth A reconstruction parameters at 180 seconds compared to 300 seconds approached 1 indicating a small significant change in percentage agreement. The boxplot for smooth reconstruction parameter shows equal quantile group 2 and group 3 suggesting a high level of agreement of the data in each of the mentioned quantiles.

The data analyses results from the second experiment when evaluating COV% with high contrast are given in tables 4.9 to 4.15. The data using high contrast includes images reconstructed in WB algorithm with different parameters (normal, smooth, smooth A and smooth B) with a voxel size of 4x4x4 mm^3, and also reconstructed using head and neck HN algorithm with 2x2x2 mm^3 voxel size. For HN only the smooth B smoothing parameter was used.

As for low contrast, six ROIs of 10 , 13, 17 , 22, 28 and 37 mm were drawn on hot spheres centered on slice 29, sixty of the same size on the same slice and on slices 25, 27, 31 and 33 with WB image reconstruction using a voxel size of 4x4x4 mm^3. The centered spheres when using the head and neck algorithm were centered on slice 57 and 4 slices placed on 47, 52, 62 and 67 were used to acquire activity concentration on the background.

Table 4.9: COV% for 30 s of phantom measurements with high contrast

Sphere	COV% 30 s scan				
	normal	smooth	smooth A	smooth B	
Diameter	WB	WB	WB	WB	HN
37 mm	10.7 ± 0.2	9.6 ± 0.2	9.3 ± 0.2	9.1 ± 0.1	12.4 ± 0.2
28 mm	13.3 ± 0.2	11.9 ± 0.2	11.2 ± 0.2	10.8 ± 0.2	16.3 ± 0.3
22 mm	16.6 ± 0.3	14.3 ± 0.2	13.7 ± 0.2	13.10± 0.2	21.3 ± 0.4
17 mm	21.1 ± 0.3	17.9 ± 0.3	17.0 ± 0.3	15.9 ± 0.3	25.5 ± 0.4
13 mm	26.2 ± 0.4	22.4 ± 0.4	21.1 ± 0.3	19.5 ± 0.3	34.0 ± 0.4
10 mm	30.2 ± 0.5	28.0 ± 0.5	26.0 ± 0.4	23.8 ± 0.4	47.3 ± 0.8

Table 4.10: COV% for 60 s of phantom measurements with high contrast

Sphere	COV% 60 s scan				
	normal	smooth	smooth A	smooth B	
Diameter	WB	WB	WB	WB	HN
37 mm	11.7 ± 0.2	10.8 ± 0.2	10.5 ± 0.2	10.2 ± 0.2	9.4 ± 0.2
28 mm	12.8 ± 0.2	11.6 ± 0.2	11.2 ± 0.2	10.8 ± 0.2	11.7 ± 0.2
22 mm	15.2 ± 0.2	13.6 ± 0.2	13.0 ± 0.2	12.5 ± 0.2	14.7 ± 0.2
17 mm	18.7 ± 0.3	16.7 ± 0.3	15.8 ± 0.7	14.9 ± 0.2	18.8 ± 0.3
13 mm	23.0 ± 0.4	20.3 ± 0.3	18.7 ± 0.3	18.0 ± 0.3	24.6 ± 0.4
10 mm	27.2 ± 0.4	23.8 ± 0.4	22.3 ± 0.4	20.6 ± 0.3	32.8 ± 0.5

Table 4.11: COV% for 90 s of phantom measurements with high contrast

Sphere Diameter	COV% 90 s scan				
	normal	smooth	smooth A	smooth B	
	WB	WB	WB	WB	HN
37 mm	10.7 ± 0.2	9.9 ± 0.2	9.6 ± 0.2	9.2 ± 0.1	7.5 ± 0.1
28 mm	11.7 ± 0.2	10.5 ± 0.2	10.2 ± 0.2	9.8 ± 0.2	10.0 ± 0.2
22 mm	12.7 ± 0.2	11.6 ± 0.2	11.2 ± 0.2	10.7 ± 0.2	14.5 ± 0.2
17 mm	14.7 ± 0.2	13.1 ± 0.2	12.6 ± 0.2	10.4 ± 0.2	16.7 ± 0.3
1 3mm	16.5 ± 0.3	14.4 ± 0.2	13.7 ± 0.2	12.7 ± 0.2	20.7 ± 0.3
10 mm	19.3 ± 0.3	16.8 ± 0.3	15.9 ± 0.3	14.9 ± 0.2	25.9 ± 0.4

Table 4.12: COV% for 120 s of phantom measurements with high contrast

Sphere Diameter	COV% 120 s scan				
	normal	smooth	smooth A	smooth B	
	WB	WB	WB	WB	HN
37 mm	8.3 ± 0.1	7.6 ± 0.1	7.4 ± 0.1	7.2 ± 0.1	7.3 ± 0.1
2 8mm	10.2 ± 0.1	9.3 ± 0.1	9.0 ± 0.1	8.5 ± 0.1	9.5 ± 0.2
22 mm	12.5 ± 0.2	11.2 ± 0.2	10.6 ± 0.2	8.4 ± 0.1	12.7 ± 0.2
17 mm	14.2 ± 0.2	12.9 ± 0.2	12.4 ± 0.2	11.9 ± 0.2	15.9 ± 0.3
13mm	16.4 ± 0.3	14.7 ± 0.2	13.9 ± 0.2	13.2 ± 0.2	19.4 ± 0.3
10 mm	18.6 ± 0.3	16.1 ± 0.3	15.4 ± 0.3	14.8 ± 0.2	23.5 ± 0.4

Table 4.13: COV% for 150 s of phantom measurements with high contrast

Sphere Diameter	COV% 150 s scan				
	normal	smooth	smooth A	smooth B	
	WB	WB	WB	WB	HN
37 mm	7.6 ± 0.1	6.7 ± 0.1	6.5 ± 0.1	6.2 ± 0.1	6.3 ± 0.1
28 mm	9.0 ± 0.1	8.0 ± 0.1	8.1 ± 0.1	7.6 ± 0.1	8.9 ± 0.1
22 mm	10.6 ± 0.2	9.5 ± 0.2	9.8 ± 0.2	9.2 ± 0.1	11.4 ± 0.2
17 mm	12.6 ± 0.2	11.2 ± 0.2	11.3 ± 0.2	10.6 ± 0.2	14.9 ± 0.2
13 mm	15.3 ± 0.2	13.5 ± 0.2	13.1 ± 0.2	12.4 ± 0.2	17.4 ± 0.3
10 mm	16.5 ± 0.3	14.5 ± 0.2	14.2 ± 0.2	13.1 ± 0.2	22.7 ± 0.4

Table 4.14: COV% for 180 s of phantom measurements with high contrast

Sphere Diameter	COV% 180 s scan				
	normal	smooth	smooth A	smooth B	
	WB	WB	WB	WB	HN
37 mm	7.1 ± 0.1	6.4 ± 0.1	6.2 ± 0.1	6.0 ± 0.1	5.8 ± 0.1
28 mm	8.5 ± 0.1	7.6 ± 0.1	7.2 ± 0.12	6.9 ± 0.1	7.6 ± 0.1
22 mm	9.7 ± 0.2	8.5 ± 0.1	8.1 ± 0.1	7.7 ± 0.1	10.4 ± 0.2
17 mm	11.4 ± 0.2	10.0 ± 0.2	9.5 ± 0.2	8.9 ± 0.1	14.0 ± 0.2
13 mm	13.7 ± 0.2	12.0 ± 0.2	11.3 ± 0.2	10.6 ± 0.2	13.9 ± 0.3
10 mm	15.8 ± 0.3	13.6 ± 0.2	12.8 ± 0.2	11.7 ± 0.2	17.2 ± 0.4

Table 4.15: COV% for 300 s of phantom measurements with high contrast

Sphere Diameter	COV% 300 s scan				
	normal	smooth	smooth A	smooth B	
	WB	WB	WB	WB	HN
37 mm	6.1 ± 0.1	5.6 ± 0.1	5.5 ± 0.1	5.3 ± 0.1	5.7 ± 0.1
28 mm	7.5 ± 0.1	6.9 ± 0.1	6.7 ± 0.1	6.5 ± 0.1	7.5 ± 0.1
22 mm	8.93 ± 0.15	8.16 ± 0.14	7.86 ± 0.13	7.45 ± 0.12	9.16 ± 0.17
17 mm	10.2 ± 0.2	9.4 ± 0.2	9.0 ± 0.1	8.6 ± 0.1	11.2 ± 0.2
13 mm	11.9 ± 0.2	10.8 ± 0.2	10.3 ± 0.2	9.9 ± 0.2	7.5 ± 0.1
10 mm	12.7 ± 0.2	11.5 ± 0.2	11.0 ± 0.2	10.4 ± 0.2	10.4 ± 0.2

The results for high contrast (Tables 4.9 to 4.15) indicate a similar trend to low contrast; image noise decreases with an increase in acquisition time. The appearance of a PET image is affected by the matrix size, the pixel size decreases; as the number of reconstructed events that contribute to the image, decreases, resulting in loss of counts adding image noise (IAEA, 2014). Figure 4.5 plots COV% against time per field of view; image noise is higher for images reconstructed using smaller voxel size of 2x2x2 mm^3 compared to those using larger voxel size of 4x4x4 mm^3.

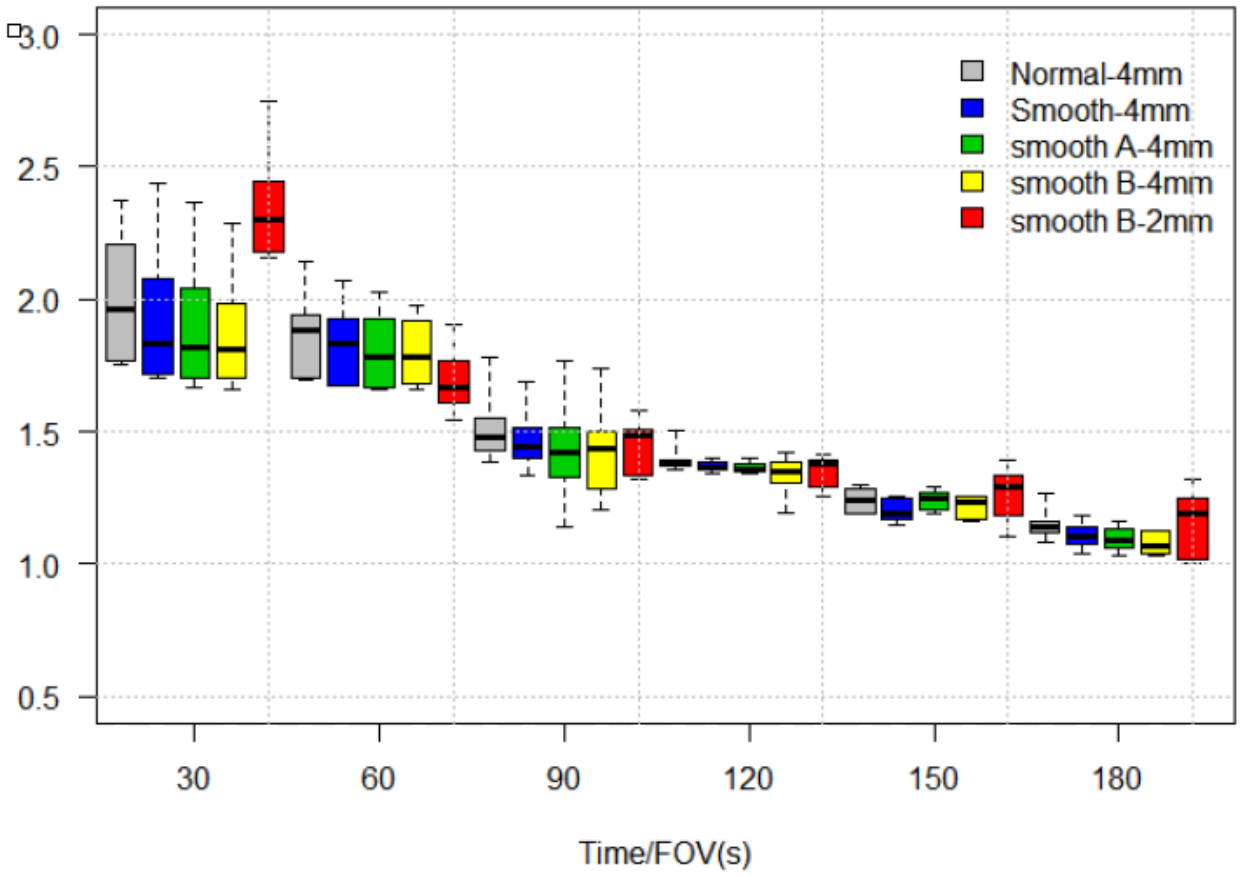

Figure 4.5: Bar plot of the COV % (high contrast) of all spheres for different frame duration times and smoothing filters in comparison to the 300 second reference scan for the WB reconstruction with voxel size of 4x4x4 mm^3 and 2x2x2 mm^3

The CNR data analyses results were obtained using equation 3.2 on images reconstructed with low contrast. The maximum activity concentration of the hot spheres were considered when determining the CNR. Tables 4.16 to 4.22 indicate CNR values for phantom measurements with low contrast. The contrast to noise ratio increased with an increase in acquisition time.

Table 4.16: CNR for 30 s of phantom measurement with low contrast

Sphere Diameter	CNR 30 s scan			
	normal	**smooth**	**smooth A**	**smooth B**
	WB	**WB**	**WB**	**WB**
37 mm	21.6 ± 0.4	27.5 ± 0.5	29.8 ± 0.5	32.7 ± 0.5
28 mm	10.9 ± 0.2	13.0 ± 0.2	14.5 ± 0.2	16.6 ± 0.3
22 mm	8.2 ± 0.1	10.1 ± 0.2	11.2 ± 0.2	12.4 ± 0.2
17 mm	6.5 ± 0.1	6.8 ± 0.1	8.0 ± 0.1	8.3 ± 0.1
13 mm	6.2 ± 0.1	7.2 ± 0.1	9.4 ± 0.2	9.4 ± 0.2
10 mm	2.3 ± 0.0	3.1 ± 0.0	3.4 ± 0.1	3.6 ± 0.1

Table 4.17: CNR for 60 s of phantom measurement with low contrast

Sphere Diameter	CNR 60 s scan			
	normal	**smooth**	**smooth A**	**smooth B**
	WB	**WB**	**WB**	**WB**
37 mm	37.5 ± 0.6	44.8 ± 0.7	49.4 ± 0.8	58.3 ± 1.0
28 mm	20.0 ± 0.3	24.2 ± 0.4	25.1 ± 0.4	28.7 ± 0.5
22 mm	14.5 ± 0.2	18.8 ± 0.3	21.6 ± 0.4	22.5 ± 0.4
17 mm	10.2 ± 0.2	12.1 ± 0.2	13.2 ± 0.2	14.3 ± 0.2
13 mm	9.1 ± 0.1	10.9 ± 0.2	11.9 ± 0.2	12.6 ± 0.2
10 mm	7.63 ± 0.13	7.68 ± 0.13	7.61 ± 0.13	7.46 ± 0.12

Table 4.18: CNR for 90 s of phantom measurement with low contrast

Sphere Diameter	CNR 90 s scan			
	normal	**smooth**	**smooth A**	**smooth B**
	WB	**WB**	**WB**	**WB**
37 mm	48.4 ± 0.81	57.0 ± 0.9	62.1 ± 1.0	68.4 ± 1.1
28 mm	22.6 ± 0.4	26.1 ± 0.4	28.6 ± 0.5	31.3 ± 0.5
22 mm	16.0 ± 0.3	18.5 ± 0.3	19.6 ± 0.3	22.1 ± 0.4
17 mm	10.5 ± 0.2	17.8 ± 0.3	12.9 ± 0.2	14.8 ± 0.2
13 mm	11.7 ± 0.2	12.6 ± 0.2	12.4 ± 0.2	13.5 ± 0.2
10 mm	6.9 ± 0.1	7.4 ± 0.1	7.6 ± 0.1	7.8 ± 0.1

Table 4.19: CNR for 120 s of phantom measurement with low contrast

Sphere Diameter	CNR 120 s scan			
	normal	**smooth**	**smooth A**	**smooth B**
	WB	**WB**	**WB**	**WB**
37 mm	52.6 ± 0.9	61.3 ± 1.0	65.0 ± 1.1	70.5 ± 1.2
28 mm	24.6 ± 0.4	30.1 ± 0.5	32.4 ± 0.5	35.4 ± 0.6
22 mm	19.2 ± 0.3	23.1 ± 0.4	24.0 ± 0.4	27.6 ± 0.5
17 mm	11.4 ± 0.2	13.7 ± 0.2	14.7 ± 0.2	15.8 ± 0.3
13 mm	7.9 ± 0.1	9.6 ± 0.2	10.4 ± 0.2	11.5 ± 0.2
10 mm	7.2 ± 0.1	7.9 ± 0.1	8.4 ± 0.1	7.8 ± 0.1

Table 4.20: CNR for 150 s of phantom measurement with low contrast

Sphere Diameter	CNR 150 s scan			
	normal	**smooth**	**smooth A**	**smooth B**
	WB	**WB**	**WB**	**WB**
37 mm	57.3 ± 1.0	63.3 ± 1.1	69.2 ± 1.1	73.7 ± 1.2
28 mm	32.0 ± 0.5	37.7 ± 0.6	39.6 ± 0.7	41.9 ± 0.7
22 mm	22.2 ± 0.4	27.1 ± 0.4	25.2 ± 0.4	26.8 ± 0.4
17 mm	14.6 ± 0.2	16.2 ± 0.3	18.2 ± 0.3	17.4 ± 0.3
13 mm	12.8 ± 0.21	14.5 ± 0.2	15.0 ± 0.2	15.6 ± 0.3
10 mm	10.1 ± 0.2	10.1 ± 0.2	10.2 ± 0.2	8.8 ± 0.1

Table 4.21: CNR for 180 s of phantom measurement with low contrast

Sphere Diameter	CNR 180 s scan			
	normal	**smooth**	**smooth A**	**smooth B**
	WB	**WB**	**WB**	**WB**
37 mm	66.1 ± 1.1	82.2 ± 1.4	89.1 ± 1.5	98.1 ± 1.6
28 mm	34.8 ± 0.6	41.8 ± 0.7	45.1 ± 0.7	48.7 ± 0.8
22 mm	25.9 ± 0.4	30.0 ± 0.5	31.9 ± 0.5	34.3 ± 0.6
17 mm	17.9 ± 0.3	20.4 ± 0.4	21.5 ± 0.4	23.0 ± 0.4
13 mm	13.2 ± 0.2	15.3 ± 0.3	16.3 ± 0.1	17.4 ± 0.3
10 mm	9.9 ± 0.2	10.9 ± 0.2	11.3 ± 0.2	10.6 ± 0.2

Table 4.22: CNR for 300 s of phantom measurement with low contrast

Sphere Diameter	CNR 300 s scan			
	normal	**smooth**	**smooth A**	**smooth B**
	WB	**WB**	**WB**	**WB**
37 mm	80.0 ± 1.3	75.6 ± 1.3	99.8 ± 1.7	83.0 ± 1.4
28 mm	34.8 ± 0.6	40.2 ± 0.7	45.6 ± 0.8	40.8 ± 0.7
22 mm	27.6 ± 0.5	31.4 ± 0.5	34.2 ± 0.6	36.1 ± 0.6
17 mm	18.4 ± 0.3	21.3 ± 0.3	22.6 ± 0.4	24.0 ± 0.4
13 mm	14.6 ± 0.2	15.6 ± 0.3	17.7 ± 0.3	17.7 ± 0.3
10 mm	10.3 ± 0.2	11.0 ± 0.2	12.2 ± 0.2	11.6 ± 1.0

The CNR was much higher for 37 mm spheres in comparison to the other spheres (10, 13, 17, 22 and 28 mm). Figure 4.6 illustrates the CNR plot against acquisition times per field of view at low contrast, when evaluating how the different reconstruction parameters influence PET image quality. Images filtered with smooth reconstruction parameter showed better CNR than the normal, smooth A and smooth B smoothing.

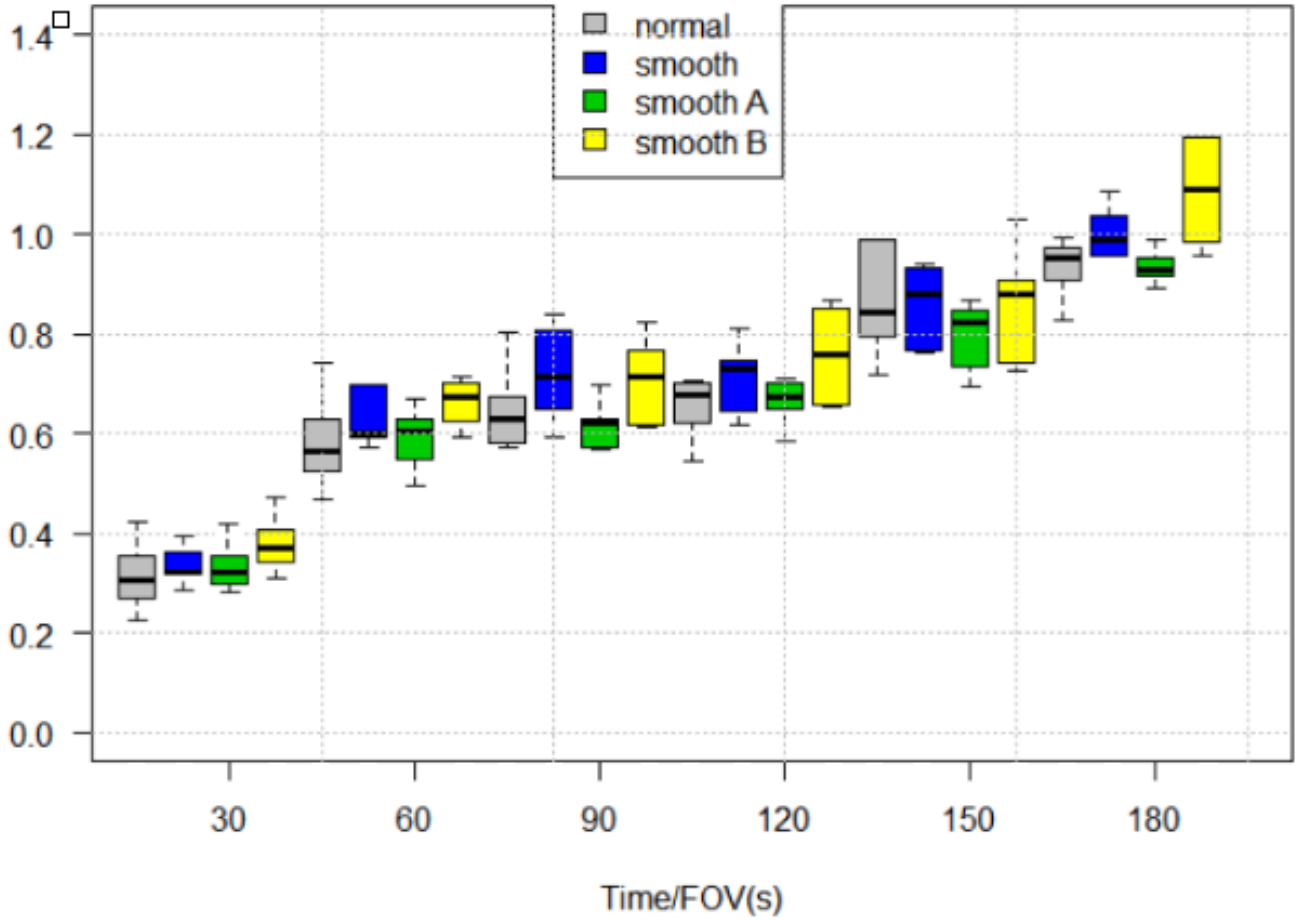

Figure 4.6: Bar plot of the CNR (low contrast) of all spheres for different frame duration times and smoothing filters in comparison to the 300 second reference scan for the whole body reconstruction with voxel size of 4x4x4 mm^3

The CNR data analyses results obtained using different reconstruction parameters on high contrast images are presented in tables 4.23 to 4.29. The CNR variability is higher in all spheres especially for the 28 mm and 37 mm spheres for all acquisition times.

Table 4.23: CNR for 30 s of phantom measurements with high contrast

Sphere	CNR 30 s scan				
	normal	smooth	smooth A	smooth B	
Diameter	WB	WB	WB	WB	HN
3 7mm	577.1 ± 9.6	642.1 ± 10.7	657.2 ± 10.9	670.5 ± 11.2	543.5 ± 9.1
28 mm	289.3 ± 4.8	318.9 ± 5.3	337.0 ± 5.6	348.9 ± 5.8	289.6 ± 4.8
22 mm	241.1 ± 4.0	274.9 ± 4.6	283.9 ± 3.4	297.1 ± 4.9	177.9 ± 3.0
17 mm	165.0 ± 2.7	193.1 ± 3.2	202.6 ± 1.9	216.1 ± 3.6	124.1 ± 2.1
13 mm	92.8 ± 1.5	106.1 ± 1.7	111.9 ± 1.9	120.2 ± 2.0	80.9 ± 1.3
10 mm	34.2 ± 0.6	42.9 ± 0.7	46.9 ± 0.8	52.1 ± 0.9	43.0 ± 0.7

Table 4.24: CNR for 60 s of phantom measurements with high contrast

Sphere	CNR 60 s scan				
	normal	smooth	smooth A	smooth B	
Diameter	WB	WB	WB	WB	HN
37 mm	517.8 ± 8.6	549.8 ± 9.2	561.3 ± 9.4	575.4 ± 9.6	671.8 ± 11.2
28 mm	283.0 ± 4.7	308.5 ± 5.1	318.4 ± 5.3	329.6 ± 5.5	357.4 ± 6.0
22 mm	257.9 ± 4.3	276.0 ± 4.6	286.7 ± 3.5	298.8 ± 5.0	267.2 ± 4.4
17 mm	181.3 ± 3.0	201.6 ± 3.4	212.5 ± 3.5	224.8 ± 3.7	185.1 ± 3.1
13 mm	96.9 ± 1.62	109.5 ± 1.8	117.2 ± 1.9	122.1 ± 2.0	142.5 ± 2.4
10 mm	58.6 ± 1.0	65.1 ± 1.1	68.6 ± 1.1	73.3 ± 1.2	91.1 ± 1.5

Table 4.25: CNR for 90 s of phantom measurements with high contrast

Sphere Diameter	CNR 90 s scan				
	normal	smooth	smooth A	smooth B	
	WB	WB	WB	WB	HN
37 mm	526.7 ± 8.8	569.5 ± 9.49	585.1 ± 9.7	608.2 ± 10.1	880.5 ± 14.7
28 mm	291.7 ± 4.9	323.6 ± 5.4	335.5 ± 5.6	350.9 ± 5.9	414.3 ± 6.9
22 mm	294.9 ± 4.9	325.3 ± 5.4	337.9 ± 4.3	353.3 ± 5.9	339.4 ± 5.7
17 mm	214.8 ± 3.6	244.3 ± 4.1	255.7 ± 4.3	311.5 ± 5.2	208.9 ± 3.5
13 mm	135.2 ± 2.2	157.6 ± 2.6	166.7 ± 2.8	180.8 ± 3.0	153.6 ± 2.6
10 mm	70.1 ± 1.1	82.5 ± 1.4	88.2 ± 1.5	94.5 ± 1.6	86.6 ± 1.4

Table 4.26: CNR for 120 s of phantom measurements with high contrast

Sphere Diameter	CNR 120 s scan				
	normal	smooth	smooth A	smooth B	
	WB	WB	WB	WB	HN
37 mm	675.4 ± 11.3	737.6 ± 12.3	759.9 ± 12.7	786.2 ± 13.1	942.3 ± 15.7
28 mm	346.6 ± 5.8	385.4 ± 6.4	398.5 ± 6.6	423.1 ± 7.0	381.7 ± 6.4
22 mm	311.7 ± 5.2	347.9 ± 5.8	367.0 ± 4.1	466.0 ± 7.8	259.0 ± 4.3
17 mm	213.0 ± 3.5	236.0 ± 3.9	247.0 ± 4.1	258.0 ± 4.3	181.0 ± 3.0
13 mm	137.0 ± 2.3	152.3 ± 2.5	159.8 ± 2.7	167.8 ± 2.8	134.4 ± 2.2
10 mm	69.1 ± 1.1	83.3 ± 1.4	88.3 ± 1.5	91.3 ± 1.5	90.3 ± 1.5

Table 4.27: CNR for 150 s of phantom measurements with high contrast

Sphere Diameter	CNR 150 s scan				
	normal	smooth	smooth A	smooth B	
	WB	WB	WB	WB	HN
37 mm	778.0 ± 13.0	884.5 ± 14.7	900.4 ± 15.0	946.9 ± 15.8	827.8 ± 13.8
28 mm	410.7 ± 6.8	455.6 ± 7.6	443.1 ± 7.4	467.6 ± 7.8	410.8 ± 6.8
22 mm	350.8 ± 5.8	394.5 ± 4.5	385.2 ± 4.4	412.5 ± 6.9	287.6 ± 4.8
17 mm	232.0 ± 3.9	268.7 ± 4.5	265.7 ± 4.4	286.4 ± 4.4	172.9 ± 2.9
13 mm	156.6 ± 2.6	159.3 ± 2.6	164.5 ± 2.7	175.3 ± 2.9	139.8 ± 2.3
10 mm	98.5 ± 1.6	108.2 ± 1.8	109.0 ± 1.8	115.7 ± 1.9	98.7 ± 1.6

Table 4.28: CNR for 180 s of phantom measurements with high contrast

Sphere Diameter	CNR 180 s scan				
	normal	smooth	smooth A	smooth B	
	WB	WB	WB	WB	HN
37 mm	801.8±13.4	879.3 ± 14.7	908.0 ± 15.1	942.1 ± 15.7	984.2 ± 16.4
28 mm	419.0 ± 7.0	467.5 ± 7.8	487.0 ± 8.1	512.1 ± 8.5	515.7 ± 8.6
22 mm	358.7 ± 6.0	415.8 ± 4.9	440.3 ± 5.1	471.8 ± 7.9	323.8 ± 5.4
17 mm	253.0 ± 4.2	292.0 ± 4.9	309.2 ± 5.1	332.0 ± 5.5	198.4 ± 3.3
13 mm	183.8 ± 3.1	180.7 ± 3.0	191.9 ± 3.2	206.9 ± 3.4	158.7 ± 2.6
10 mm	87.5 ± 1.5	102.9 ± 1.7	110.2 ± 1.8	120.0 ± 2.0	89.9 ± 1.5

Table 4.29: CNR for 300 s of phantom measurements with high contrast

Sphere Diameter	CNR 300 s scan				
	normal	smooth	smooth A	smooth B	
	WB	WB	WB	WB	HN
37 mm	938.9 ± 15.6	1015.1 ± 16.9	1041.5 ± 17.4	1068.9 ± 17.8	1006.9 ± 16.8
28 mm	469.5 ± 7.8	506.5 ± 8.4	522.7 ± 8.7	541.6 ± 9.0	512.8 ± 8.5
22 mm	394.7 ± 6.6	435.2 ± 7.2	454.6 ± 7.6	484.0 ± 8.1	378.7 ± 6.3
17 mm	303.8 ± 5.1	328.8 ± 5.5	341.6 ± 5.7	358.0 ± 6.0	264.3 ± 4.4
13 mm	183.8 ± 3.1	203.6 ± 3.4	213.2 ± 3.5	224.7 ± 3.7	201.1 ± 3.3
10 mm	102.9 ± 1.7	116.3 ± 1.9	122.1 ± 2.0	128.9 ± 2.1	112.9 ± 1.9

The contrast to noise ratio on high contrast images were higher than those with low contrast.

Figure 4.7 shows graphical representation of the contrast to noise analyses results for high contrast images reconstructed with several reconstruction parameters. Images reconstructed with higher voxel size mainly smooth B illustrated better CNR than those reconstructed with smaller voxel size.

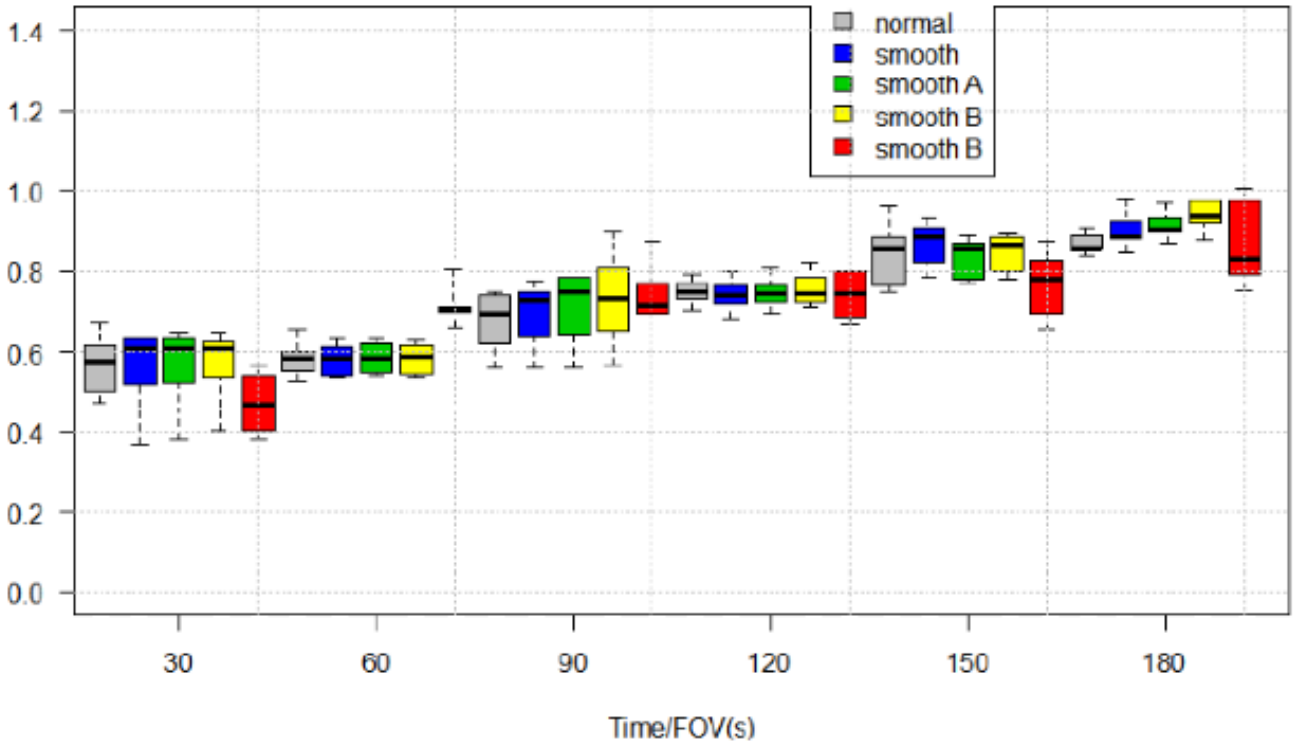

Figure 4.7: Bar plot of the CNR (high contrast) of all spheres for different frame duration times and smoothing filters in comparison to the 300 second reference scan for the whole body reconstruction with voxel size of 4x4x4 mm^3 and 2x2x2 mm^3

The SNR analyses results obtained using equation 3.1 on images reconstructed with low contrast are given in tables 4.30 to 4.36.

Table 4.30: SNR for 30 s of phantom measurement with low contrast

Sphere Diameter	SNR 30 s scan			
	normal	**smooth**	**smooth A**	**smooth B**
	WB	**WB**	**WB**	**WB**
37 mm	7.9 ± 0.1	7.9 ± 0.1	9.7 ± 0.2	10.1 ± 0.2
28 mm	7.8 ± 0.1	7.8 ± 0.1	9.5 ± 0.2	10.1 ± 0.2
22 mm	8.0 ± 0.1	8.0 ± 0.1	9.7 ± 0.2	10.4 ± 0.2
17 mm	8.0 ± 0.1	8.0 ± 0.1	9.5 ± 0.2	9.6 ± 0.2
13 mm	7.3 ± 0.1	7.3 ± 0.1	9.0 ± 0.1	9.2 ± 0.1
10 mm	6.4 ± 0.1	6.4 ± 0.1	7.5 ± 0.1	8.0 ± 0.1

Table 4.31: SNR for 60 s of phantom measurement with low contrast

Sphere Diameter	SNR 60 s scan			
	normal	**smooth**	**smooth A**	**smooth B**
	WB	**WB**	**WB**	**WB**
37 mm	12.1 ± 0.2	13.9 ± 0.2	15.0 ± 0.2	16.6 ± 0.3
28 mm	12.1 ± 0.2	13.8 ± 0.2	14.0 ± 0.2	15.9 ± 0.3
22 mm	11.0 ± 0.2	12.7 ± 0.2	14.0 ± 0.2	14.7 ± 0.2
17 mm	9.4 ± 0.2	10.6 ± 0.2	11.4 ± 0.2	12.5 ± 0.2
13 mm	8.2 ± 0.1	9.6 ± 0.2	10.5 ± 0.2	11.2 ± 0.2
10 mm	7.6 ± 0.1	8.8 ± 0.1	9.1 ± 0.1	9.6 ± 0.2

Table 4.32: SNR for 90 s of phantom measurement with low contrast

Sphere Diameter	SNR 90 s scan			
	normal	**smooth**	**smooth A**	**smooth B**
	WB	**WB**	**WB**	**WB**
37 mm	14.0 ± 0.2	15.8 ± 0.3	16.8 ± 0.3	18.3 ± 0.3
28 mm	12.1 ± 0.2	13.5 ± 0.2	14.3 ± 0.2	15.5 ± 0.3
22 mm	11.5 ± 0.2	12.9 ± 0.2	13.2 ± 0.2	14.5 ± 0.2
17 mm	10.6 ± 0.2	12.0 ± 0.2	12.4 ± 0.2	13.5 ± 0.2
13 mm	9.3 ± 0.1	10.3 ± 0.2	10.9 ± 0.2	11.7 ± 0.2
10 mm	8.2 ± 0.1	9.4 ± 0.2	10.0 ± 0.2	10.6 ± 0.2

Table 4.33: SNR for 120 s of phantom measurement with low contrast

Sphere Diameter	SNR 120 s scan			
	normal	**smooth**	**smooth A**	**smooth B**
	WB	**WB**	**WB**	**WB**
37 mm	15.5 ± 0.3	16.9 ± 0.3	17.6 ± 0.3	18.8 ± 0.3
28 mm	14.3 ± 0.2	16.6 ± 0.3	17.6 ± 0.3	18.7 ± 0.3
22 mm	13.5 ± 0.2	15.5 ± 0.3	15.9 ± 0.3	17.5 ± 0.3
17 mm	12.6 ± 0.2	15.3 ± 0.3	16.1 ± 0.3	17.1 ± 0.3
13 mm	10.6 ± 0.2	12.6 ± 0.2	13.2 ± 0.2	14.7 ± 0.2
10 mm	9.3 ± 0.2	10.7 ± 0.2	11.5 ± 0.2	12.7 ± 0.2

Table 4.34: SNR for 150 s of phantom measurement with low contrast

Sphere Diameter	SNR 150 s scan			
	normal	**smooth**	**smooth A**	**smooth B**
	WB	**WB**	**WB**	**WB**
37 mm	15.4 ± 0.3	17.1 ± 0.3	18.4 ± 0.3	19.1 ± 0.3
28 mm	16.3 ± 0.3	17.8 ± 0.3	18.5 ± 0.3	19.7 ± 0.3
22 mm	14.7 ± 0.2	15.9 ± 0.3	16.4 ± 0.3	17.1 ± 0.3
17 mm	14.6 ± 0.2	15.2 ± 0.3	15.8 ± 0.3	16.2 ± 0.3
13 mm	12.3 ± 0.2	13.3 ± 0.2	13.8 ± 0.3	14.6 ± 0.2
10 mm	11.7 ± 0.2	12.7 ± 0.2	13.2 ± 0.2	14.3 ± 0.2

Table 4.35: SNR for 180 s of phantom measurement with low contrast

Sphere Diameter	SNR 180 s scan			
	normal	**smooth**	**smooth A**	**smooth B**
	WB	**WB**	**WB**	**WB**
37 mm	18.1 ± 0.3	21.6 ± 0.4	23.1 ± 0.4	25.1 ± 0.4
28 mm	17.9 ± 0.3	20.8 ± 0.3	22.2 ± 0.4	23.7 ± 0.4
22 mm	17.1 ± 0.3	19.3 ± 0.3	20.3 ± 0.3	21.6 ± 0.4
17 mm	15.6 ± 0.3	17.2 ± 0.3	18.1 ± 0.3	19.3 ± 0.4
13 mm	13.7 ± 0.2	15.6 ± 0.3	16.7 ± 0.3	18.0 ± 0.3
10 mm	11.5 ± 0.2	13.2 ± 0.2	14.0 ± 0.2	15.1 ± 0.2

Table 4.36: SNR for 300 s of phantom measurement with low contrast

Sphere	**SNR 300 s scan**			
	normal	**smooth**	**smooth A**	**smooth B**
Diameter	**WB**	**WB**	**WB**	**WB**
37 mm	20.7 ± 0.3	18.8 ± 0.3	25.3 ± 0.4	20.4 ± 0.3
28 mm	17.6 ± 0.3	19.6 ± 0.3	21.1 ± 0.3	19.2 ± 0.3
22 mm	16.2 ± 0.3	18.0 ± 0.3	19.6 ± 0.3	20.4 ± 0.3
17 mm	15.3 ± 0.3	17.2 ± 0.3	18.4 ± 0.3	19.5 ± 0.3
13 mm	13.9 ± 0.2	15.7 ± 0.3	16.8 ± 0.3	17.5 ± 0.3
10 mm	14.3 ± 0.2	15.6 ± 0.3	16.9 ± 0.3	17.6 ± 0.3

The graph in figure 4.8 shows the SNR (low contrast) increases with longer acquisition times for all FOV. The images reconstructed with normal showed better SNR followed by smooth A, smooth smoothing indicated better fit between the second and third group quantile.

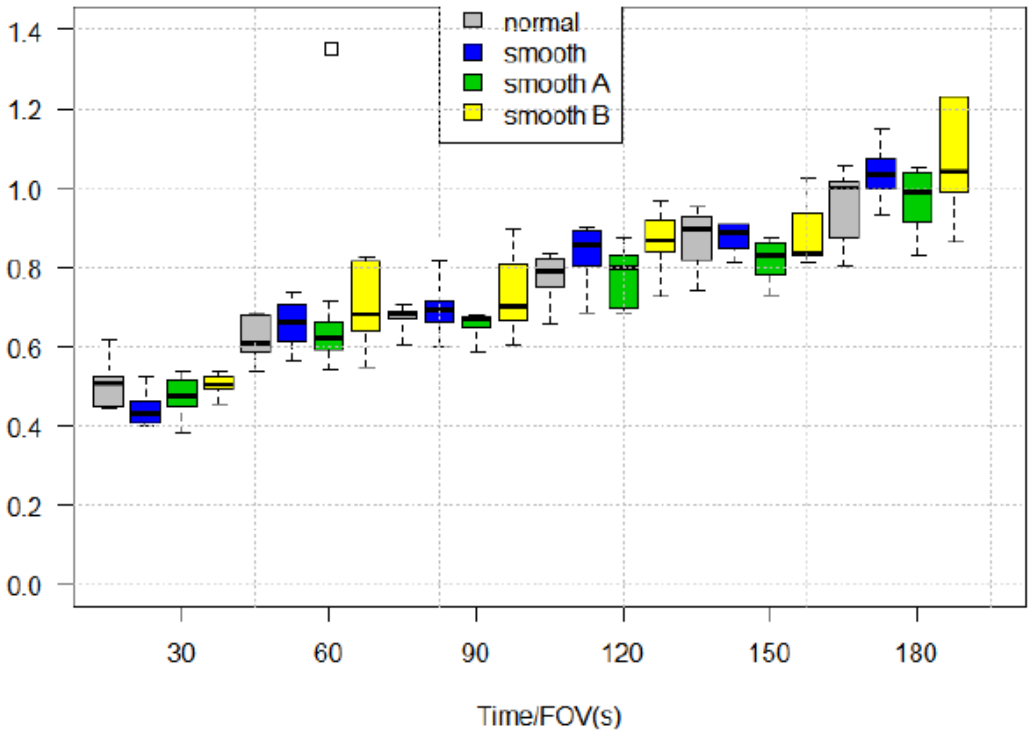

Figure 4.8: Bar plot of the SNR for different frame duration times and smoothing filters in comparison to the 300 second reference scan for the WB reconstruction with voxel size of 4x4x4 mm^3

The SNR data analysis for images reconstructed with large (4x4x4 mm^3) and small (2x2x2 mm^3) voxel sizes are shown in tables 4.37 to 4.43.

Table 4.37: SNR for 30 s phantom measurements with high contrast

Sphere	SNR 30 s scan				
	normal	smooth	smooth A	smooth B	
Diameter	WB	WB	WB	WB	HN
37 mm	9.4 ± 0.2	10.5 ± 0.2	10.7 ± 0.2	11.0 ± 0.2	8.1 ± 0.1
28 mm	7.5 ± 0.1	8.4 ± 0.1	8.9 ± 0.1	9.2 ± 0.1	6.1 ± 0.1
22 mm	6.0 ± 0.1	7.0 ± 0.1	7.3 ± 0.1	7.6 ± 0.1	4.7 ± 0.1
17 mm	4.7 ± 0.1	5.6 ± 0.1	5.9 ± 0.1	6.3 ± 0.1	3.9 ± 0.1
13 mm	3.8 ± 0.1	4.5 ± 0.1	4.7 ± 0.1	5.1 ± 0.1	2.9 ± 0.0
10 mm	3.3 ± 0.1	3.6 ± 0.1	3.8 ± 0.1	4.2 ± 0.1	2.1 ± 0.0

Table 4.38: SNR for 60 s of phantom measurements with high contrast

Sphere	SNR 60 s scan				
	normal	smooth	smooth A	smooth B	
Diameter	WB	WB	WB	WB	HN
37 mm	8.6 ± 0.1	9.2 ± 0.1	9.5 ± 0.2	9.8 ± 0.2	10.6 ± 0.2
28 mm	7.8 ± 0.1	8.6 ± 0.1	8.9 ± 0.1	9.2 ± 0.1	8.6 ± 0.1
22 mm	6.6 ± 0.1	7.3 ± 0.1	7.7 ± 0.1	8.0 ± 0.1	6.8 ± 0.1
17 mm	5.3 ± 0.1	5.6 ± 0.1	6.3 ± 0.1	6.7 ± 0.1	5.3 ± 0.1
13mm	4.34 ± 0.07	4.93 ± 0.08	5.34 ± 0.09	5.57 ± 0.09	4.06 ± 0.07
10mm	3.68 ± 0.06	4.20 ± 0.07	4.49 ± 0.09	4.86 ± 0.08	3.05 ± 0.05

Table 4.39: SNR for 90 s of phantom measurements with high contrast

Sphere Diameter	SNR 90 s scan				
	normal	smooth	smooth A	smooth B	
	WB	WB	WB	WB	HN
37 mm	9.3 ± 0.2	10.1 ± 0.2	10.4 ± 0.2	10.8 ± 0.2	13.4 ± 0.2
28 mm	8.5 ± 0.1	9.5 ± 0.2	9.8 ± 0.2	10.2 ± 0.2	10.0 ± 0.2
22 mm	7.8 ± 0.1	8.6 ± 0.1	9.0 ± 0.1	9.3 ± 0.2	6.9 ± 0.1
17 mm	6.8 ± 0.1	7.6 ± 0.1	7.9 ± 0.1	9.6 ± 0.2	6.0 ± 0.1
13 mm	6.1 ± 0.1	6.9 ± 0.1	7.3 ± 0.1	7.9 ± 0.1	4.8 ± 0.1
10 mm	5.2 ± 0.1	5.9 ± 0.1	6.3 ± 0.1	6.7 ± 0.1	3.9 ± 0.1

Table 4.40: SNR for 120 s of phantom measurements with high contrast

Sphere Diameter	SNR 120 s scan				
	normal	smooth	smooth A	smooth B	
	WB	WB	WB	WB	HN
37 mm	12.0 ± 0.2	13.1 ± 0.2	13.5 ± 0.2	13.9 ± 0.2	13.7 ± 0.2
28 mm	9.8 ± 0.2	10.8 ± 0.2	11.1 ± 0.2	11.7 ± 0.2	10.6 ± 0.2
22 mm	8.0 ± 0.1	8.9 ± 0.1	9.4 ± 0.2	11.9 ± 0.2	7.9 ± 0.1
17 mm	7.0 ± 0.1	7.7 ± 0.1	8.1 ± 0.1	8.4 ± 0.1	6.3 ± 0.1
13 mm	6.1 ± 0.1	6.8 ± 0.1	7.2 ± 0.1	7.5 ± 0.1	5.2 ± 0.1
10 mm	5.4 ± 0.1	6.2 ± 0.1	6.5 ± 0.1	6.7 ± 0.1	4.3 ± 0.1

Table 4.41: SNR for 150 s of phantom measurements with high contrast

Sphere Diameter	SNR 150 s scan				
	normal	smooth	smooth A	smooth B	
	WB	WB	WB	WB	HN
37 mm	13.2 ± 0.2	15.0 ± 0.2	15.3 ± 0.3	16.1 ± 0.3	16.0 ± 0.3
28 mm	11.2 ± 0.2	12.5 ± 0.2	12.4 ± 0.2	13.1 ± 0.2	11.2 ± 0.2
22 mm	9.4 ± 0.2	10.5 ± 0.2	10.2 ± 0.2	10.9 ± 0.2	8.7 ± 0.1
17 mm	8.0 ± 0.1	9.0 ± 0.1	8.8 ± 0.1	9.4 ± 0.2	7.0 ± 0.1
13 mm	6.5 ± 0.1	7.4 ± 0.1	7.6 ± 0.1	8.1 ± 0.1	5.2 ± 0.1
10 mm	6.1 ± 0.1	6.9 ± 0.1	7.0 ± 0.1	7.6 ± 0.1	4.4 ± 0.1

Table 4.42: SNR for 180 s of phantom measurements with high contrast

Sphere Diameter	SNR 180 s scan				
	normal	smooth	smooth A	smooth B	
	WB	WB	WB	WB	HN
37 mm	14.2 ± 0.2	15.6 ± 0.3	16.1 ± 0.3	16.7 ± 0.3	17.3 ± 0.3
28 mm	11.7 ± 0.2	13.2 ± 0.2	13.8 ± 0.2	14.5 ± 0.2	13.2 ± 0.2
22 mm	10.3 ± 0.2	11.8 ± 0.2	12.4 ± 0.2	13.1 ± 0.2	9.6 ± 0.2
17 mm	8.7 ± 0.1	10.0 ± 0.2	10.5 ± 0.2	11.2 ± 0.2	7.1 ± 0.1
13 mm	7.3 ± 0.1	8.3 ± 0.1	8.8 ± 0.1	9.5 ± 0.2	5.7 ± 0.1
10 mm	6.3 ± 0.1	7.3 ± 0.1	7.8 ± 0.1	8.5 ± 0.1	4.4 ± 0.1

Table 4.43: SNR for 300 s of phantom measurements with high contrast

Sphere Diameter	SNR 300 s scan				
	normal	smooth	smooth A	smooth B	
	WB	WB	WB	WB	HN
37 mm	16.5 ± 0.3	17.8 ± 0.3	18.3 ± 0.3	18.7 ± 0.3	17.6 ± 0.3
28 mm	13.3 ± 0.2	14.4 ± 0.2	14.9 ± 0.2	15.3 ± 0.3	13.2 ± 0.2
22 mm	11.2 ± 0.2	12.3 ± 0.2	12.7 ± 0.2	13.4 ± 0.2	10.9 ± 0.2
17 mm	9.8 ± 0.2	10.7 ± 0.2	11.1 ± 0.2	11.6 ± 0.2	8.9 ± 0.1
13 mm	8.4 ± 0.1	9.2 ± 0.1	9.7 ± 0.2	10.2 ± 0.2	7.2 ± 0.1
10mm	7.9 ± 0.1	8.7 ± 0.1	9.1 ± 0.1	9.6 ± 0.2	5.8 ± 0.1

Figure 4.9 shows the relation between images reconstructed with large (4x4x4 mm^3) and small (2x2x2 mm^3) voxels for high contrast, SNR vs time/FOV. There is a large difference in the mean values among the images reconstructed with different voxel sizes. The SNR increases as time increases, and images reconstructed using smooth B with small voxel size indicate better SNR than other reconstruction parameters.

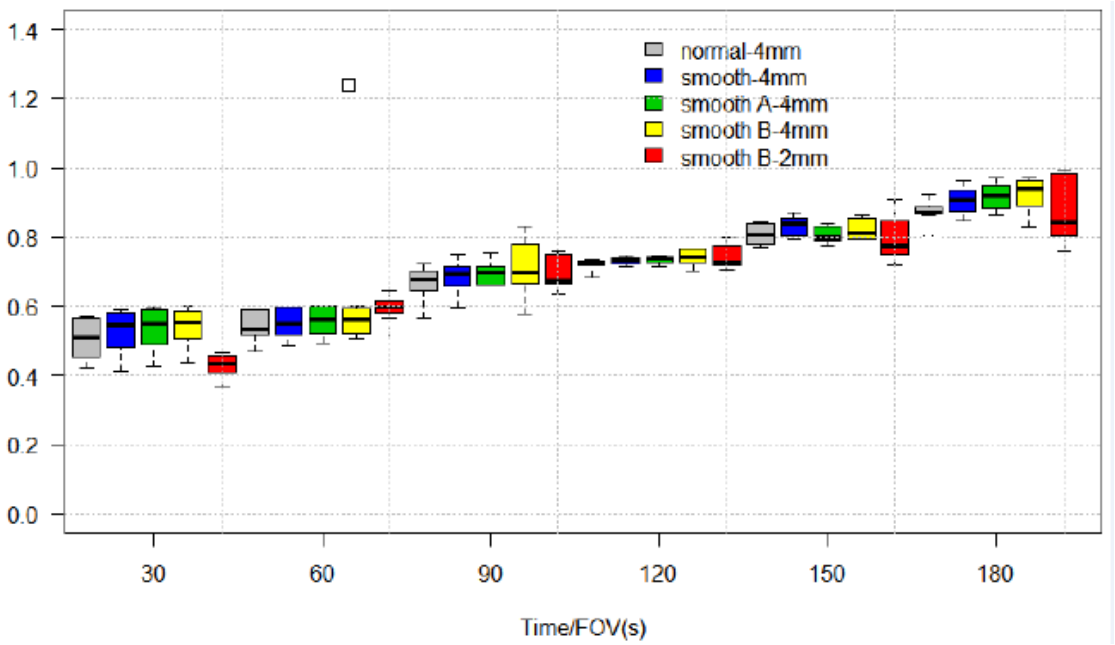

Figure 4.9: Bar plot of the SNR (high contrast) of all spheres for different frame duration times and smoothing filters in comparison to the 300 second reference scan for the WB reconstruction with voxel size of 4x4x4 mm^3 and 2x2x2 mm^3

Tables 4.44 to 4.50 show RC% data analysis for low contrast images obtained using equation 3.3, the images are for low contrast activity ratio.

Table 4.44: RC% for 30 s of phantom measurement with low contrast

Sphere Diameter	RC% 30 s scan			
	normal	**smooth**	**smooth A**	**smooth B**
	WB	**WB**	**WB**	**WB**
37 mm	75.6 ± 1.3	77.0 ± 1.3	76.4 ± 1.3	77.1 ± 1.3
28 mm	46.4 ± 0.8	45.1 ± 0.7	45.7 ± 0.8	45.9 ± 0.8
22 mm	38.1 ± 0.6	38.1 ± 0.6	37.9 ± 0.6	37.8 ± 0.6
17 mm	32.4 ± 0.5	31.4 ± 0.5	31.2 ± 0.5	31.0 ± 0.5
13 mm	31.1 ± 0.5	33.4 ± 0.6	33.4 ± 0.5	32.3 ± 0.5
10 mm	22.3 ± 0.4	23.0 ± 0.4	22.8 ± 0.4	22.4 ± 0.4

Table 4.45: RC% for 60 s of phantom measurement with low contrast

Sphere Diameter	RC% 60 s scan			
	normal	**smooth**	**smooth A**	**smooth B**
	WB	**WB**	**WB**	**WB**
37 mm	74.0 ± 1.2	73.2 ± 1.2	73.2 ± 1.2	75.1 ± 1.2
28 mm	46.4 ± 0.8	46.2 ± 0.8	46.7 ± 0.8	45.6 ± 0.8
22 mm	39.1 ± 0.6	40.6 ± 0.7	41.1 ± 0.7	40.0 ± 0.7
17 mm	33.4 ± 0.6	33.4 ± 0.6	33.7 ± 0.5	32.7 ± 0.5
13 mm	32.0 ± 0.5	32.1 ± 0.5	31.9 ± 0.5	31.5 ± 0.5
10 mm	28.9 ± 0.5	26.9 ± 0.4	26.3 ± 0.4	25.3 ± 0.4

Table 4.46: RC% for 90 s of phantom measurement with low contrast

Sphere Diameter	RC% 90 s scan			
	normal	**smooth**	**smooth A**	**smooth B**
	WB	**WB**	**WB**	**WB**
37 mm	74.8 ± 1.2	74.8 ± 1.3	75.2 ± 1.2	75.0 ± 1.2
28 mm	46.5 ± 0.8	46.5 ± 0.8	46.9 ± 0.8	46.7 ± 0.8
22 mm	38.1 ± 0.6	38.1 ± 0.6	38.4 ± 0.6	38.4 ± 0.6
17 mm	38.1 ± 0.6	38.1 ± 0.6	30.9 ± 0.5	31.3 ± 0.5
13 mm	33.2 ± 0.5	33.1 ± 0.5	31.6 ± 0.5	31.6 ± 0.5
10 mm	26.1 ± 0.4	26.1 ± 0.4	25.6 ± 0.4	24.9 ± 0.4

Table 4.47: RC% for 120 s of phantom measurement with low contrast

Sphere Diameter	RC% 120 s scan			
	normal	**smooth**	**smooth A**	**smooth B**
	WB	**WB**	**WB**	**WB**
37 mm	76.0 ± 1.3	77.1 ± 1.3	76.9 ± 1.3	76.7 ± 1.3
28 mm	45.9 ± 0.8	45.7 ± 0.8	45.7 ± 0.8	45.7 ± 0.8
22 mm	39.7 ± 0.7	39.4 ± 0.7	39.4 ± 0.7	39.7 ± 0.7
17 mm	30.2 ± 0.5	29.2 ± 0.	29.1 ± 0.5	29.0 ± 0.5
13 mm	26.8 ± 0.4	26.3 ± 0.4	26.4 ± 0.4	26.3 ± 0.4
10 mm	26.3 ± 0.4	25.3 ± 0.4	24.8 ± 0.4	24.2 ± 0.4

Table 4.48: RC% for 150 s of phantom measurement with low contrast

Sphere Diameter	RC% 150 s scan			
	normal	**smooth**	**smooth A**	**smooth B**
	WB	**WB**	**WB**	**WB**
37 mm	77.3 ± 1.3	75.1 ± 1.2	74.9 ± 1.2	75.9 ± 1.2
28 mm	47.2 ± 0.8	48.5 ± 0.8	48.4 ± 0.8	47.5 ± 0.8
22 mm	39.3 ± 0.6	38.4 ± 0.6	38.3 ± 0.6	38.5 ± 0.6
17 mm	30.9 ± 0.5	31.0 ± 0.5	32.0 ± 0.5	30.5 ± 0.5
13 mm	30.5 ± 0.5	30.3 ± 0.5	30.3 ± 0.5	29.8 ± 0.5
10 mm	26.9 ± 0.4	25.6 ± 0.4	25.1 ± 0.4	24.4 ± 0.4

Table 4.49: RC% for 180 s of phantom measurement with low contrast

Sphere Diameter	RC% 180 s scan			
	normal	**smooth**	**smooth A**	**smooth B**
	WB	**WB**	**WB**	**WB**
37 mm	76.0 ± 1.3	76.0 ± 1.3	76.0 ± 1.3	75.9 ± 1.3
28 mm	46.6 ± 0.8	46.5 ± 0.8	46.4 ± 0.8	46.2 ± 0.8
22 mm	39.0 ± 0.6	38.7 ± 0.6	38.6 ± 0.6	38.5 ± 0.6
17 mm	32.6 ± 0.5	32.4 ± 0.5	32.2 ± 0.5	32.0 ± 0.5
13 mm	29.0 ± 0.5	28.8 ± 0.5	28.6 ± 0.5	28.2 ± 0.5
10 mm	26.8 ± 0.4	26.0 ± 0.4	25.5 ± 0.4	24.8 ± 0.4

Table 4.50: RC% for 300 s of phantom measurement with low contrast

Sphere Diameter	RC% 300 s scan			
	normal	**smooth**	**smooth A**	**smooth B**
	WB	**WB**	**WB**	**WB**
37 mm	75.8 ± 1.3	75.9 ± 1.3	74.8 ± 1.2	75.1 ± 1.2
28 mm	45.6 ± 0.8	45.4 ± 0.8	45.0 ± 0.8	47.0 ± 0.8
22 mm	40.2 ± 0.7	40.3 ± 0.7	40.4 ± 0.7	40.2 ± 0.7
17 mm	32.6 ± 0.5	32.4 ± 0.5	32.3 ± 0.5	32.1 ± 0.5
13 mm	29.6 ± 0.5	28.3 ± 0.5	29.2 ± 0.5	28.4 ± 0.5
10 mm	24.4 ± 0.4	23.8 ± 0.4	24.1 ± 0.4	23.1 ± 0.4

Figure 4.10 presents the RC% of the spheres at different acquisition times per field of view on images reconstructed with lesion to background ratio of 5:1. The RC% is higher for region of interest that are larger as seen on tables 4.44 to 4.50. The results presented in these tables indicate significant differences at 180 seconds for all reconstruction parameters.

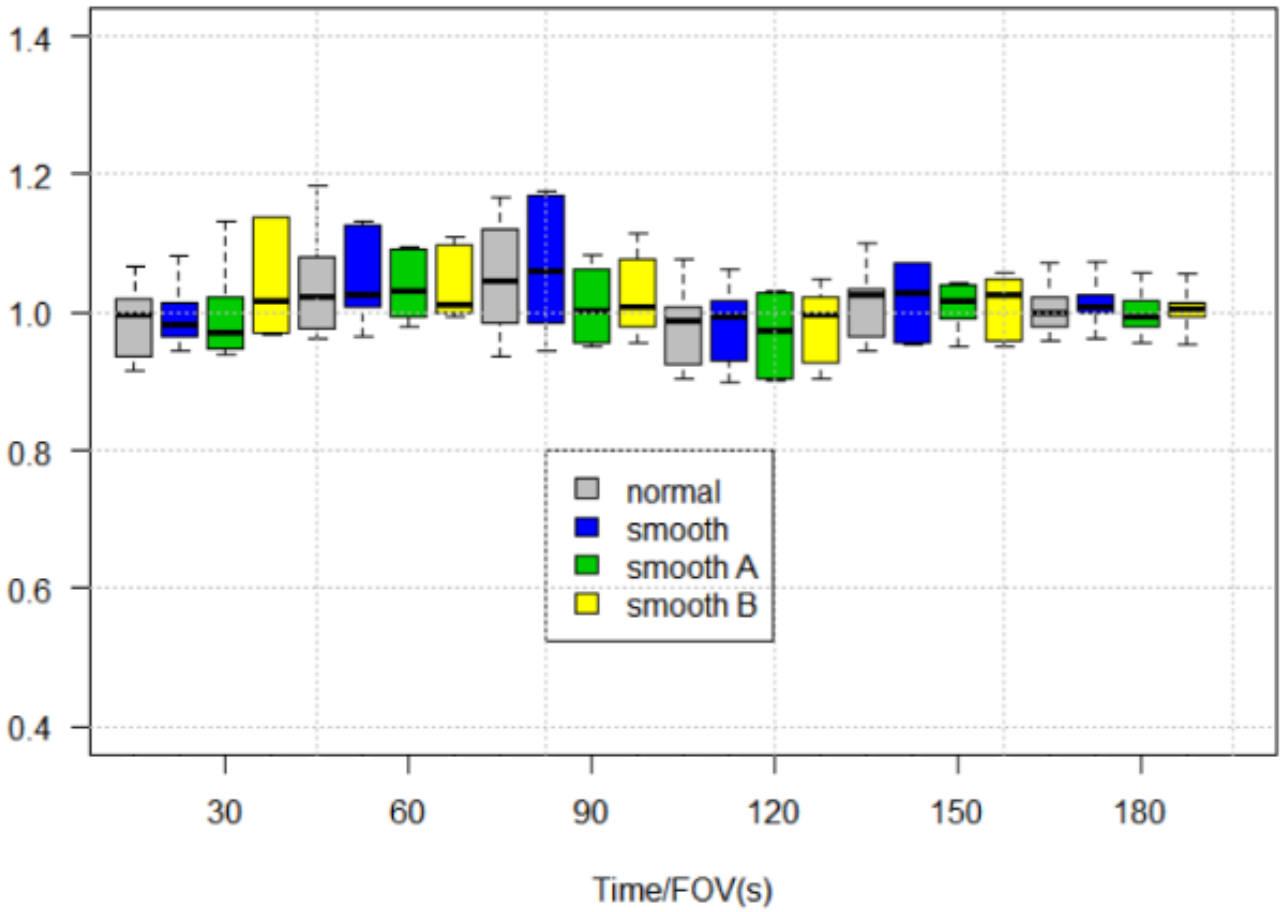

Figure 4.10: Bar plot of the RC% (low contrast) of all spheres for different frame duration times and smoothing filters in comparison to the 300 second reference scan for the WB reconstruction with a voxel size of 4x4x4 mm^3 (low contrast)

As for high contrast, tables 4.51 to 4.57 show the RC% for images reconstructed in large and small voxel sizes. The recovery coefficient for the spheres are slightly higher for high contrast compared to those of low contrast.

Table 4.51: RC% for 30 s of phantom measurements with high contrast

Sphere Diameter	RC% 30 s scan				
	normal	smooth	smooth A	smooth B	
	WB	WB	WB	WB	HN
37 mm	112.5 ± 1.9	112.5 ± 1.9	112.2 ± 1.9	111.6 ± 1.9	125.9 ± 2.1
28 mm	71.6 ± 1.2	70.9 ± 1.2	70.7 ± 1.2	70.6 ± 1.2	90.7 ± 1.5
22 mm	73.1 ± 1.2	72.1 ± 1.2	71.9 ± 1.2	71.9 ± 1.2	73.3 ± 1.2
17 mm	62.9 ± 1.1	63.0 ± 1.0	63.1 ± 1.0	63.3 ± 1.1	60.4 ± 1.0
13 mm	43.3 ± 0.7	43.3 ± 0.7	43.3 ± 0.7	43.2 ± 0.7	52.6 ± 0.9
10 mm	20.4 ± 0.3	22.3 ± 0.4	22.8 ± 0.4	23.3 ± 0.9	39.2 ± 0.6

Table 4.52: RC% for 60 s of phantom measurements with high contrast

Sphere Diameter	RC% 60 s scan				
	normal	smooth	smooth A	smooth B	
	WB	WB	WB	WB	HN
37 mm	112.7 ± 1.9	110.8 ± 1.8	110.2 ± 1.8	109.6 ± 1.8	117.0 ± 1.9
28 mm	70.0 ± 1.2	69.1 ± 1.1	69.0 ± 1.1	68.8 ± 1.1	78.1 ± 1.3
22 mm	77.2 ± 1.3	74.0 ± 1.2	73.5 ± 1.2	73.4 ± 1.2	73.3 ± 1.2
17 mm	67.8 ± 1.1	66.9 ± 1.1	66.7 ± 1.1	66.4 ± 1.1	63.2 ± 1.0
13 mm	46.4 ± 0.8	45.9 ± 0.8	45.5 ± 0.8	44.9 ± 0.7	62.7 ± 1.0
10 mm	33.8 ± 0.6	32.7 ± 0.5	32.2 ± 0.5	31.6 ± 0.5	53.2 ± 1.0

Table 4.53: RC% for 90 s of phantom measurements with high contrast

Sphere Diameter	RC% 90 s scan				
	normal	smooth	smooth A	smooth B	
	WB	WB	WB	WB	HN
37 mm	106.1 ± 1.8	105.8 ± 1.8	105.8 ± 1.8	105.9 ± 1.8	123.5 ± 2.1
28 mm	66.8 ± 1.1	66.6 ± 1.1	66.6 ± 1.1	66.8 ± 1.1	70.9 ± 1.2
22 mm	73.6 ± 1.2	73.6 ± 1.2	73.8 ± 1.2	74.1 ± 1.2	74.3 ± 1.2
17 mm	60.3 ± 1.0	61.2 ± 1.0	61.4 ± 1.0	61.7 ± 1.0	59.1 ± 1.0
13 mm	4.4 ± 0.7	44.1 ± 0.7	44.3 ± 0.7	44.3 ± 0.7	55.8 ± 0.9
10 mm	27.1 ± 0.4	27.7 ± 0.5	27.9 ± 0.5	28.0 ± 0.5	42.5 ± 0.7

Table 4.54: RC% for 120 s of phantom measurements with high contrast

Sphere Diameter	RC% 120 s scan				
	normal	smooth	smooth A	smooth B	
	WB	WB	WB	WB	HN
37 mm	104.2 ± 1.7	104.4 ± 1.7	104.5 ± 1.7	104.8 ± 1.7	110.4 ± 1.8
28 mm	67.6 ± 1.1	68.2 ± 1.1	68.4 ± 1.1	68.6 ± 1.1	73.0 ± 1.2
22 mm	73.9 ± 1.2	74.1 ± 1.2	74.3 ± 1.2	74.7 ± 1.2	72.2 ± 1.2
17 mm	60.0 ± 1.0	60.3 ± 1.0	60.4 ± 1.0	60.5 ± 1.0	58.5 ± 1.0
13 mm	45.4 ± 0.8	44.8 ± 0.7	44.6 ± 0.7	44.4 ± 0.7	53.9 ± 0.9
10 mm	26.8 ± 0.4	27.6 ± 0.5	27.8 ± 0.5	27.9 ± 0.5	41.3 ± 0.7

Table 4.55: RC% for 150 s phantom measurements with high contrast

Sphere Diameter	RC% 150 s scan				
	normal	smooth	smooth A	smooth B	
	WB	WB	WB	WB	HN
37 mm	108.5 ± 1.8	108.5 ± 1.8	108.5 ± 1.7	108.4 ± 1.8	113.7 ± 1.9
28 mm	69.3 ± 1.2	68.6 ± 1.1	68.3 ± 1.1	68.2 ± 1.1	74.7 ± 1.2
22 mm	70.7 ± 1.2	71.5 ± 1.2	72.0 ± 1.2	72.6 ± 1.2	70.9 ± 1.2
17 mm	56.1 ± 0.9	57.7 ± 1.0	58.3 ± 1.0	58.9 ± 1.0	53.8 ± 0.9
13 mm	41.1 ± 0.7	42.2 ± 0.7	42.4 ± 0.7	42.6 ± 0.7	52.7 ± 0.9
10 mm	32.3 ± 0.5	31.3 ± 0.5	30.9 ± 0.5	30.3 ± 0.5	44.1 ± 0.7

Table 4.56: RC% for 180 s phantom measurements with high contrast

Sphere Diameter	RC% 180 s scan				
	normal	smooth	smooth A	smooth B	
	WB	WB	WB	WB	HN
37 mm	104.7 ± 1.7	104.6 ± 1.7	104.8 ± 1.7	105.0 ± 1.7	107.8 ± 1.8
28 mm	68.3 ± 1.1	67.6 ± 1.1	67.6 ± 1.1	67.6 ± 1.1	75.0 ± 1.2
22 mm	66.6 ± 1.1	67.7 ± 1.1	68.3 ± 1.1	69.2 ± 1.1	65.0 ± 1.1
17 mm	56.9 ± 0.9	57.1 ± 0.9	57.3 ± 1.0	57.7 ± 1.0	54.3 ± 0.9
13 mm	42.5 ± 0.7	42.8 ± 0.7	42.9 ± 0.7	43.0 ± 0.7	53.9 ± 0.9
10 mm	28.0 ± 0.5	28.2 ± 0.5	28.3 ± 0.5	28.2 ± 0.5	40.4 ± 0.7

Table 4.57: RC% for 300 s phantom measurements with high contrast

Sphere Diameter	RC% 300 s scan				
	normal	smooth	smooth A	smooth B	
	WB	WB	WB	WB	HN
37 mm	106.1 ± 1.8	106.1 ± 1.8	106.1 ± 1.8	106.1 ± 1.8	108.2 ± 1.8
28 mm	67.8 ± 1.1	67.2 ± 1.1	67.3 ± 1.1	67.5 ± 1.1	74.2 ± 1.2
22 mm	68.1 ± 1.1	68.5 ± 1.1	68.9 ± 1.1	69.5 ± 1.2	66.9 ± 1.1
17 mm	60.2 ± 1.0	59.7 ± 1.0	59.6 ± 1.0	59.6 ± 1.0	57.8 ± 1.0
13 mm	43.4 ± 0.7	43.5 ± 0.7	43.6 ± 0.7	43.7 ± 0.7	54.6 ± 0.9
10 mm	26.7 ± 0.4	27.2 ± 0.4	27.3 ± 0.5	27.3 ± 0.5	38.4 ± 0.6

Figure 4.11 illustrates the RC% for high contrast reconstructed images. The RC% does not demonstrate significant change for all reconstruction parameters at 180 seconds.

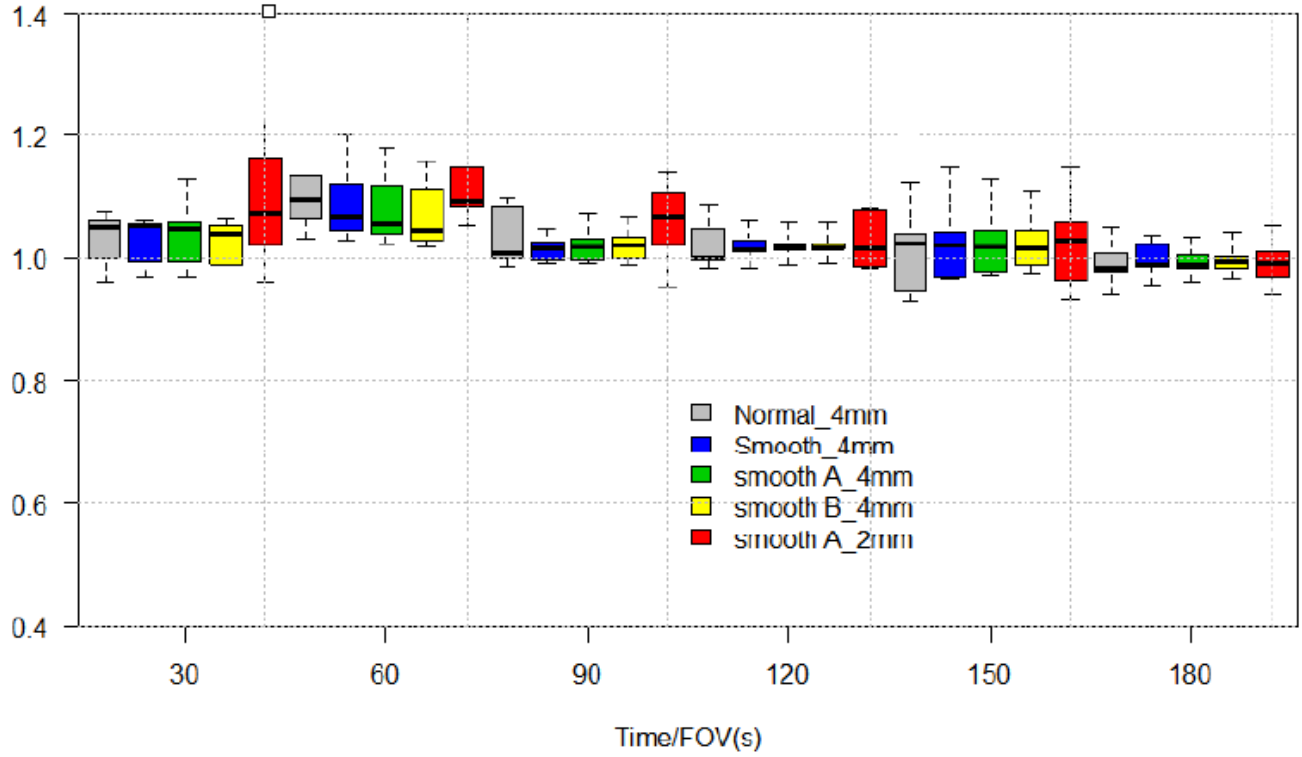

Figure 4.11: Bar plot of the RC% (high contrast) of all spheres for different frame duration times and smoothing filters in comparison to the 300 second reference scan for the whole body reconstruction with voxel size of 4x4x4 mm^3 and 2x2x2 mm^3

The relationship of the SUV measurements between the different acquisition times per bed position was determined using a linear regression method. The acquisition time per bed position of 300 seconds commonly used at the WCAPC was considered and compared.

As described in subchapter 1.6, the SUV_{max} is the highest value within a defined ROI, and it does not depend on the size of the ROI. Furthermore, it is least affected by partial volume effect (Adams et al., 2010). The SUV_{max} for images reconstructed with low contrast utilizing different reconstruction parameters are

presented in figures 4.12, 4.13, 4.14 and 4.15. The SUV_{max} for images reconstructed with high contrast also including different reconstruction parameters are presented in figures 4.16, 4.17, 4.18, 4.19 and 4.20.

In general, SUV_{max} illustrated a high correlation between the different acquisition times for both low and high contrast images and the routinely used acquisition time per bed position (300 s), applying different reconstruction parameters. In contrast to this the maximum activity concentration does not differ greatly among the different acquisition times and reconstruction parameters, which verifies the stability of the Gemini TF Big Bore Scanner.

4.2 Uniformity - Low Contrast

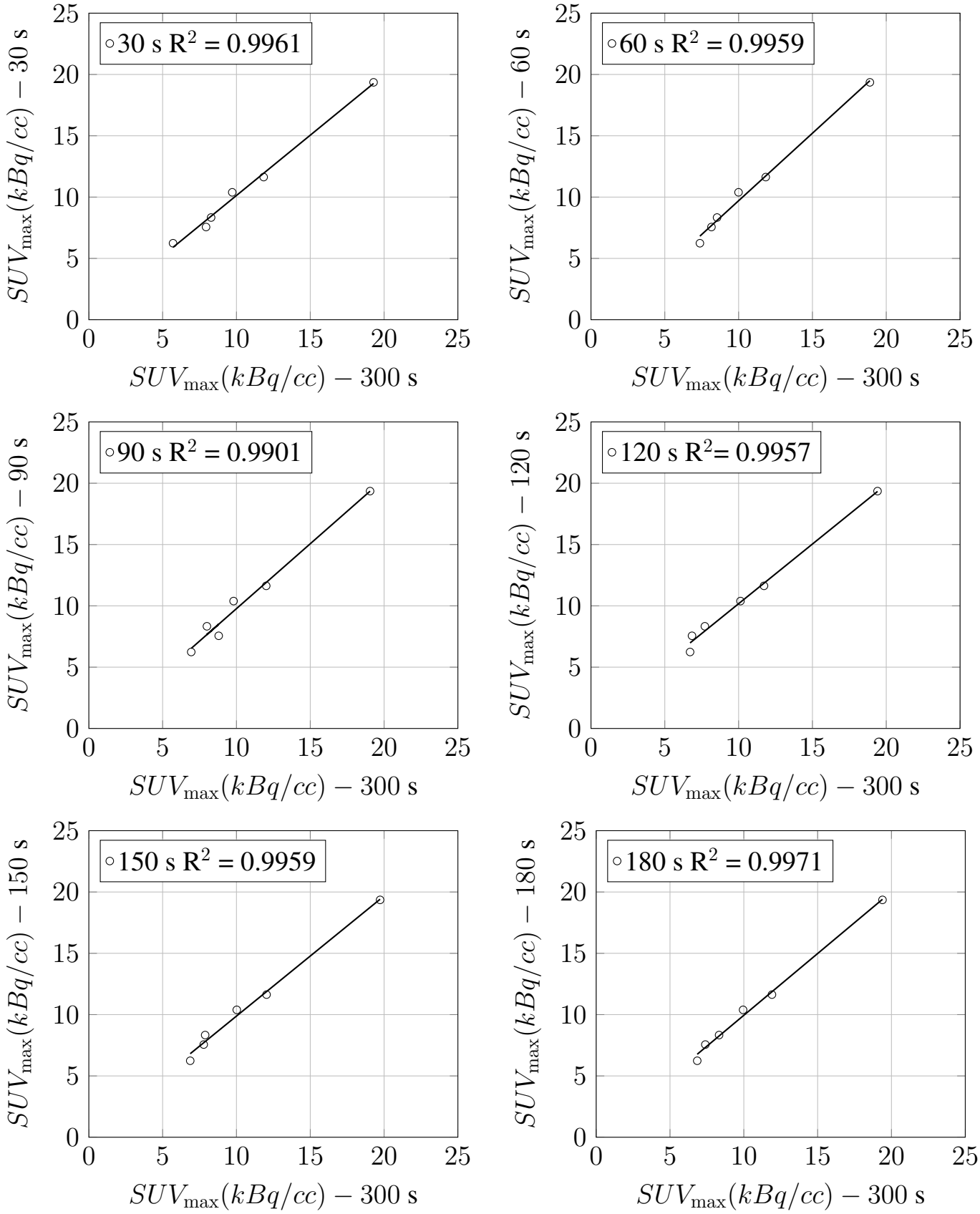

Figure 4.12: Maximum activity concentration of different acquisition times versus maximum activity concentration of 300 s acquisition time for focal points (normal - Low Contrast)

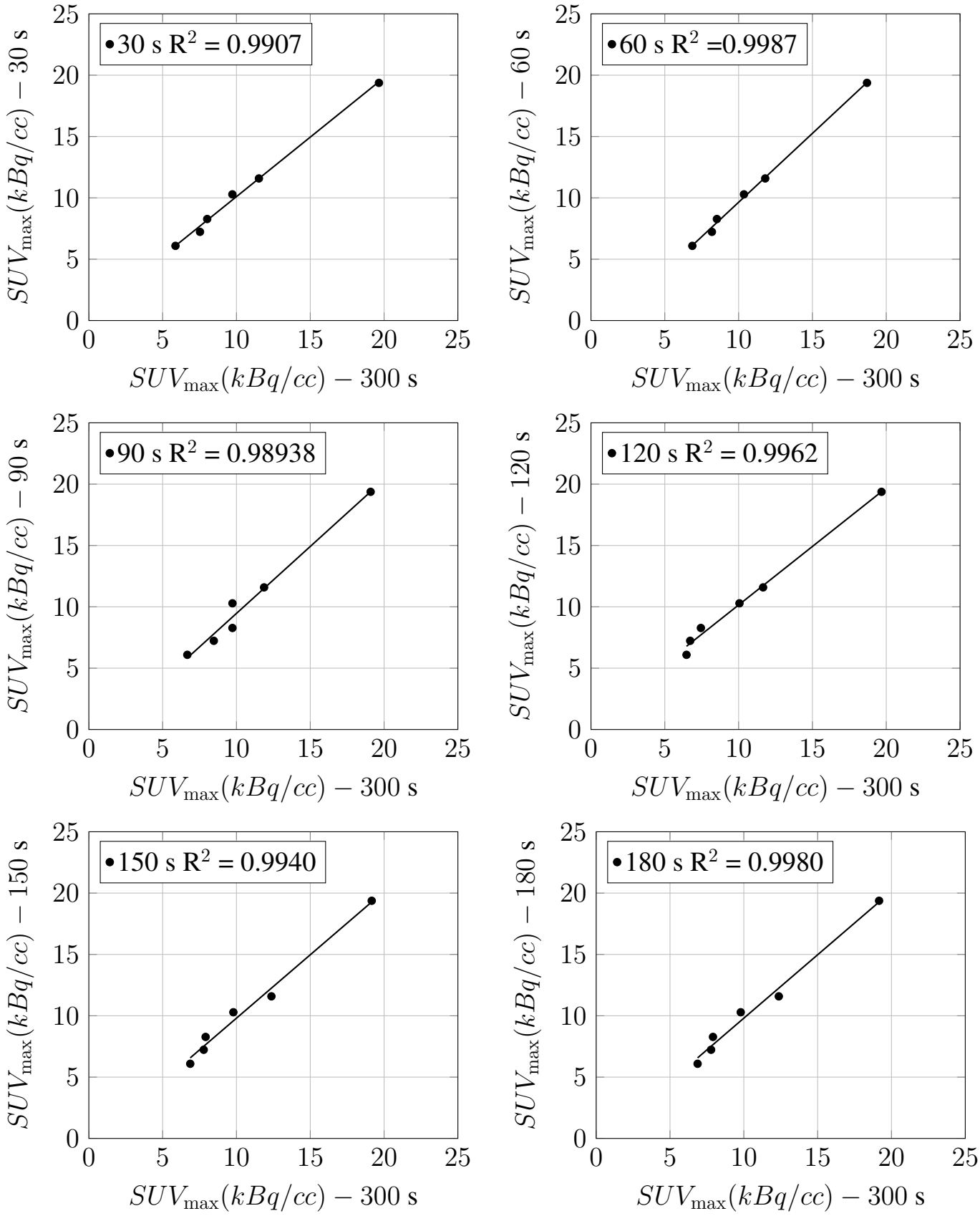

Figure 4.13: Maximum activity concentration of different acquisition times versus maximum activity concentration of 300 s acquisition time for focal points (smooth - Low Contrast)

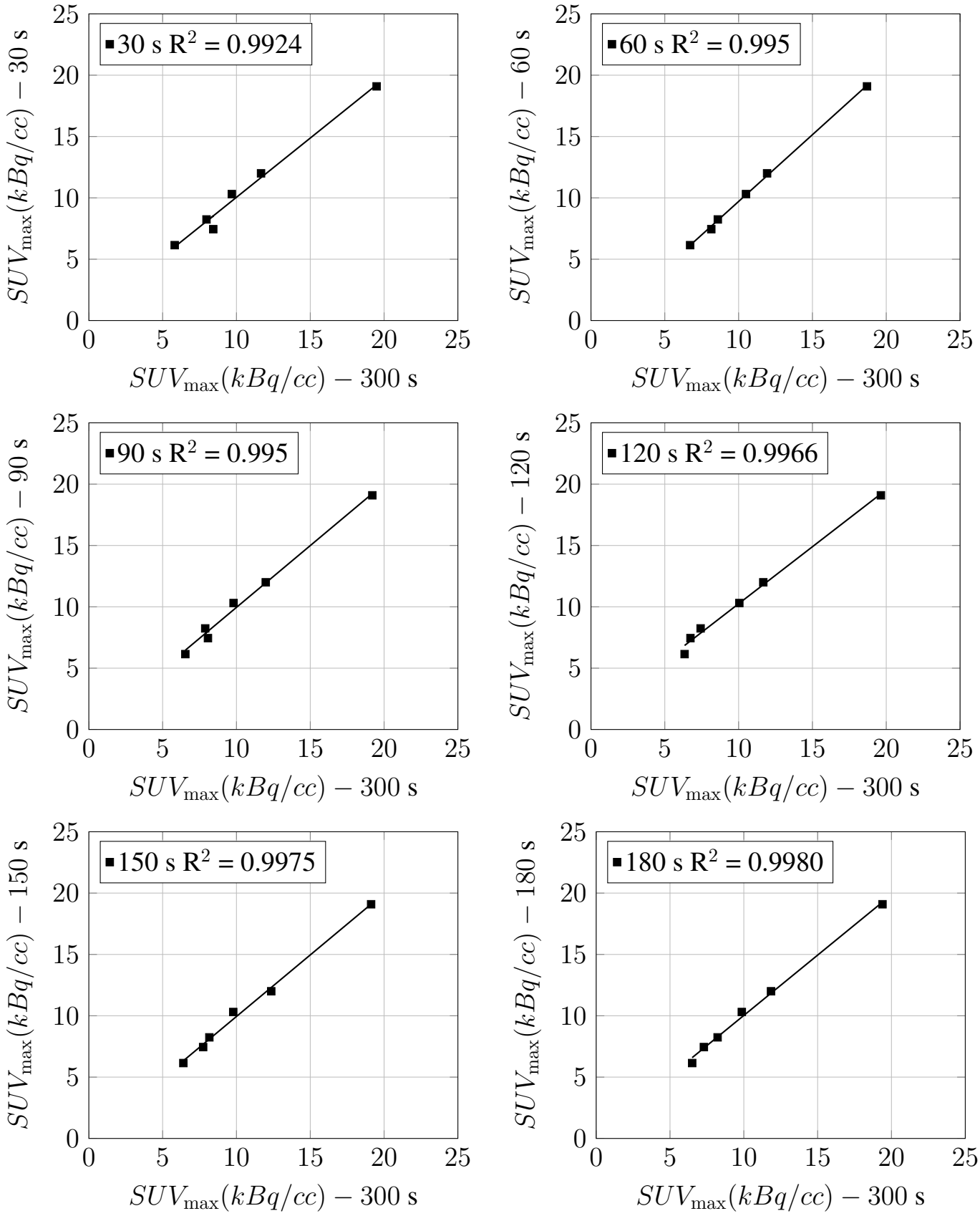

Figure 4.14: Maximum activity concentration of different acquisition times versus maximum activity concentration of 300 s acquisition time for focal points (smooth A - Low Contrast)

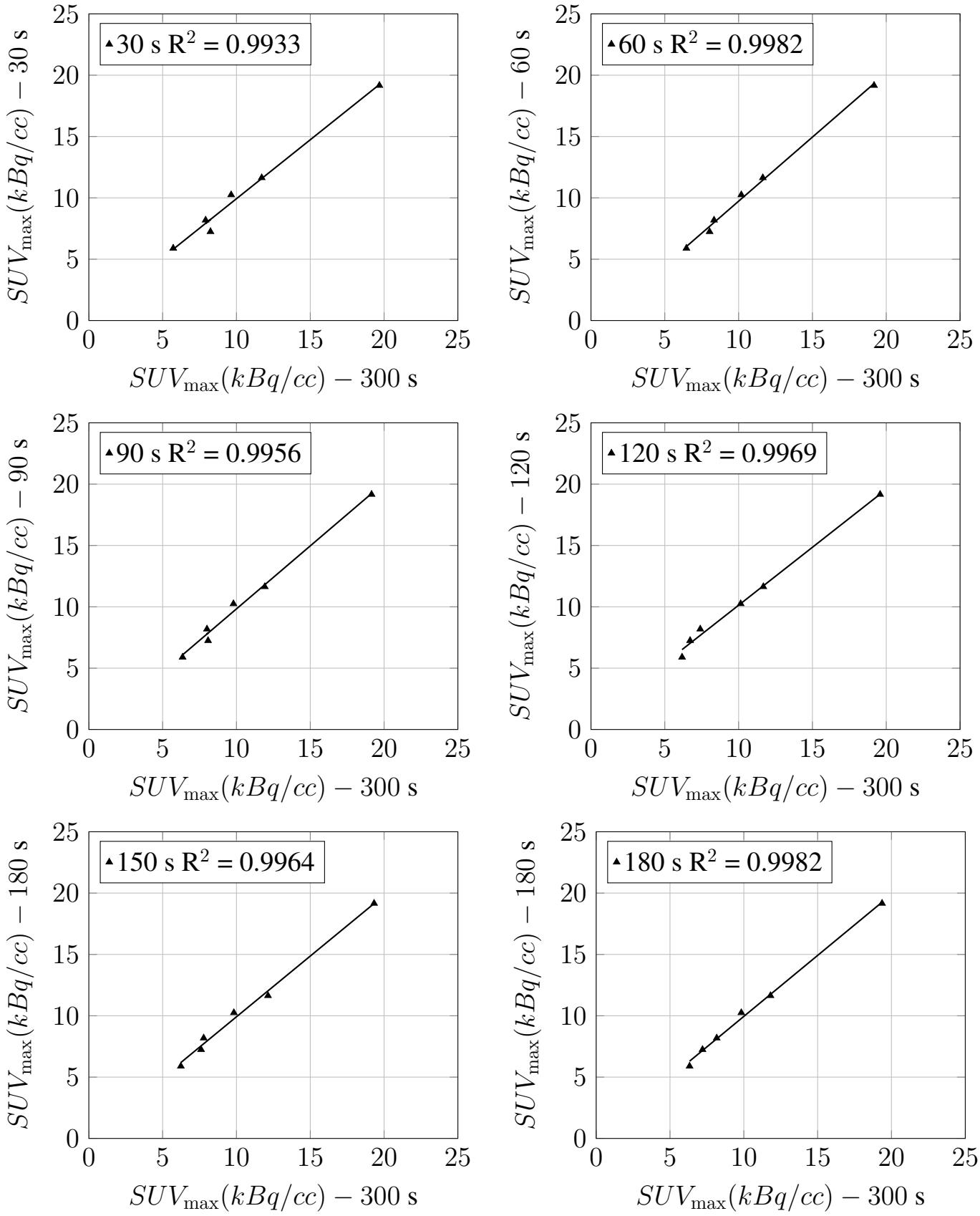

Figure 4.15: Maximum activity concentration of different acquisition times versus maximum activity concentration of 300 s acquisition time for focal points (smooth B - Low Contrast)

4.3 Uniformity - High Contrast

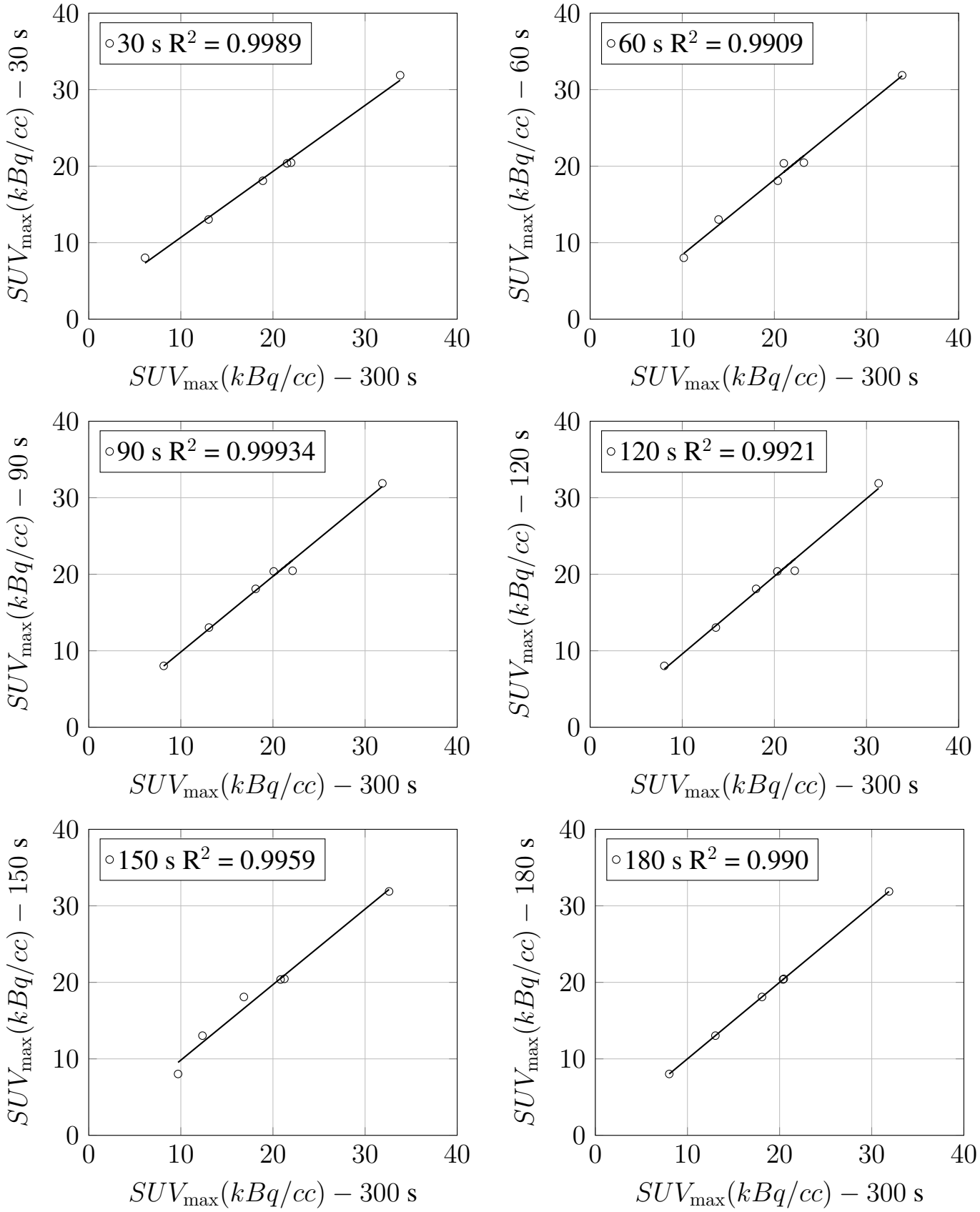

Figure 4.16: Maximum activity concentration of different acquisition times versus maximum activity concentration of 300 s acquisition time for focal points (normal - High Contrast)

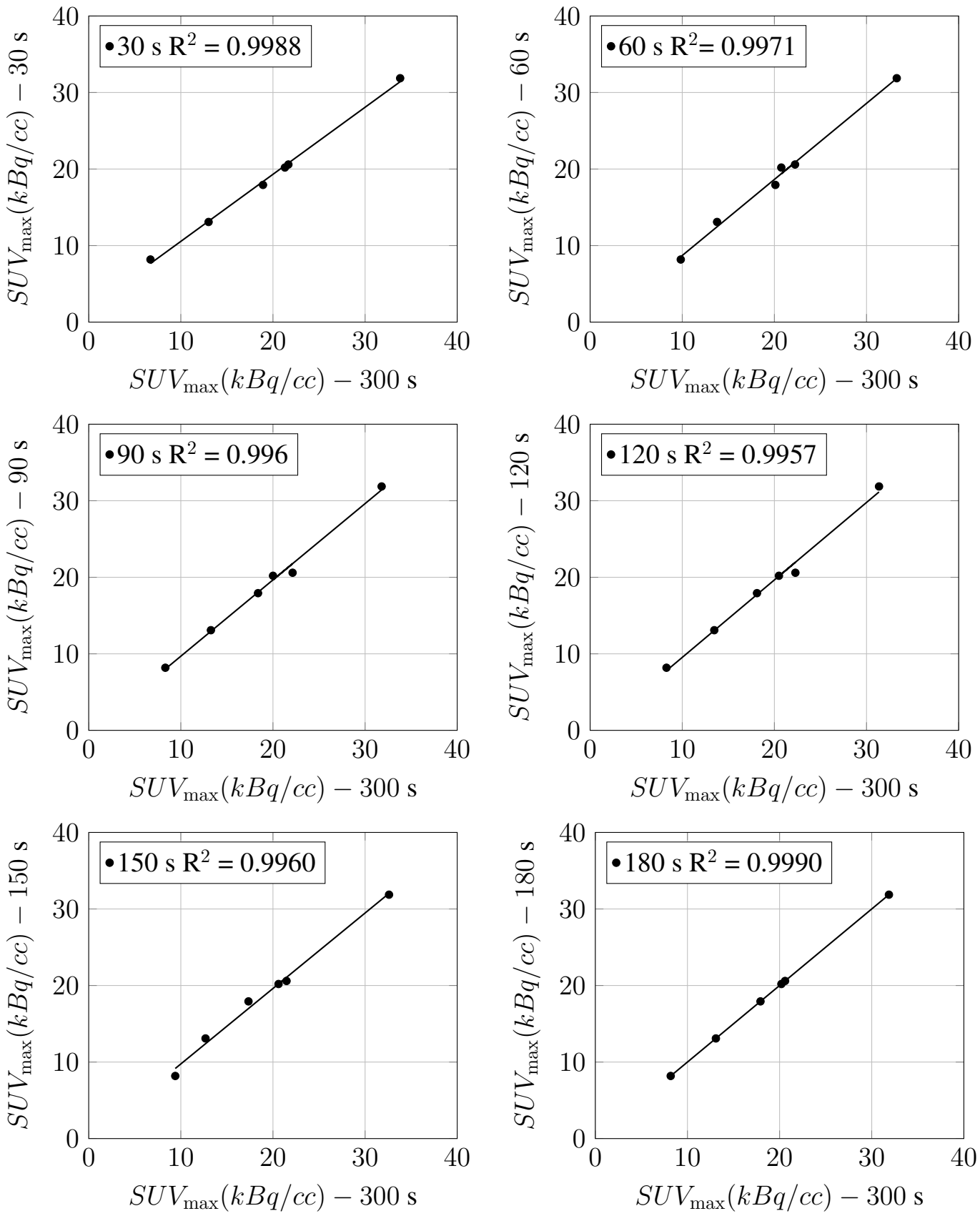

Figure 4.17: Maximum activity concentration of different acquisition times versus maximum activity concentration of 300 s acquisition time for focal points (smooth - High Contrast)

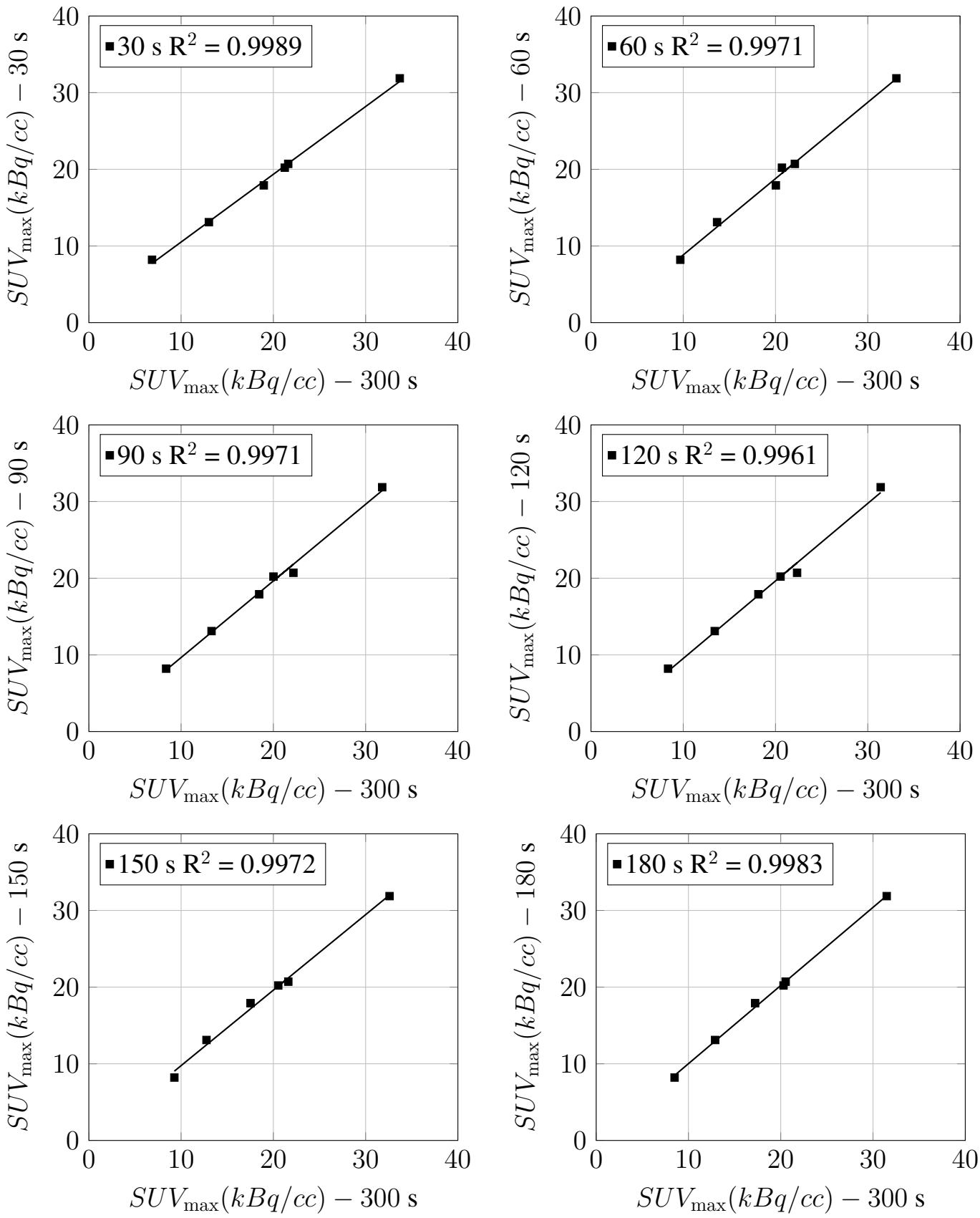

Figure 4.18: Maximum activity concentration of different acquisition times versus maximum activity concentration of 300 s acquisition time for focal points (smooth A - High Contrast)

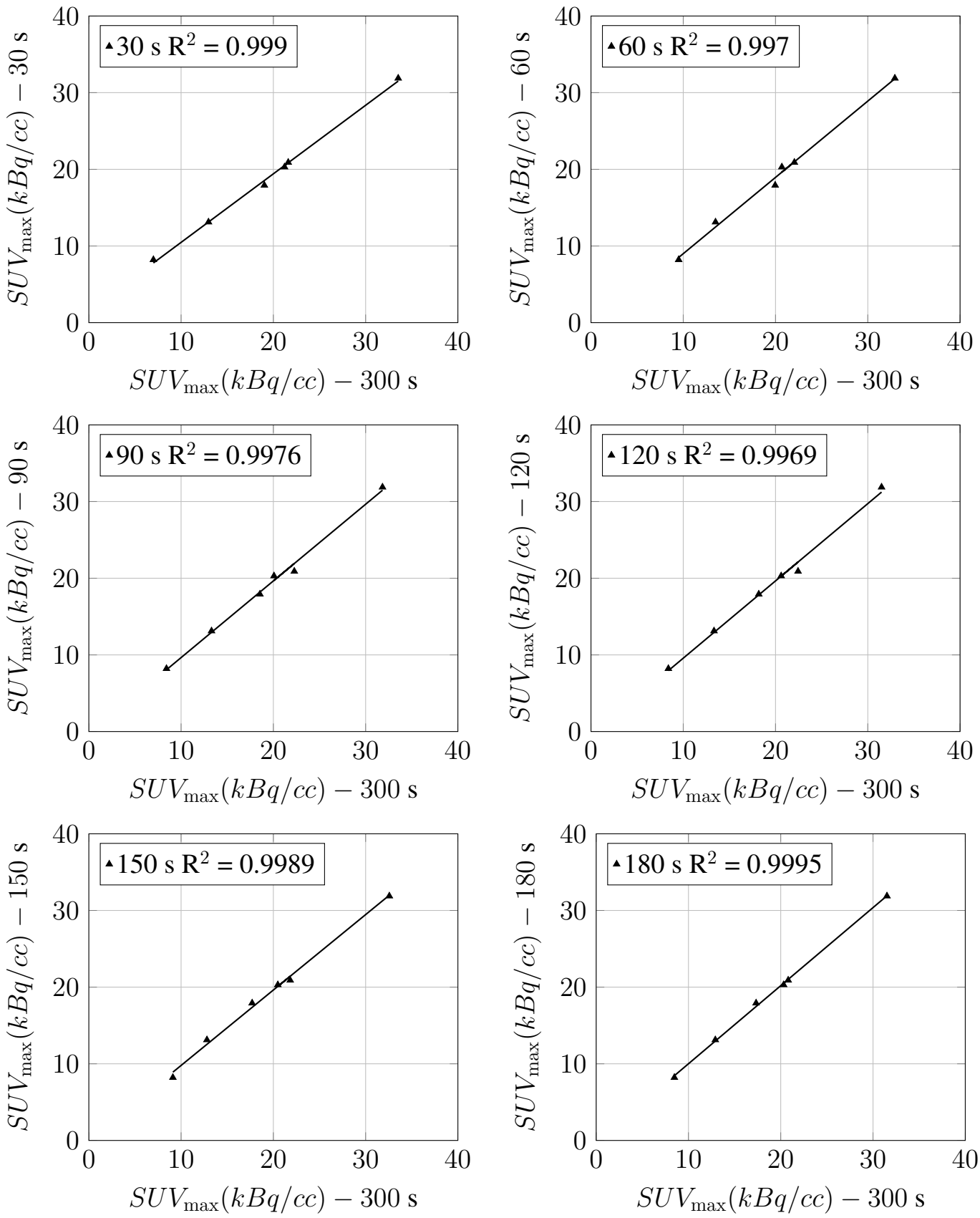

Figure 4.19: Maximum activity concentration of different acquisition times versus maximum activity concentration of 300 s acquisition time for focal points (smooth B - High Contrast)

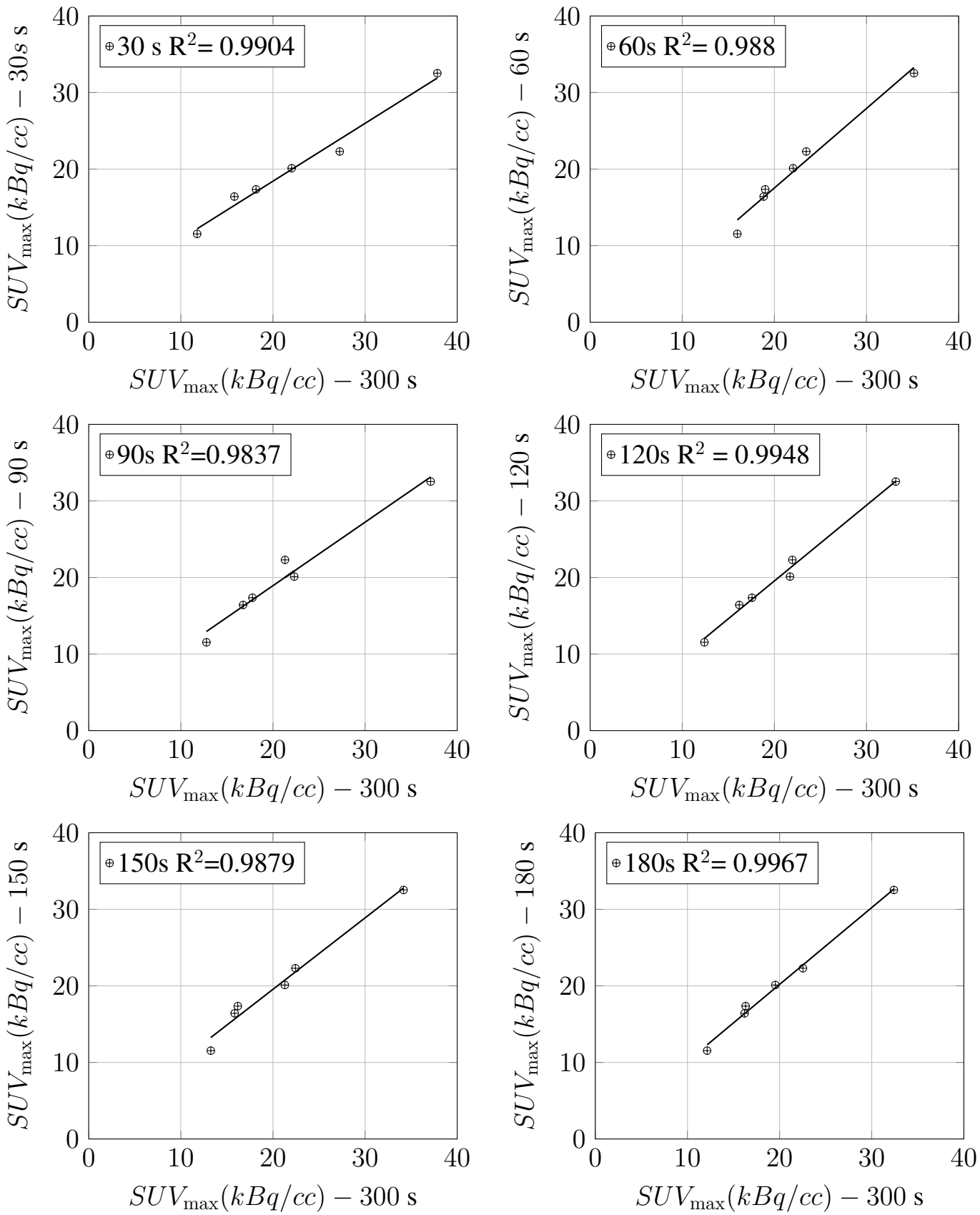

Figure 4.20: Maximum activity concentration of different acquisition times versus maximum activity concentration of 300 s acquisition time for focal points (smooth B - High Contrast–(2 mm^3)

Chapter 5

Discussion

This research was carried out to investigate how different image reconstruction parameters and acquisition times impact on image quality. In agreement with the NEMA NU 2–2007 protocol, the NEMA body phantom was prepared and scanned according to these PET/CT protocols. To reach an exact activity concentration ratio was challenging due to uncertainties in both measuring, time delay (decay), and mixing the activity. The capability of the Gemini TF Big Bore PET scanner for ^{68}Ga imaging was characterized based on a series of standard measurements based on the NEMA protocol. Analysis such as COV%, CNR, SNR and RC% assisted us to evaluate the performance of the PET scanner.

The COV% as the ratio of the standard deviation of the background ROIs to the mean uniform activity in the background ROIs (Ahangari et al., 2015) was used as a parameter to measure noise in PET image quality. Noise represents the existence of a significant unwanted signal that presents a different appearance from the expected signal in a medical image (Oliveira, 2016).

In PET the emission of positrons is a physically random process that follows the Poisson distribution technique, where the presence of noise is inevitable (Karakatsanis, Loudos and Nikita, 2009).

The objective is to limit the effect of noise and improve image quality either through increasing activity or acquisition time. Within assessing noise on low and high contrast images, high contrast images had increased noise of 1.03 – 1.16 COV% (figure 4.5) when compared to those of low contrast of 0.89 – 0.99 COV% (figure 4.4) respectively when evaluating for 180 second scan acquisition which shows to reach convergence. Furthermore, high contrast images reconstructed using head and neck protocol with 2x2x2 mm^3 had large noise of 1.25 COV% in comparison to where a larger pixel size was used.

McKeown (2019) detailed smaller voxel sizes can improve PET spatial resolution, however, as voxel size decreased the number of reconstructed events that contributed to each voxel decreased too, thereby increasing the statistical noise in each voxel. A selection of image smoothing (normal, smooth, smooth A and smooth B) parameters were used to reduce the effects of noise on image quality, but with a higher smoothing level, image contrast is also reduced. When acquisition time was varied in evaluating noise on high and low contrast images using different reconstruction parameters, it was found that low contrast images using ”smooth” and ”smooth A” smoothing converged at 180 s. The Gemini TF PET scanner with an axial FOV of 18 cm demonstrated its ability to reduce image noise while maintaining good PET image quality (Akamatsu et al., 2014).

When assessing the ability of different reconstruction parameters to generate useful image contrast, all spheres reconstructed in the high contrast situation were noticeable for all acquisition times, however the different λ (smoothing level) settings had different and sometimes more noise fluctuations (see figure 4.5). The phantom spheres for low contrast were noticeable as acquisition time increased. Oliveira (2016) defines CNR as a measure of an imaging system to determine clinically useful image contrast and that a higher CNR is essential in order to differentiate between objects.

CNR approaches convergence at 180 seconds for all smoothing parameters on low and high contrast images. Low contrast images gave better CNR of 0.96 – 1.08 (figure 4.6) when compared to those of high contrast of 0.84 – 0.91 (figure 4.7). The HN reconstruction with smaller voxel showed CNR of 0.82 value compared to the others.

The number of detected events determines the SNR (Cherry, Sorenson and Phelps, 2012). SNR represents the ratio between meaningful information and the background noise. Oliveira (2016) advocate the quality of an image can be described by its SNR as it affects diagnostic and quantitative accuracy, as a result the goal of nuclear medicine equipment is to maximize SNR in an image. The Gemini TF PET's LYSO fast scintillator with high stopping power, and Anger–logic design enables the detector to reduce noise while improving the SNR. Low and high contrast images were analysed, and qualitatively assessed. Both converged towards 1 at 180 s with SNR of 0.99 – 1.05 for low contrast images (figure 4.9), 0.80 – 0.97 for high contrast images (figure 4.8) and for smaller voxel a SNR of 0.75 (figure 4.9).

The experiment showed in terms of RC, that a more accurate quantification of activity concentration can be achieved from 180 seconds on for both high and low image contrast for all smoothing parameters used.

In this study optimization of acquisition time using BLOB–OS (with TOF) reconstruction with various smoothing parameters were analyzed. The results obtained from the phantom study demonstrated the Philips Gemini TF Big Bore PET scanner's stability of good uniformity when assessing maximum activity concentration among the different acquisitions, and the ability of the scanner to detect or recover radioactivity in low and high contrast images for all smoothing parameters. According to phantom results the feasibility of reducing time incorporating smoothing reconstruction parameter "smooth" on low contrast images, acquisition time can be reduced to 180 seconds while maintaining acceptable image quality. The study confirms that 180 seconds per bed position is an optimal acquisition time duration.

Using head and neck protocol resulted in high fluctuations of image noise and low SNR. There was an increase in image noise when using small 2 mm voxels instead of 4 mm. Higher smoothing levels (smooth A or smooth B) are not appropriate to use for shorter scan times as they produce high fluctuation in image noise both for high contrast voxels (4x4x4 mm^3 and 2x2x2 mm^3) images. Incorporating smaller reconstruction parameters (normal and smooth), the acquisition time can be reduced to 180 seconds with no loss of image quality, making it possible to increase patient throughout using ^{68}Ga tracers.

The current study demonstrated that the Gemini PET/CT system permitted emission scan of 3 min/bed positions using the NEMA phantom without compromising image quality when 5 min/bed positions were used as reference standard. However, phantom measurements are always a simplification of real patient measurements. Therefore, the results has to be validated clinically by further research. An approach for such validation might be possible with the WCAPC scanner, because the system uses list mode data acquisition. This allows reconstruction of patient data with different frame duration times. An evaluation of the recommended 3 min/bed position images and referenced images with 5 min/bed position by multiple readers (e.g. nuclear medicine physicians with different experience) could clarify, if the results of phantom measurements can be translated directly into clinical application.

The strength of this research was having to simulate a real life situation using patient data. The difficulties experienced were manually drawing the ROIs on the Hermes hybrid software as they were not on the same position on different slices. The study therefore recommend the use of a programming language to determine the accuracy of the manual analysis of ROIs on different slices. The analysis were only based on ^{68}Ga DOTANOC data, as it cannot be replicated to other ^{68}Ga studies, further research is recommended on ^{68}Ga PSMA.

Chapter 6

Conclusion

Incorporating BLOB–OS (TOF) reconstruction using the 4 mm voxel on low contrast images, acquisition time can be reduced to 180 s with smooth smoothing while preserving the image quality. This time reduction can be translated into improvement of patient comfort, patient throughput and avoiding image artifacts due to longer acquisition.

Bibliography

Adams, M.C., Turkington, T.G., Wilson, J.M. and Wong, T.Z., 2010. A systematic review of the factors affecting accuracy of SUV measurements. *American Journal of Roentgenology*, 195(2), pp.310–320.

Ahangari, S., Ghafarian, P., Shekari, M., Ghadiri, H., Bakhshayeshkaram, M. and Ay, M., 2015. The impact of point spread function modeling on scan duration in PET imaging. *Frontier in biomedical Technologies*, 2(3), pp.137–145.

Ahasan, M.M., Mahmud, A., Khanam, M.N., Afroz, S., Khatun, R., Akter, S., Atique Ullah, A.K.M. and Rahman, M.M., 2011. Study of Noise Equivalent Count Rate (NECR) of a PET camera with a FOV of 0.2m. *Nuclear Science and Applications*, 20(1& 2), pp.35–37.

Akamatsu, G., Uba, K., Taniguchi, T., Mitsumoto, K., Narisue, A., Tsutsui, Y. and Sasaki, M., 2014. Impact of time–of–flight PET/CT with a large axial field of view for reducing whole body acquisition time. *Journal of Nuclear Medicine Technology*, 42(2), pp.101–104.

Al Hussani, M.T. and Ali Al Hayani, M., 2014. The use of filtered back projection algorithm for reconstruction of tomographic image. *Al–Nahrain Journal for College of Engineering Sciences*, 17(2), pp.151–156.

Antić, V. and Haglund, J., 2016. Connections between noise equivalent count rate and image noise in PET medical imaging. Rad Conference Proceedings, 1, pp.187–190.

Banerjee, S.R. and Pomper, M.G., 2013. Clinical application of Gallium-68. *Applied Radiation and Isotopes*, 76, pp.2–13.

Beister, M., Kolditz, D. and Kalender, W.A., 2012. Iterative reconstruction methods in X–ray CT. *Physica Medica*, 28(2), pp.94–108.

Bettinardi, V., Castiglioni, I., De Bernadi, E. and Gilardi, M.C., 2014. PET quantification: strategies for partial volume correction. *Clinical and Translational Imaging*, 2, pp.199–218.

Bushberg, J.T., Seibert, J.A., Leidholdt, E.M. and Boone, J.M., 2012. *The essential physics of medical imaging*. 3rd ed. Philadelphia: Lippincott Williams & Wilkins.

Casey, M.E. and Nutt, R., 1986. A multi crystal two dimensional BGO detector system for positron emission tomography. *IEEE Transactions on Nuclear Science*, 33(1), pp.460–463.

Cherry, S., Sorenson, J. and Phelps, M., 2012. *Physics in Nuclear Medicine*. 4th ed. Philadelphis, PA.: Elsevier Saunders.

Chuang, K.S., Jan, M.L., Wu, J., Lu, J.C., Chen, S., Hsu, C.H. and Fu, Y.K., 2005. A maximum likelihood expectation maximization algorithm with thresholding. *Computerized Medical Imaging and Graphics*, 29(7), pp.571–578.

Conti, M., 2011. Focus on time of flight PET: the benefits of improved time resolution. *European Journal of Nuclear Medicine and Molecular Imaging*, 38, pp.1147–1157.

DeWerd, L.A. and Kissick, M., eds, 2014. *The phantoms of medical and health physics devices for research and development*. New York: Springer.

Fogelman, I., Gnanasegaran, G. and Wall, H. van der, eds, 2012. *Radionuclide and hybrid bone imaging*. 1st ed. Berlin,Heidelberg: Springer.

Francis, H., Amuasi, J.H., Kwame, K.A. and Vangu, M.D.T., 2016. Quantitative assessment of radionuclide uptake and positron emission tomography–computed tomography image contrast. *World Journal of Nuclear Medicine*, 15(3), pp.167–172.

Fukukita, H., Senda, M., Terauchi, T., Suzuki, K., Daisaki, H., Matsumoto, K., Ikari, Y. and Hayashi, M., 2010. Japanese guideline for the oncology FDG-PET/CT data acquisition protocol: Synopsis of version 1.0. *Annals of nuclear medicine*, 24(4), pp.325–34.

Garcea, G., Ong, S.L. and Maddern, G.J., 2009. The current role of PET-CT in the characterization of hepatobiliary malignancies. *The official journal of the International Hepato-Pancreato Billiary Association*, 11(1), pp.4–17.

Groheux, D., Martineau, A., Vrigneaud, J., Hindie, E., Baillet, G. and Moretti, J., 2009. Effect of variation in relaxation parameter value on LOR–RAMLA reconstruction of 18F–FDG PET studies. *Nuclear Medicine Communications*, 30(12), pp.926–933.

Guerra, A., 2004. *Ionizing radiation detectors for medical imaging*. Singapore: World Scientific Publishing.

Hausmann, D., Dinter, D.J., Sadick, M., Brade, J., Schoenberg, S.O. and Büsing, K., 2012. The impact of acquisition time on image quality in whole–body ^{18}F–FDG PET/CT for cancer staging. *Journal of Nuclear Medicine and Technology*, 40(4), pp.255–258.

Hendee, W. and Ritenour, E., 2002. *Medical Imaging Physics*. 4th ed. Wiley-Liss.

Herman, G.T. and Meyer, L.B., 1993. Algebraic reconstruction techniques can be made computationally efficient (positron emission tomography application). *IEEE Transactions on Medical Imaging*, 12(3), pp.600–609.

IAEA, 2014. *IAEA human health series no.27:PET/CT atlas on quality control and image artefacts*. Vienna, Austria: International Atomic Energy Association.

Jakoby, B.W., Bercier, Y., Conti, M., Casey, M.E., Bendriem, B. and Townsend, D.W., 2011. Physical and clinical performance of the mCT time–of–flight PET/CT scanner. *Physics in Medicine and Biology*, 56(8), pp.2375–2389.

Kangai, Y. and Onishi, H., 2016. Acquisition time optimization of positron emission tomography studies by use of a regression function derived from torso cross–sections and noise–equivalent counts. *Radiological Physics and Technology*, 9(2), pp.161–169.

Karakatsanis, N.A., Fokou, E. and Tsoumpass, C., 2015. Dosage optimization in positron emission tomography: state of the art methods and future prospects. *American Journal of Nuclear Medicine and Molecular Imaging*, 5(5), pp.527–547.

Karakatsanis, N.A., Loudos, G. and Nikita, K.S., 2009. A methodology for optimizing the acquisition time of a clinical pet scan using GATE. *IAEE nuclear Science Symposium Conference Record*, FL. pp.2896–2901.

Krempser, A.R., Ichinose, R.M., Sá, A. Miranda de, Oliveira, S.M. Velasques de and Carneiro, M.P., 2013. Recovery coefficients determination for partial volume effect correction in oncological PET/CT images considering the effect of activity outside the field of view. *Annals of Nuclear Medicine*, 27(10), pp.924–930.

Lee, J.S., 2010. Technical advances in current PET and Hybrid Imaging systems. *The Open Nuclear Medicine Journal*, 2, pp.192–208.

Martiniova, L., De Palatis, L., Etchebehere, E. and Ravizzini, G., 2016. Gallium 68 in medical imaging. *Current Radiopharmaceuticals*, 9(3), pp.187–207.

Masuda, Y., Kondo, C., Matsuo, Y., Uetani, M. and Kusakabe, K., 2009. Comparison of imaging protocols for 18F–FDG PET/CT in overweight patients: optimizing scan duration versus administered dose. *Journal of Nuclear Medicine*, 50(6), pp.844–848.

McKeown, C., 2019. *Optimisation and assessment techniques for clinical PET reconstruction*. Thesis (PhD). University of Glasgow.

Melcher, C.L., 2000. Scintillation crystals for PET. *Journal of Nuclear Medicine*, 41, pp.1051–1055.

Mettler, F. and Guiberteau, M., 2012. *Essentials of Nuclear Medicine Imaging*. 6th ed. Philadelphia, PA: Elsevier, Saunders.

Mittra, E. and Quon, A., 2009. Positron emission tomography/computed tomography: the current technology and applications. *Radiologic Clinics of North America*, 47(1), pp.147–160.

Moses, W.M., 2011. Fundamental limits of spatial resolution in PET. *Nuclear Instruments & Methods in Physics Research A*, 648(S1), pp.S236–S240.

NEMA NU 2 2007, 2007. *NEMA Standards Publication NU 2-2007: Performance Measurement of Positron Emission Tomographs.* Rosslyn, VA: National Electrical Manufactures Association.

Oliveira, J., 2016. *Influence of the time–of–flight and the acquisition time on image quality in positron emission Tomography/Computed Tomography scanners*. Thesis (M.Sc.). Instituto Politecnico de Lisboa, Lisboa.

Oliveira, J., Parafita, R., Branco, S. and Susana, 2018. Minimisation of acquisition time in a TOF PET/CT scanner without compromising image quality. *Proceeding of vi eccomas thematic conference on computational vision and medical image processing*, 18–20 October 2017, Portugal. Porto: Springer International, pp.1–16.

Powsner, R., Palmer, M. and Powsner, E., 2013. *Essentials of nuclear medicine physics and instrumentation*. 3rd ed. John Wiley & Sons.

Saha, G., 2010. *Fundamentals of Nuclear Pharmacy*. 6th ed. New York: Springer.

Shanchez-Crespo, A., 2013. Comparison of Gallium–68 and Fluorine–18 imaging characteristics in positron emission tomography. *Applied Radiation and Isotopes*, 76, pp.55–62.

Shreve, P. and Townsend, D., eds, 2011. *Clinical PET–CT in radiology: integrated imaging in oncology*. New York, London: Springer.

Smith, N. and Webb, A., 2011. *Introduction to Medical Imaging Physics, Engineering and Clinical Application*. Cambridge, UK: Cambridge University Press.

Soret, M., Bacharach, S.L. and Buvat, I., 2007. Partial–volume effect in PET tumor imaging. *The Journal of Nuclear Medicine*, 48(8), pp.932–945.

Surti, S., Kuhn, A., Werner, M.E., Perkins, A.E., Kolthammer, J. and Karp, J., 2007. Performance of Philips Gemini TF PET/CT scanner with special consideration for its time-of-flight imaging capabilities. *Journal of Nuclear Medicine*, 48(3), pp.471–480.

Taniguchi, T., Akamatsu, G., Kasahara, Y., Mitsumoto, K., Baba, S., Tsutsui, Y., Himuro, K., Mikasa, S., Kidera, D. and Sasaki, M., 2015. Improvement in PET/CT image quality in overweight patients with PSF and TOF. *Annals of Nuclear Medicine*, 29(1), pp.71–77.

Turkington, T.G., 2001. Introduction to PET instrumentation. *Journal of Nuclear Medicine Technology*, 29(1), pp.4–11.

Ullah, M.N., Pratiwi, E., Cheon, J., Choi, H. and Yeo, J., 2016. Instrumentation for time–of–flight positron emission tomography. *Nuclear Medicine and Molecular Imaging*, 50(2), pp.112–122.

Umeda, T., Miwa, K., Murata, T., Miyaji, N., Wagatsuma, K., Motegi, K., Terauchi, T. and Koizumi, M., 2017. Optimization of a shorter variable–acquisition time for legs to achieve true whole–body PET/CT images. *Australasian Physical and Engineering Sciences in Medicine*, 40(4), pp.861–868.

Vandenberghe, S., Mikhaylova, E., D'Hoe, E., Mollet, P. and Karp, J.S., 2016. Recent developments in time of flight PET. *European Journal of Nuclear Medicine and Molecular Imaging*, 3(3), pp.1–30.

Von Schulthess, G., ed., 2007. *Molecular anatomic imaging: PET–CT and SPECT–CT integrated modality*. 2nd ed. Philadelphia, PA: Lippincott Williams & Wilkins.

Wernick, M. and Aarsvold, J., eds, 2004. *Emission tomography: the fundamentals of PET and SPECT*. San Diego, California,USA: Elsevier.

Workman, R. and Coleman, R., eds, 2006. *PET/CT Essentials for Clinical Practice*. New York, USA: Springer.

Zaidi, H., ed., 2006. *Quantitative analysis in nuclear medicine imaging*. Singapore: Springer.